Development of a Pilot Low Temperature Solar Thermal Co-Generation System for Water Distillation and Energy Production

by

Jacobus Gerhardus van Zyl

Thesis presented in partial fulfilment of the requirements for the degree of Master of Engineering (Mechanical Engineering) in the Faculty of Engineering at Stellenbosch University

Supervisor: Prof Michael Owen

December 2023

Declaration

By submitting this thesis electronically, I declare that the entirety of the work contained therein is my own, original work, that I am the sole author thereof (save to the extent explicitly otherwise stated), that reproduction and publication thereof by Stellenbosch University will not infringe any third party rights and that I have not previously in its entirety or in part submitted it for obtaining any qualification.

Date: December 2023

Abstract

This study aimed to develop a pilot system for low temperature solar thermal combined power and clean water co-generation. The system comprised a solar thermal steam generation system (6.5 kW_{th} external compound parabolic concentrating collector array and kettle-type boiler) coupled to a condensing steam engine (reciprocating steam expander and condenser). The system uses solar thermal energy to produce steam at ~1 atm from raw feedwater. The steam is used to drive the steam expander (both through steam work and condensation) to produce mechanical work (which can be used directly for pumping or converted to electricity). The vapor exiting the engine is condensed and collected, providing distilled water for human use. The steam expander was designed by the University of Southampton and was manufactured at Stellenbosch University. The rest of the overall system (solar steam generator and condenser) was designed and constructed as part of this work with the intent to integrate the expander. Unfortunately, the expander did not operate, and this thesis thus reports on the design of the overall system and the measured performance of the solar steam generator and condenser (including measured distilled water production). The mechanical and electrical energy generation of the system was estimated using the measured steam generation and engine thermal efficiencies from literature. Results from three day-long on-sun tests are provided and prove that the steam generation system was able to meet its performance requirements (specifically providing steam at the required flow rate and condition to the condensing engine). The system produced distillate at an average specific energy consumption (SEC) of 2125 kWh/m^3 and an estimated average mechanical energy output of 0.039 kWh/m^2 of collector aperture area per day. The monthly and annual distillate production and energy generation were also estimated to illustrate the longer term expected performance with an estimated annual yield of 17.1 kWh/m^2 mechanical energy and 1012 L distilled water. Compared to existing low temperature energy systems (e.g. organic Rankine cycles for low-grade power generation), and various technologies for solar desalination (notably solar PV powered reverse osmosis), the investigated system proves to be infeasible based on its high SEC, low overall efficiency and relative complexity (notably in terms of the condensing engine).

KEY WORDS: co-generation, compound parabolic concentrator, desalination, distillation, solar thermal energy, steam expansion

Uittreksel

Hierdie studie het gemik om 'n prototipe te ontwikkel vir laetemperatuur-sontermiese gekombineerde krag en skoonwater-ko-opwekking. Die stelsel het bestaan uit 'n sontermiese stoom-opwekkingstelsel (6.5 $kW_{termies}$ eksterne saamgestelde paraboliese konsentreerder en ketel) gekoppel aan 'n kondenserende stoomenjin. Die stelsel gebruik sontermieseenergie om stoom teen ~1 atm van onbehandelde voerwater te genereer. Die stoom word gebruik om die stoomuitbreider aan te dryf (beide deur stoomwerk en kondensasie) en om meganiese werk te vervaardig (wat direk vir pompwerk gebruik kan word of omgeskakel kan word na elektrisiteit). Die damp wat die enjin verlaat, word gekondenseer en versamel, wat gedistilleerde water vir menslike gebruik verskaf. Die algehele en stoomopwekkingstelsels is ontwerp as deel van hierdie werk en vorm die primêre fokus van hierdie studie. Die stoomuitbreider is ontwerp deur die Universiteit van Southampton en is vervaardig deur Stellenbosch Universiteit. Die res van die algehele stelsel (sonkrag-stoomgenerator en kondensor) is ontwerp en gebou as deel van hierdie werk met die doel om die uitbreider te integreer en geïntegreer in die algehele stelsel in hierdie projek. Ongelukkig het die enjinuitbreider nie gewerk nie, en hierdie tesis doen dus verslag oor die ontwerp van die algehele stelsel en die gemete werkverrigting van die stoomopwekkingstelsel sonstoomopwekker en kondensor (insluitend gemete skoon gedistilleerde waterproduksie). Die meganiese en elektriese energieopwekking van die stelsel is beraam deur gebruik te maak van die gemete stoomopwekking en enjin se termiese doeltreffendheid uit literatuur. Resultate van drie daglange sonop toetse word verskaf en bewys dat die stoomopwekkingstelsel in staat was om aan sy werkverrigtingvereistes te voldoen (spesifiek die verskaffing van stoom teen die vereiste vloeitempo en toestand aan die kondensenjin). Die stelsel het distillaat geproduseer teen 'n gemiddelde spesifieke energieverbruik (SEC) van 2125 $kWh_{sonkrag}/m^3$ en 'n geskatte gemiddelde meganiese kraglewering van 0.039 kWh/m^2 van die versamelaar-openingoppervlakte per dag. Die maandelikse en jaarlikse distillaatproduksie en energieopwekking is ook beraam om die verwagte verrigting op langer termyn te illustreer met 'n geskatte jaarlikse opbrengs van 17.1 kWh/m^2 meganiese energie en 1012 L gedistilleerde water. In vergelyking met bestaande laetemperatuur-energiestelsels (bv. organiese Rankine-siklusse vir laegraadse kragopwekking), en verskeie tegnologieë vir sonkrag-ontsouting (veral sonkrag-PV-aangedrewe tru-osmose), blyk die ondersoekde stelsel onuitvoerbaar te wees op grond van sy hoë SEC, lae algehele doeltreffendheid en relatiewe kompleksiteit (veral in terme van die kondenserende enjin).

SLEUTELWOORDE: distillasie, medegenerasie, ontsouting, saamgestelde paraboliese konsentreerder, sontermieseenergie, stoomuitbreiding

Acknowledgements

This project was funded by United Kingdom Research and Innovation (UKRI) as part of their Global Challenges Research Fund (GCRF). I would like to thank them for their financial support and for the opportunity to have been involved in this study.

I would like to thank my wife for being by my side throughout this project – for her unwavering support through encouragement, show of care, and many sacrifices throughout these past three years. She played an integral role in helping me to stay focused and motivated, and to enjoy this project from beginning to end.

I must thank my supervisor, Prof. Mike Owen, for his excellent mentorship. It was a genuine pleasure working with him. I have learnt many things from him – most notably, his practical approach to problem solving, logical approach to writing, and empowering leadership.

My sincerest thank you to my parents and brother for their support during this project. I would not have been at the end of my Master's in mechanical engineering if it were not for their many sacrifices throughout my life.

I want to say thank you to Stan Rietveld for his assistance over a period of three months during his internship at our research group. It was very helpful to have a work partner for that period and to have made a great new friend.

I acknowledge that the execution of this project was only possible thanks to the team at the Stellenbosch University Mechanical and Mechatronic Engineering Department – namely, Simorné Paulse, Ferdi Zietsman, Graham Hamerse, Calvin Hamerse, Cobus Samuels, and PJ Robyn, who all worked many hours on manufacturing and installation tasks; Kevin Neaves for his technical assistance related to electrical and electronic matters; Cobus Zietsman for his advice and guidance; as well as Nathi Hlwempu and Juliun Stanfliet for their technical advice but also many hours of physical labour. I have learnt much from each of them and am a much better engineer today because of their inputs.

I also want to thank Michael Reed for his assistance in the design of this experimental system through his findings in a computerised model of the system. It was especially good to work with him in the early part of the project to navigate the various uncertainties in terms of project scope and the system design.

I must also thank the team from the University of Southampton – Gerald Müller and Curtis Howell – for the collaboration we had with them. Unfortunately, there were some challenges, particularly with regards to the condensing engine, which we acknowledge is disappointing, but we believe the results from this project are nonetheless useful to add to their research into the modern application of the condensing engine.

Dedication

This thesis was done to the best of my ability in dedication to the Lord Jesus.

So whether you eat or drink or whatever you do, do it all for the glory of God.

– 1 Corinthians 10:31

Table of Contents

List of Tables

List of Figures

Nomenclature

Abbreviations

AMVP	Auto-Mechanical Vacuum Pump
BDC	Bottom Dead Centre
CSP	Concentrated Solar Power
DNI	Direct Normal Irradiance [W/m^2] or Irradiation [kWh/m^2]
DHI	Diffuse Horizontal Irradiance [W/m^2] or Irradiation [kWh/m^2]
EDPM	Ethylene Propylene Diene Monomer
FS	Full-Scale
GHI	Global Horizontal Irradiance [W/m^2] or Irradiation [kWh/m^2]
GTI	Global Tilt Irradiance [W/m^2] or Irradiation [kWh/m^2]
HTF	Heat Transfer Fluid
MBV	Manual Ball Valve
NC	Normally Closed
NO	Normally Open
ORC	Organic Rankine Cycle
PV	Photovoltaic
SABS	South African Bureau of Standards
SADC	Southern African Development Community
SDG	Sustainable Development Goal
SEC	Specific Energy Consumption [kWh/m^3]
SKV	Sky View Factor
SSGS	Solar Steam Generation System
SRL	Solar Rooftop Laboratory
SU	Stellenbosch University
SV	Solenoid Valve
TDC	Top Dead Centre
TDS	Total Dissolved Solids
TIASA	Thermal Insulation Association of Southern Africa
UN	United Nations
UoS	University of Southampton
WHO	World Health Organisation
WRS	Water Reticulation System
XCPC	External Compound Parabolic Concentrator

Symbols

a	Heat loss coefficient

A	Collector area [m^2] – may refer to either the gross collector area or aperture area, depending on the case
C	Concentration ratio
β	Collector tilt angle (inclination) relative to horizontal [°]
d	Diameter [m or mm]
D	Diameter [m or mm]
δ	Solar declination angle [°]
G	Irradiance [W/m^2]
H	Height/distance [m]
L	Length [m or mm]
η	Efficiency
$\dot{m}$	Mass flowrate [kg/s, kg/hr]
N	Numeric day of the year
P	Pressure [Pa, bar]
ρ	Density [kg/m^3]
u	Specific internal energy [J/kg]
v	Specific volume [m^3/kg] or linear velocity [m/s]
V	Volume [m^3, L]
ω	Angular velocity/rotational speed [rad/s]
w	Velocity [m/s]
W	Mechanical work [J]
$\dot{W}$	Power [W]
$\dot{Q}$	Heat transfer rate [W]
z	Relative height from defined datum [m]

Subscripts

0	For optical efficiency (η_0) – zero (0) represents the case of zero heat loss when the mean collector temperature equals the ambient temperature ($\Delta T_{ma} = 0$), then $\eta_{coll} = \eta_0$. Also used to denote solar constant (G_0).
II	Second Law
a	Ambient, aperture
A	Branch A on collector array
acc	Acceptance
adm	Admission
alb	Albedo (ground-reflected)
b	Beam solar irradiance, boiler, or bore
B	Branch B on collector array
bo	Boiler outlet (collector array inlet)

bore	Bore of engine cylinder
b-st	Boiler steam (ullage space)
C	Carnot, branch C on collector array
cd	condenser
cl	Clearance
ci	Collector branch inlet
co	Collector branch outlet
coll	Collector
cond-ci	Condenser coolant-side inlet
cond-co	Condenser coolant-side outlet
cond-so	Condenser steam-side outlet
d	Down
D	Diffuse solar irradiance
dist	Distillate
e	Electrical
ei	Engine inlet
eo	Engine outlet (condenser steam-side inlet)
exp	Expansion
G	Solar energy
i	Inner, inlet, input, or initial
io	Input to output
ind	Indicated
m	Mechanical
M	Mechanical
ma	Mean to ambient
o	Outer, outlet, or output
p	Power, constant-pressure, or piston
p-low	Lower section of boiler pool
p-mid	Middle section of boiler pool
p-upp	Upper section of boiler pool
r	Reflector
s	Supply
sc	Annual mean value solar constant
str	Stroke
t	Total
th	Thermal
u	Useful, or up
uw	Untreated water
x	Displacement from specified datum

1 Introduction

1.1 Background

Stellenbosch University (SU) and the University of Southampton (UoS) are collaborating on the development of a novel low-temperature solar thermal co-generation system that purifies water and generates mechanical power or electricity. The system uses external compound parabolic concentrating (XCPC) solar collectors to convert solar radiation to useful heat, which is then used to generate steam in a boiler from fresh or brackish water. The steam is then used by a reciprocating steam expander, which utilises steam condensation in the condenser to generate mechanical power that can be converted to electricity (see Chapter 3.3 for explanation on condensing engine operating principle). The distillate is collected at the condenser outlet for human use. A simplified schematic of the system is shown in Figure 1.

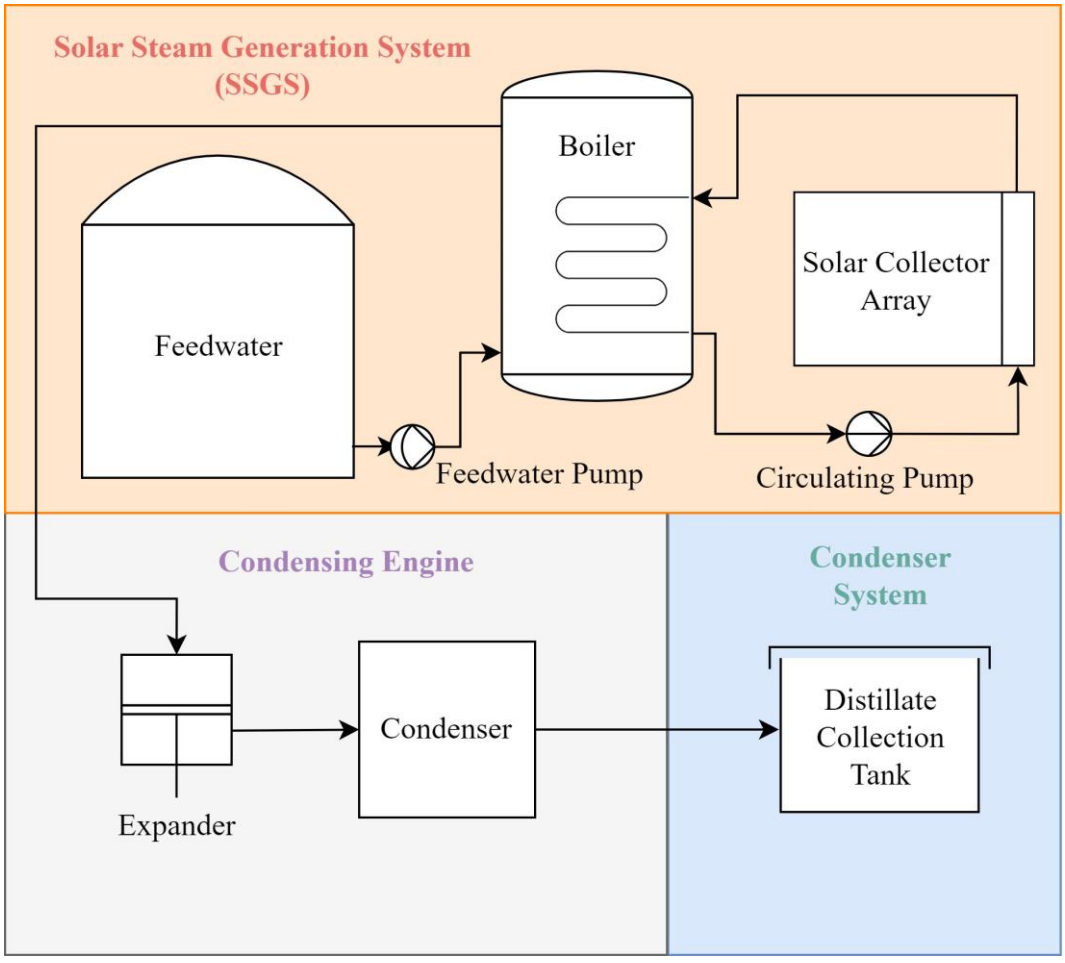

Figure 1 Simplified system schematic

The system aims to address the need for clean water and electricity identified in the United Nations (UN) Sustainable Development Goals (SDGs) 6 and 7. The Southern African Development Community (SADC) has been identified as a region of particular interest for the potential application of this type of system due to the significant need for sustainable clean water and energy supply in the region, large population living in remote rural areas, and the excellent solar resource in many parts of the SADC. The aim of this project was to develop a working proof-of-concept prototype to evaluate the technical feasibility of this concept.

1.2 Objectives

The objectives of this project were defined as follows:

1. Manufacture a reciprocating condensing engine expander designed by UoS.
2. Design and manufacture a solar steam generation system (SSGS) and condenser capable of generating and condensing, respectively, the steam required to run the condensing engine expander.
3. Design and manufacture a proof-of-concept prototype, incorporating the SSGS, expander, and suitable condenser.
4. Commission and test the prototype to determine the component and system performance.
5. Evaluate the feasibility of the concept based on the measured data and experience gained during the project.

1.3 Methodology

A formal engineering design process was followed, comprising:

1. Definition of customer requirements and conversion to engineering specifications.
2. Functional decomposition of the experimental system.
3. Concept generation, evaluation, and final selection.
4. Detailed design of the system.

The project included a significant practical component in the form of procurement, manufacturing, assembly, and installation of various equipment, including:

1. Purchase of bought-out parts for the condensing engine as per UoS specifications.
2. Purchase of bought-out parts for the rest of the system as per the detailed design conducted as part of this work.
3. Manufacturing of the condensing engine parts as per UoS specifications, as well as various components for the rest of the system as per the system detailed design.

4. Assembly of the condensing engine.
5. Installation of the condensing engine, SSGS, condenser, as well as the power and control system.
6. Commissioning of the components and overall system.

Finally, on-sun experimental testing was conducted to determine the performance of the experimental system and to evaluate the technical feasibility of the proposed concept.

1.4 Scope and Limitations on Scope

The primary responsibility of the author was to design, manufacture and test the SSGS and the overall system into which the condensing engine was to be incorporated. The condensing engine was designed by UoS, and the manufacture and assembly handled by SU under the guidance of the author as part of this project, with the objective of on-sun testing the entire system.

Unfortunately, the condensing engine did not function properly when integrated into the system. While significant effort was invested into getting the condensing engine to work, time constraints eventually necessitated that these efforts be abandoned for the time being, with the major issue being leakages on the cylinders preventing the requisite vacuum from forming. The focus of this thesis is thus on the performance of the SSGS and thermal system, the design of which was the responsibility of the author. The performance of the condensing engine was inferred using the measured performance of the thermal system and engine thermal efficiencies from literature to evaluate the overall concept.

1.5 Thesis Outline

Chapter 2 presents a literature review, which starts by providing an analysis of the need for water and energy in rural parts of the SADC and, in contrast, looks at the excellent solar resource in the region. It then goes on to discuss the use of low-grade heat for electricity generation and compares the organic Rankine cycle (ORC) to a condensing engine for this application. Thereafter, the process of water purification/desalination is considered, and it is subsequently shown that solar thermal collectors could be used to produce low-grade steam to drive the condensing engine for power generation and simultaneously subject the water to distillation for water purification/desalination (co-generation).

Chapter 3 discusses the governing theory needed to understand various technical aspects referred to or assumed to be understood by the reader in this thesis, covering various terminology, geometric definitions and theory pertaining to solar radiation and useful heat gain by solar collectors, particularly non-imaging concentrating

collectors; boiler theory which informed the boiler selection discussed in the detailed design of Chapter 4; as well as the operating principles of a reciprocating uniflow condensing engine.

Chapter 4 starts with the formulation of customer requirements and translation to engineering specifications, functional decomposition of the proposed system, and a summary of the concept selection process; followed by the detailed design of the system, which includes the solar collector array and boiler selection, sizing, and design, condenser selection and rating, condensing engine design, as well as the control and power system design.

Chapter 5 presents the performance metrics used as part of evaluating the technical feasibility of this system. The major outputs of the system are energy and clean water, so the performance metrics are concerned with the energy conversion from solar to either mechanical or electrical energy and the clean water production rate as a function of solar energy input (therefore also collector array size). Furthermore, the experimental testing used to determine the values of the performance metrics is described – namely, the experimental process for data collection, measurement equipment, and a discussion on data processing, considering systematic and random uncertainty in the data.

The measured data from three full-day on-sun tests, and the resulting values for the performance metrics for energy conversion and clean water production, are presented and analysed in Chapter 6, including an estimation of the monthly and annual performance of the system. The results are compared with existing solar-powered technology for electricity generation and water purification. Finally, a summary of system performance (compared to the project objects) is given at the end of the chapter. Finally, in Chapter 7, a conclusion is made as to the feasibility of the proposed concept, major outcomes, and areas for further investigation.

2 Literature Review

2.1 Water and Energy in Southern Africa

2.1.1 Electricity Shortage

The UN SDG 7 is to e***nsure access to affordable, reliable, sustainable, and modern energy for all*** (UN, 2022). In 2020, 733 million people globally were without access to electricity, of which 77 % live in Sub-Saharan Africa and the majority are situated in rural areas (UN, 2022). By May 2018, only 48 % of people living in the SADC had domestic access to electricity (Southern African Development Community & Southern African Research and Documentation Centre, 2018). Similarly, in 2020, the proportion of people in Sub-Saharan Africa without domestic access to electricity was 48.1 % (UN, 2022). Although Africa is experiencing the fastest rate of urbanisation globally, it is projected that 44 % of Africans will still be living in rural areas in 2050 (UN Department of Economic and Social Affairs, 2014). Therefore, rural areas in Sub-Saharan Africa appear to be a key area of need for development of basic electricity infrastructure for the foreseeable future.

The major power utility in the SADC is the South African state-owned utility, Eskom, which owns over 70 % of installed and operating capacity, and services over 70 % of the demand in the SADC (Southern African Power Pool, 2021). In 2021, coal-fueled thermal energy made up 81.3 % of the South African energy mix (Council for Scientific and Industrial Research, 2022). However, due to the aging of coal-fired plants, these are planned for large-scale decommissioning (Department of Public Enterprises Republic of South Africa, 2019). The South African Just Transition Framework plans for a move away from coal towards renewables, with acceleration of renewable energy infrastructure having started in 2021 and downsizing of coal production and employment in the coal sector planned to start in 2025 and accelerated from 2030 (Presidential Climate Commission, 2022).

Moreover, the demand for electricity in Southern Africa is expected to grow by 40 % from 2018 to 2028 (SARDC, 2018). When considering the capacity and make-up of energy infrastructure and the demand thereon in the SADC, as well as the efforts to move away from coal, it is apparent that there is an urgent need for further, more rapid, energy infrastructure development.

2.1.2 Clean Water Shortage

The UN SDG 6 is to e***nsure availability and sustainable management of water and sanitation for all*** (UN, 2022). By 2030, 1.6 billion people will not have access to safely managed water for drinking and 1.9 billion people will not have access to basic hygiene facilities (UN, 2022). By 2035, 40 % of the global population will be living in communities where the demand for clean water exceeds the supply (Guppy

and Anderson, 2017). To achieve access for all by 2030, the current rate at which access is being obtained must increase by 400 % (UN, 2022). In 2017, approximately 73 % of people in Sub-Saharan Africa did not use safely managed drinking water services (UN Educational, Scientific and Cultural Organisation and UN Water, 2021). Furthermore, in 2022, 80 % of people globally without access to clean water lived in rural areas (UN, 2022). In the *Africa Water Vision for 2025*, the link between water availability and socio-economic development is identified, such that inadequate access to safe water and sanitation perpetuates poverty and results in diminishing rates of economic development (UN Economic Commission for Africa, African Union Commission & Africa Development Bank, 2003). The need for development of safely managed water infrastructure in Africa, and particularly rural parts of Sub-Saharan Africa is evident in the high percentage of the population that lacks this basic human right, and the consequent impact that this has on the rate of socio-economic development and quality of life in the region.

2.1.3 Abundant Solar Resource

The *SADC Industrialisation Strategy and Roadmap 2015-2063* plans to utilise the abundant, diverse pool of natural resources from each of the member states to obtain reliable energy infrastructure and sustainable growth of the energy sector (SADC, 2015). Parts of the SADC possess abundant solar radiation suitable for the energy industry – most notably: Botswana, Namibia, and South Africa (International Renewable Energy Agency – IRENA, 2015). Certain technologies utilise the combination of beam and diffuse irradiance – namely, global irradiance – such as compound parabolic concentrating (CPC) collectors with low concentration ratios (see explanation on non-imaging concentrators in Chapter 3.1.2), as was used in this project.

In Figure 2, the annual global horizontal irradiation (GHI) power potential map is shown. From Figure 2, as well as the direct normal irradiation (DNI) and PV power potential maps – readily available from SOLARGIS (2022) – it is evident the SADC has significant potential for the development of solar-powered technology using beam and/or diffuse irradiance, depending on the application.

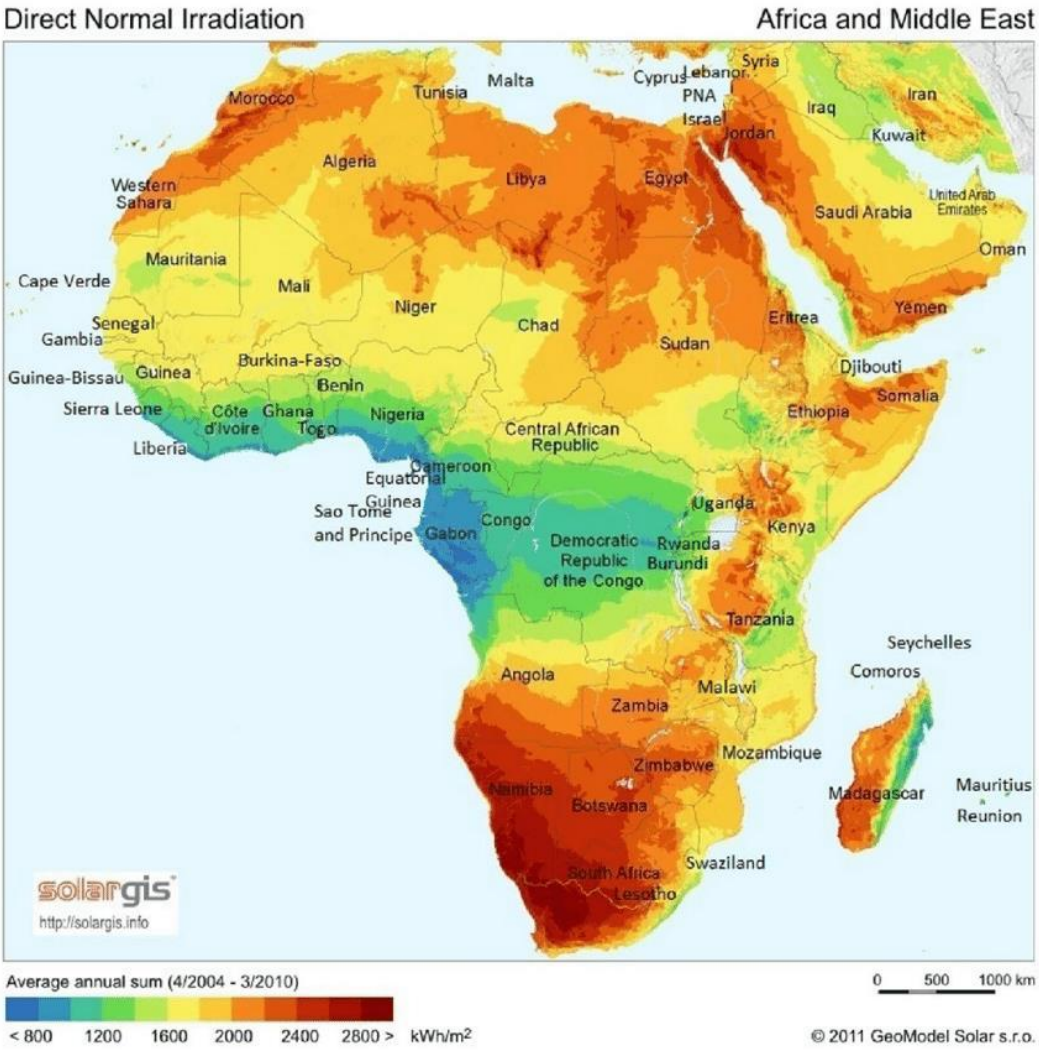

Figure 2 Africa map of annual GHI (SOLARGIS, 2022)

2.2 Low-Grade Heat to Electricity

2.2.1 Low-Grade Heat

Low-grade heat refers to usable heat at an operating temperature below a specified threshold, which is defined differently by various authors. For instance, Matsuda (2013): 150 °C; Müller and Howell (2021): 230 °C; and Bao et al. (2019): 250 °C. For this work, *low-grade* will refer to temperatures below 250 °C.

The utilisation of low-grade heat has gained much interest in recent years due to its occurrence as waste heat from many industrial processes (Bao et al. 2019). In addition to waste heat, other sources of low-grade heat exist, including renewable sources such as solar thermal energy (Müller and Howell, 2021).

2.2.2 Conversion of Low-Grade Heat to Power

The primary technology applied for conversion of low-grade heat to electricity has been heat engine systems – specifically ORCs (Bao et al., 2019). ORCs are similar to conventional steam Rankine cycles, but they use an organic working fluid with a low boiling point, such as a refrigerant or hydrocarbon (Frangoudakis et al., 2011). Other cycles suitable for low-grade heat to power exist – such as the Kalina cycle, which uses a mixture of ammonia and water as the working fluid and has superior performance over ORCs in some instances. However, in this chapter the ORC will be treated as the reference technology for low-grade heat-to-power systems, since it is the most established low-grade heat to power technology.

The condensing engine (reciprocating expander) offers an alternative to the ORC, using water as the working fluid and operating at approximately 100 °C and 1 bar (abs). The basic working principle of a condensing engine is that a low vacuum pressure is obtained in the engine cylinder during the exhaust process by condensation of steam in the condenser and atmospheric pressure is used as the driving force on the open side of the piston.

Müller and Howell (2021) compared the final known 19th-century, 0.735 kW condensing engine by Hathorn, Davey and Co. (Josse, 1885) to four ORC electricity generation systems from Landelle et al. (2017) with power ratings in the same range (0.5 to 1.4 kW). The condensing engine had a thermal efficiency of 3.7 %, which is low compared to the ORC systems, which ranged from 4.2 to 6.8 %.

However, due to the differing operating temperatures, it was more suitable to compare them in terms of the Second Law (exergy) efficiency, which is the thermal efficiency divided by the theoretical maximum (Carnot) efficiency. The Second Law efficiency (η_{II}) is defined in Equation (1), which is the standard expression for heat engines (Dincer and Kanoglu, 2010), where η_{th} is the thermal efficiency, and η_C is the Carnot efficiency.

$$\eta_{II} = \frac{\eta_{th}}{\eta_C} \tag{1}$$

The thermal (First Law) efficiency is defined in Equation (2), where $\dot{W}_o$ is the mechanical power output and $\dot{Q}_b$ is the thermal energy input (Atkins et al., 2018). In this project, $\dot{Q}_b$ was the rate of heat gain by the boiler from the collector array HTF.

$$\eta_{th} = \frac{\dot{W}_o}{\dot{Q}_b} \tag{2}$$

The Carnot efficiency is defined in Equation (3), where T_{cd} is the condensation (heat sink) thermodynamic temperature and T_b is the boiler (heat source) thermodynamic temperature (Atkins *et al.*, 2018).

$$\eta_C = 1 - \frac{T_{cd}}{T_b} \quad (3)$$

The Hathorn and Davey condensing engine had a Second Law efficiency of 24.7 %, and the four ORC systems varied from 20.1 to 35 %, illustrating that the 19th-century condensing engine is comparable with modern ORCs in terms of Second Law efficiency. Müller and Howell (2021) suggested that technological development since 1885 now allows for the use of expansion in the condensing engine and, therefore, the potential to increase the net thermal efficiency from 3.7 % (expansion ratio, r_{exp} = 1) to 9 % (r_{exp} = 4), which translates to a Second Law efficiency of 40 %, exceeding that of ORCs of a similar scale.

However, the experimentally determined thermal efficiencies determined by Müller et al. (2018) ranged from 2 to 5.5 % corresponding to the expansion ratios r_{exp} = 1 to 4, respectively. Since these values have been experimentally proven, they were used as the basis for estimating the mechanical output of the engine in this project, as discussed further in Chapter 5.1.1.3, instead of the higher theoretical values alluded to in Müller & Howell (2021).

The four ORCs considered in Müller and Howell (2021) had operating pressures ranging from 4.55 to 12.7 bar (abs), whereas the condensing engine uses steam near to 1 bar (abs) and is therefore not a pressurised system, reducing safety, manufacture, and maintenance costs, as well as making it simple to build and operate (Müller and Howell, 2021). Additionally, using water has certain benefits compared to organic fluids, in that it is non-toxic, non-flammable, and in most cases cheaper and more readily available (Müller, 2017).

In 2017, 9 % of ORCs in practice used solar energy as a heat source (Landelle *et al.*, 2017). However, up to now there has been no research on solar thermal driven condensing engines as an alternative to solar-powered ORC systems.

Table 1 shows the typical operating temperatures of different types of solar thermal collectors. All except the flat plate collector can theoretically produce fluid temperatures above 100 °C but typically not much over 250 °C. Therefore, most of the listed solar thermal collectors produce low-grade heat, and many can produce steam at atmospheric pressure or higher, including non-tracking collectors, which offer simplicity and lower cost compared to tracking systems.

Table 1 Solar thermal collector types and typical operating temperatures

Motion	Collector Type	Temperature (°C)
Stationary	FPC – flat plate collector	30-80
	ETC – evacuated tube collector	50-200
	CPC – compound parabolic concentrator	60-240
	XCPC – external CPC	60-300
Single-axis tracking	CPC – compound parabolic concentrator	60-300
	LFR – linear Fresnel reflector	60-250
	CTC – cylindrical trough collector	60-300
	PTC – parabolic trough collector	60-400
Two-axis tracking	PDR – parabolic dish reflector	100-1500
	HFC – heliostat field reflector	150-2000

Note: all the values in Table 1 were obtained from Kalogirou (2014), except that of the XCPC, taken from Jiang *et al*. (2017).

Furthermore, Müller and Howell (2021) suggest the condensing engine has the potential to be used for combined electricity generation and water desalination, since water is used as the working fluid and is subjected to a distillation process, whereby liquid water is boiled, and the pure water vapour is condensed. If the condensate is collected and removed from the system rather than recirculated to the boiler, then distilled water becomes a product of the system. This could be a unique application in which condensing engines might be more suitable than systems that use organic fluids, such as ORCs.

2.3 Desalination and Water Purification

2.3.1 Clean Water

Potable water refers to water suitable for human consumption (Ahuja, 2021), and implies safe levels according to a wide variety of metrics – for instance, salinity, pH, hardness, chemical and heavy metal concentration (Ahuja, 2021), as well as pesticides, pathogenic bacteria, viruses, and protozoa (Kalogirou, 2014). Therefore, water that has unsafe levels by any of these metrics, must be treated to become potable. Note that in this project, distillation was used to generate distilled water, which we will refer to as clean water, as it has been purified of contaminants, but needs to be remineralised to make it truly potable.

2.3.2 Desalination

Desalination is the process by which dissolved salts are removed from saline water so that potable water may be recovered (Panagopoulos, 2021). It is otherwise also defined as the process by which dissolved solids are removed from sea-, brackish

or treated wastewater (Khan et al., 2013), and is typically performed at water temperatures in the range of 60 to 90 °C (Christopher et al., 2019). Desalination processes can be classified as one of three types: (1) *phase change* – distillation or freezing; (2) *semi-permeable membrane* – reverse osmosis (RO) or electrodialysis (ED); and (3) *chemical* – chlorination, iodine treatment etc. (Rasul *et al.*, 2013). The demonstration system investigated in this project is a form of distillation-type phase-change water desalination.

Conventional desalination solutions are effective yet energy intensive and the continuous use of non-renewable energy sources is unsustainable, threatening energy security in the long term and causing greenhouse gas emissions. Renewable energy, such as solar, has potential as a sustainable alternative (International Bank for Reconstruction and Development, 2012).

Various solar desalination technologies exist and are classified as either direct or indirect. Indirect systems use solar energy to generate either the heat or electricity used for processes such as Reverse Osmosis (RO), Multi-Effect Distillation (MED), or Multi-Stage-Flash (MSF) desalination. In contrast, direct solar desalination systems are those where distillation occurs in the solar collection system itself, such as with solar stills, which use evaporation and condensation in the collector system to separate the salt and water (Rasul *et al.*, 2013). The most commonly occurring desalination technologies are RO and MSF (Kalogirou, 2014).

Photovoltaic reverse osmosis (PV-RO) and ED have shown to have the lowest specific energy consumption (SEC, kWh/m^3) for solar desalination. PV-RO and ED (as well as Reverse ED) typically have SECs in the range 0.5 to 3 kWh_e/m^3 and 1 to 3.5 kWh_e/m^3, respectively (Stillwell and Webber, 2016). Assuming an average PV (solar to electrical) efficiency of 15 % (Mehmood et al., 2019), this would equate to 4 to 25 kWh_{solar}/m^3, and 8 to 30 kWh_{solar}/m^3, for PV-RO and ED, respectively. Assuming an average PV efficiency of 15 % and average solar to thermal efficiency of 50 %, the SEC of MSF is between 48 and 80 kWh_{solar}/m^3, and for MED is between 38 and 55 kWh_{solar}/m^3 (Kalogirou, 2014).

Therefore, existing desalination technologies have SECs comfortably below 100 kWh_{solar}/m^3, and the low-SEC technologies (PV-RO and ED) operate between 4 and 30 kWh_{solar}/m^3.

2.3.3 Solar Distillation

Distillation is one way of addressing most of the contaminants listed in Chapter 2.3.1, specifically the removal of inorganic compounds, such as metals, and hardness (calcium and magnesium). It involves vaporising the contaminated water and removing the steam to leave behind the non-volatile components such as metals and salts.

Furthermore, distillation is useful for inactivation of micro-organisms, such as bacteria and certain viruses (Kamrin, 1990). Thermal inactivation is a well-known

technique for treating water to reduce microbial load and involves exposing the microorganism to elevated temperatures for an extended period (Coombes et al., 2006). An extensive list of pathogens (disease-causing microorganisms) is given by WHO (2015) with accompanying temperatures and exposure times for inactivation, as presented in Figure 3 (constructed from WHO (2015)).

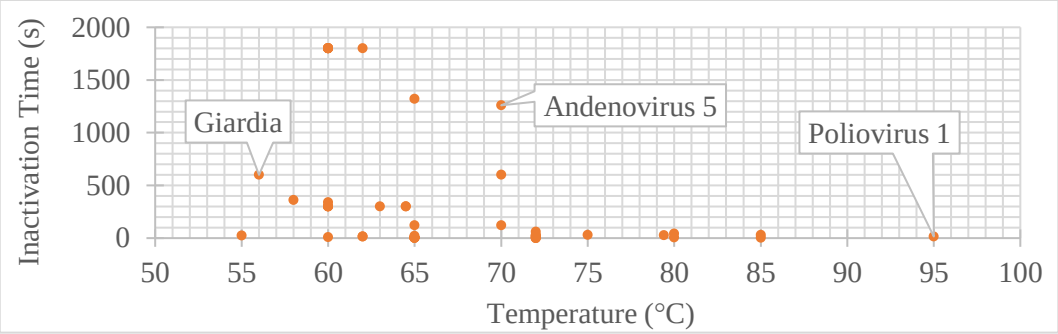

Figure 3 Inactivation time and temperature for various bio-contaminants

The required exposure time varies significantly for different organisms and at different temperatures – the apparent trend is that deactivation time decreases significantly with increasing temperature. Based on the temperature range in Figure 3, low-grade heat appears to be suitable for thermal inactivation of bio-contaminants and increases in effectiveness with increasing temperature.

Distillation with low-grade heat is therefore a relatively comprehensive solution for removal of typical contaminants from water, since it purifies the water of inorganic compounds by the process of boiling separation, and bio-contaminants by deactivating them as they are exposed to elevated temperatures.

Furthermore, solar thermal distillation is a well-established technology with various solar thermal collectors suitable for use as the heat source (Kalogirou, 2014). As such, solar thermal distillation is a relatively comprehensive and sustainable solution for the purification of water, and it is an attractive solution in the context of the SADC due to the excellent solar resource in large parts of the region.

However, it should be noted that distillation is unsuitable to remove organic compounds with lower boiling points than water, such as benzene and toluene (Kamrin, 1990), and might increase their concentration. Benzene (Agency for Toxic Substances and Disease Registry, 2007) and toluene (Agency for Toxic Substances and Disease Registry, 2017) are a concern if the water source has been contaminated by such causes as industrial discharge and gasoline spills.

2.4 Conclusions from Literature Review

The SADC is an area with significant need for clean water and energy, particularly in rural areas. On the other hand, large parts of the SADC possess a rich renewable energy resource in the form of solar radiation. It is in this context that a novel concept for solar-powered co-generation of clean water and energy is being investigated.

Low-grade heat occurs frequently as waste heat or from renewable energy technologies such as solar thermal collectors, particularly non-tracking collectors. The most established technology for utilising this low-grade heat for power generation is the organic Rankine cycle, but the condensing engine is a possible alternative, which uses water (steam) as the working fluid. If the water is supplied on an open loop, it is subjected to a distillation process and distilled water is produced as a system output.

Therefore, the condensing engine could potentially be used for combined power generation and water purification and the system therefore offers a potentially elegant solution in the context of the UN SDGs 6 and 7.

3 Governing Theory

This chapter introduces theory that is either referenced, required for understanding or useful as background in Chapters 4 and 5 – namely, the system design and system performance metrics, respectively.

3.1 Solar Collector Operation

3.1.1 Solar Irradiance

Solar irradiance, also known as insolation, is the instantaneous rate at which solar energy is incident on a unit area, typically measured in W/m^2. Solar irradiation is the amount of solar energy incident on a unit area over a specified period, which is the integral of irradiance with respect to time, typically measured in kWh/m^2.

The radiative solar energy incident per unit time on a unit surface area positioned outside the earth's atmosphere and faced perpendicular to the line of propagation of the radiation varies between 1330 and 1400 W/m^2 annually, as per Equation (4),

$$G_0 = G_{sc}\left[1 + 0.033\cos\left(\frac{360}{365}N\right)\right] \tag{4}$$

where G_{sc} = 1366.1 W/m^2 is the annual mean of the solar constant G_0, and N is the numeric day of the year. (Kalogirou, 2014).

In the atmosphere, portions of G_0 are absorbed, reflected, scattered, or transmitted directly. Consequently, the concentration of solar irradiance at the surface of the earth is lower than G_0 and it consists of the directly transmitted component known as beam irradiance, and the scattered component known as diffuse irradiance. The sum of the beam and diffuse components is the global or total irradiance. (Kalogirou, 2014).

Direct normal irradiance (DNI) is the beam irradiance on a surface facing directly towards the sun, perpendicular to the incident radiation. Diffuse horizontal irradiance (DHI) is the diffuse irradiance on a horizontal surface. Global horizontal irradiance (GHI) is the total of beam (DNI $\cdot \cos\vartheta$) and diffuse irradiance (DHI) on a horizontal surface.

The irradiance on a solar collector, beam or diffuse, is affected by the collector tilt angle relative to the ground and the collector's azimuthal orientation. Figure 4 illustrates some important solar angles used when relating a tilted surface to the position of the sun, which are listed in Table 2.

Table 2 Definitions of symbols in Figure 4

Symbol	Definition
β	Collector surface tilt angle relative to the horizontal
ϑ	Solar incidence angle, which is the angle between the DNI on a collector aperture and the normal to the aperture
ϕ	Solar zenith angle
z	Solar azimuth angle
Z_s	Surface azimuth angle

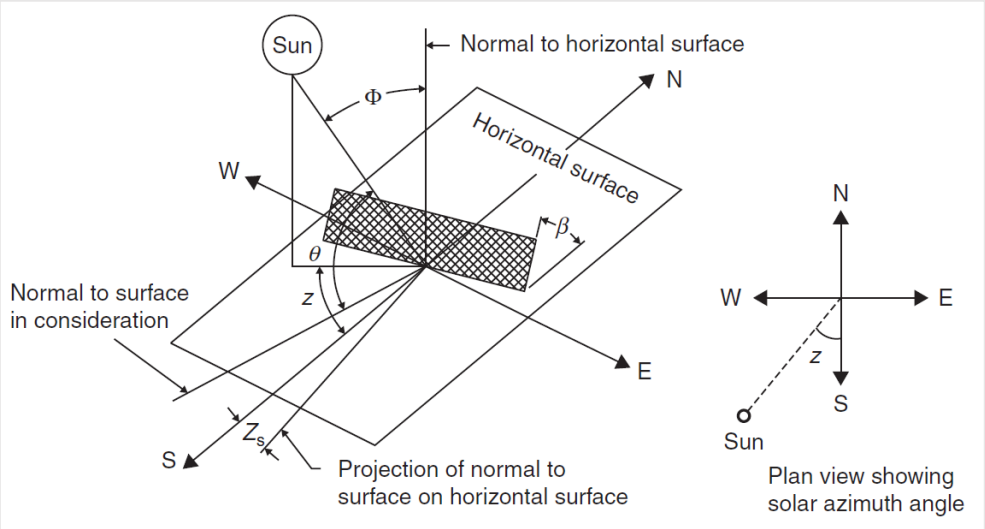

Figure 4 Solar angles relative to a tilted surface (Kalogirou, 2014)

Beam irradiance, corrected for collector tilt, ($G_{b,T}$), is reduced from the DNI by the factor $\cos\vartheta$, according to Equation (5) (Beckman and Duffie, 2013). The calculation of ϑ is described in various literature but was not required in this project, as the global tilt (in-plane) irradiance was directly measured using a pyranometer, so Equations (5) to (8) are shown for illustration purposes only and were not required in this project.

$$G_{b,T} = DNI \cos\vartheta \tag{5}$$

Diffuse irradiance, corrected for collector tilt, ($G_{d,T}$) is reduced from the DHI by the sky view factor (SKV) as per Equation (6), based on the isotropic diffuse model from Liu and Richard (1963).

$$G_{d,T} = DHI \cdot SKV \tag{6}$$

The sky view factor describes the fraction of the full hemispherical sky that is visible to the collector aperture, at its respective tilt (inclination) angle (β), as per Equation (7) (Liu and Richard, 1963).

$$\mathrm{SKV} = \frac{1 + \cos\beta}{2} \tag{7}$$

The global tilt irradiance (GTI) is defined as per Equation (8) (Loutzenhiser et al., 2007) as the sum of the beam, diffuse, and albedo (ground-reflected) components, corrected for collector tilt. In the case of the XCPC, the view factor to the ground is negligible, and thus the contribution of the albedo component ($G_{alb,T}$) would have been negligible in the actual GTI that was measured.

$$\mathrm{GTI} = G_{b,T} + G_{d,T} + G_{alb,T} \tag{8}$$

3.1.2 Non-Imaging Concentrators

The concentration ratio of a solar collector is the ratio of the aperture area to the absorber/receiver area, as defined in Equation (9) (Kalogirou, 2014).

$$C = \frac{A_a}{A_r} \tag{9}$$

Non-imaging concentrators are solar collectors with low concentration ratios, not reproducing the image of the radiation source because the incident radiation is reflected widely onto the receiver. All the incident radiation, both diffuse and beam, with incidence angles smaller than the acceptance half-angle is reflected onto the receiver. Linear non-imaging collectors typically have concentration ratios below 10. (Beckman and Duffie, 2013).

Collectors with concentration ratios below 3 can accept a large amount of diffuse radiation, and those with concentration ratios below 2 typically do not require any tracking, such as the collector used in this experimental system (C = 1.4), whereas from 3 upward tracking requirements start at biannual frequency. (Kalogirou, 2014).

3.1.3 Useful Heat Gain and Efficiency

The efficiency of a solar thermal collector is defined in Equation (10) as is the ratio of the useful heat gain to the incident solar energy (Beckman and Duffie, 2013), where $\dot{Q}_u$ is the useful heat gain, G_t is the total irradiance, which in the case of this experiment was the global tilt irradiance (GTI), and A is either the gross collector area or the aperture area, corresponding to the area used to calculate $\dot{Q}_{gain}$ in Equation (15) – the appropriate area is usually selected by the collector calibrator.

$$\eta_{coll} = \frac{\dot{Q}_u}{G_t A} \tag{10}$$

The useful heat gain is theoretically defined in Equation (11) as the difference between the solar radiation absorbed by the collector heat transfer fluid (HTF) after optical losses ($\dot{Q}_{gain}$) and the heat loss from the collector ($\dot{Q}_{loss}$) (Beckman and Duffie, 2013) due to convection and radiation losses from the absorber tube, and conduction losses from the supply and return header tubes. The useful heat gain may also be determined directly using Equation (12),

$$\dot{Q}_u = \dot{Q}_{gain} - \dot{Q}_{loss} \tag{11}$$

$$\dot{Q}_u = \dot{m}\, c_p\, \Delta T_{io} \tag{12}$$

where $\dot{m}$ is the mass flowrate of the HTF, c_p is the specific heat capacity of the HTF at the mean collector temperature (T_m), which is the mean of the HTF temperatures at the inlet and outlet of the collector, defined in Equation (13), and ΔT_{io} is the HTF temperature difference between the collector inlet and outlet.

$$T_{HTF,m} = \frac{T_{HTF,out} + T_{HTF,in}}{2} \tag{13}$$

$\dot{Q}_{gain}$ and $\dot{Q}_{loss}$ are defined in Equations (15) and (16), respectively; where A is either the gross or aperture area, η_0 is the optical efficiency defined in Equation (17), a_1 and a_2 are the empirical heat loss coefficients, respectively, and ΔT_{ma} is the difference between the mean collector temperature and the ambient temperature (Equation (14)), which represents the driving force for all forms of heat loss from the collector. The optical efficiency and heat loss coefficients are constants typically available in the datasheets of collectors. This information can then be used when comparing different collectors at the expected operating temperatures and irradiance levels.

$$\Delta T_{ma} = T_{HTF,m} - T_a \tag{14}$$

$$\dot{Q}_{gain} = \eta_0 G_t A \tag{15}$$

$$\dot{Q}_{loss} = A(a_1\, \Delta T_{ma} + a_2\, \Delta T_{ma}{}^2) \tag{16}$$

The optical efficiency of a collector, defined in Equation (17), is the fraction of incident solar radiation ($G_t A$) absorbed as heat gain by the collector absorber excluding heat loss ($\dot{Q}_{gain} = \dot{Q}_u - \dot{Q}_{loss}$), depending on factors such as the reflectivity of a reflector, transmissivity of the glass of evacuated tubes or flat plate

collector covers, absorptance of the receiver, angles of incidence, and the geometry of the collector. (Kalogirou, 2014).

$$\eta_0 = \frac{\dot{Q}_{gain}}{G_t A} \tag{17}$$

3.1.4 Collector Flowrate Estimation

Setting Equation (11) (collector useful heat gain formula) equal to Equation (12) (enthalpy change in collector/s) and rearranging, Equation (18) is obtained for the collector mass flowrate.

$$\dot{m} = \frac{c_p \, \Delta T_{io}}{A \, (\eta_0 G_t - \, a_1 \, \Delta T_{ma} + \, a_2 \, \Delta T_{ma}{}^2)} \tag{18}$$

3.2 Pool Boiling

Figure 5 is the Nukiyama pool boiling curve for water at atmospheric pressure, which represents the relationship between excess temperature (ΔT_{excess}), defined in Equation (28), and heat flux $\dot{q}_{boiling}$. ΔT_{excess} is the difference between the surface temperature (which in the case of this project was the outer surface of the helical coil tube) and the saturation temperature of the liquid being boiled.

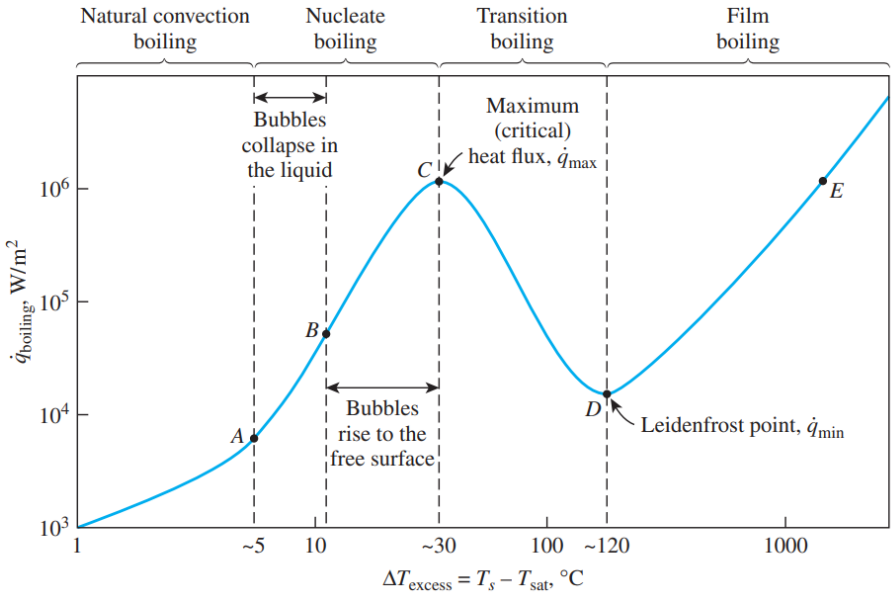

Figure 5 Nukiyama boiling curve for water at 1 atm (Cengel and Ghajar, 2015)

$$\Delta T_{excess} = T_s - T_{sat} \quad (19)$$

The boiling curve is dependent primarily on the liquid pressure and the combination of heating surface material and liquid. In the case of pool boiling, it is practically independent of the heating surface geometry (Cengel and Ghajar, 2015). Therefore, the characteristics of the curve are applicable to this experiment. The boiling curve has four distinct regimes – natural convection, nucleate, transition and film. The transition and film regimes are undesirable due to their instability and lower heat transfer coefficients. Burnout was not a relevant risk due to the nature of the heat source. As such, the excess temperature limit of ~30 °C represented an important design parameter in the context of this project.

3.3 Condensing Engine Operation

3.3.1 Thermodynamic Cycle

A single cycle of a uniflow reciprocating engine, referring to each single piston, consists of a downward and upward stroke equating to five thermodynamic processes, as presented in Figure 6 and Table 3.

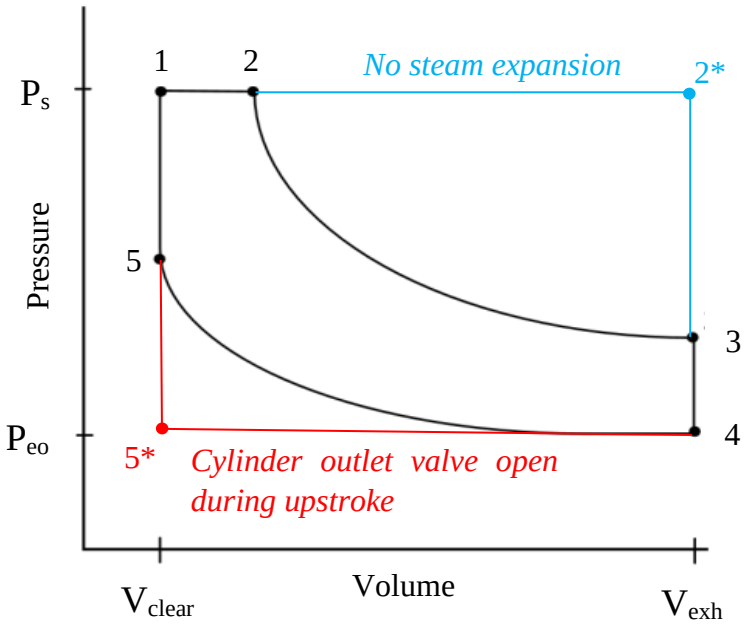

Figure 6 P-V diagram for full condensing engine cycle

Each process is typically considered as quasi-static, such that the energy of the steam at any point is equal to the internal energy and not the enthalpy (Bannister, 1991).

Table 3 Condensing engine cycle constituent processes

Designation	Process	Means
5 to 1	Intake	Constant volume
1 to 2	Intake	Constant pressure
1 to 2*	Intake	Constant pressure
2 to 3	Expansion	Constant temperature
3 to 4	Exhaustion	Constant volume
4 to 5	Compression	Constant temperature
4 to 5*	Exhaustion	Constant pressure

Figure 7 (UoS CAD) defines the characteristic dimensions of a condensing engine cylinder, which will be referred to subsequently.

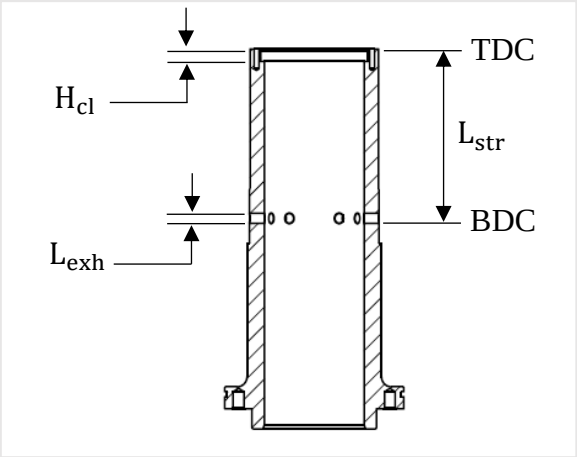

Figure 7 Definition of primary cylinder dimensions

For the following discussion of the condensing engine cycle, the general sequence of the engine cycle was taken from Bannister (1991), who gives a comprehensive description of the cycle of a uniflow reciprocating engine, and the adaptations are clearly stated for the condensing engine considered in this study. The figures used in this explanation were created by the author. Please refer to Figure 6 for the following explanation.

At 5, the piston is at top dead centre (TDC) and the steam in the cylinder is that which remained after exhaustion from the vents and was recompressed during the upstroke. However, for the engine used in this project the outlet valve remains open during the upstroke, so the pressure at 5 equals the condenser pressure, instead being 5*.

From 5 to 1, steam is admitted into the clearance space between the piston and cylinder at TDC, as shown in Figure 8 (a), typically modelled as an instantaneous constant-volume pressure rise up to the supply pressure. From 1 to 2, the piston

moves downward from TDC, and steam supply continues until the piston has traversed the entire admission length, at which point the inlet valve closes, as shown in Figure 8 (b) and Figure 9 (a). When steam expansion is not used, the inlet valve remains open for the entire downstroke (TDC to BDC), such that 2 becomes 2*.

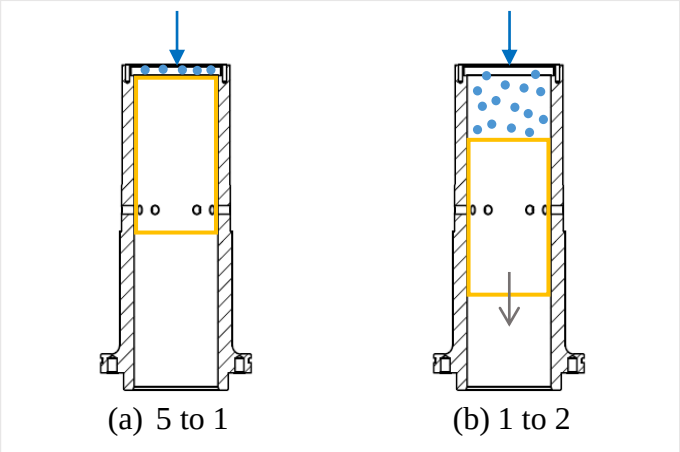

Figure 8 Condensing engine intake

The process 2 to 3 is relevant when steam expansion is used. State 2 represents the instance at which the inlet valve is closed and expansion begins, as shown in Figure 9 (a). From 2 to 3 the piston traverses from the position of valve closure to bottom dead centre (BDC), as shown in Figure 9 (b). The engine used in this experiment was fitted with a steam jacket for near-isothermal expansion.

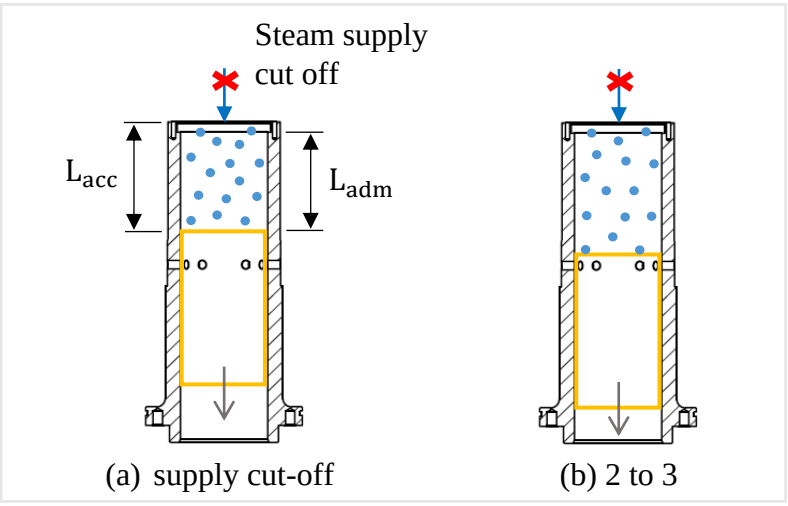

Figure 9 Condensing engine expansion

The expansion ratio (r_{exp}) is defined in Equation (20) (Bannister, 1991),

$$r_{exp} = \frac{L_{acc}}{H_{cl} + L_{str}} \tag{20}$$

where, as illustrated in Figure 9 (a), L_{acc} is the acceptance length (measured from TDC), H_{cl} is the clearance height, and L_{str} is the stroke length – see also Figure 7.

The cut-off ratio ($r_{cut-off}$), defined in Equation (21) (Bannister, 1991), is the ratio of the admission length to the stroke length – in other words, the percentage of the stroke over which the inlet valve is open.

$$r_{cut-off} = \frac{L_{adm}}{L_{str}} \tag{21}$$

A higher expansion ratio corresponds to a lower cut-off ratio – and both imply steam has more opportunity to expand during the downstroke, which increases engine thermal efficiency (more work done per unit volume steam generated).

At 3 the steam-side face of the piston is in line with the top edges of the exhaust ports and steam exhaustion through the ports takes place, as shown in Figure 10 (a). The process 3 to 4 is typically modelled as an instantaneous constant-volume exhaust process, during which the steam-side face of the piston moves down to the bottom edge and back up to the top edge of the exhaust ports, allowing steam to evacuate through the ports to the condenser. 3 to 4 will be referred to as the primary exhaust process.

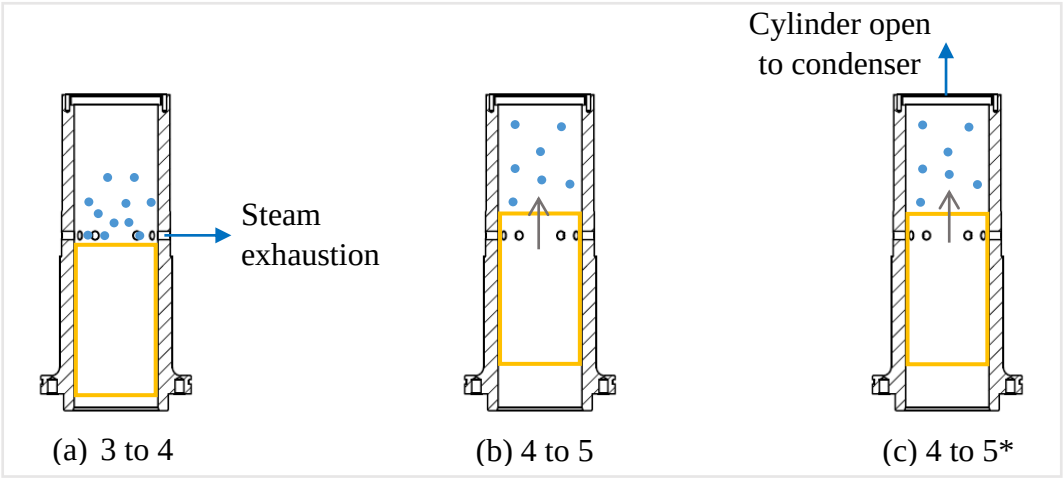

Figure 10 Condensing engine (a) primary exhaustion, (b) recompression, and (c) secondary exhaustion

From 4 to 5, the steam remaining in the cylinder is compressed as the piston moves from the top of the exhaust ports back to TDC, as shown in Figure 10 (b). If the cylinder is open to the condenser during this process, such as for the engine in this experimental system, then steam is exhausted (secondary exhaustion) in a constant-pressure process – 4 to 5*, as shown in Figure 10 (c). The exhaust processes – both 3 to 4 and 4 to 5* – are fundamentally dependent on the pressure drop from the cylinder to the condenser to drive steam out of the cylinder. Therefore, the lower the steam-side condenser pressure, the more effective the exhaust process.

3.3.2 Engine Power Output

The engine shaft output power ($\dot{W}_o$) is determined from the speed (ω_o) and torque (T_o) measurements according to Equation (22) ($\dot{W}_o$ is an average value calculated for each piston cycle), where the speed and torque were both intended to be measured variables, but unfortunately were not obtained since the engine did not run as intended.

$$\dot{W}_o = T_o \omega_o \tag{22}$$

The work performed on the piston per cycle (W_{ind} in Joules) by steam and atmospheric air, referred to as the cyclic indicated work, is defined in Equation (23) as the sum of the work done on the downstroke (W_d) and upstroke (W_u). (Senft, 1987).

$$W_{ind} = W_d + W_u \tag{23}$$

For the case of no expansion, W_d and W_u are defined in Equations (24) and (25), respectively (Müller *et al.*, 2018),

$$W_d = (P_s - P_{atm})\, A_{pf} \cdot L_{str} \tag{24}$$

$$W_u = (P_{atm} - P_{eo})\, A_{pf} \cdot L_{str} \tag{25}$$

where, P_s is the steam pressure as it enters the engine cylinder, P_{eo} is the low-vacuum condenser (engine exhaust) pressure, P_{atm} is atmospheric pressure, A_{pf} is the piston face area and L_{str} is the stroke length. In essence, for Equations (24) and (25), the respective net pressures are multiplied by the face area to give the net force, which is multiplied by the stroke length to give the work done by the net force on the down- and upstroke, respectively.

For the case of steam expansion, Equation (24) is adapted to use L_{acc} instead of L_{str} for the constant pressure process from 1 to 2 (see Figure 6), and the steam expansion work must then also be added, which similarly uses Equation (24) but with $L_{str} - L_{acc}$ instead of L_{str} and with variable P_s, which reduces from the initial value

along the isothermal expansion line 2 to 3 in Figure 6 as the steam expands and the piston continues downward. (Müller *et al.*, 2018).

The cyclic average indicated power ($\dot{W}_{ind}$) is defined in Equation (26) as the product of the piston cyclic indicated work and the cycle frequency (ω_{cycle} in rad/s).

$$\dot{W}_{ind} = W_{ind} \cdot \omega_{cycle} \tag{26}$$

Furthermore, the shaft work (W_o), which is the indicated work minus the mechanical friction losses, is related to the indicated work by the mechanical efficiency, which may also be expressed as the ratio of the cyclic average shaft power and cyclic average indicated power in Equation (27). (Senft, 1987).

$$\eta_M = \frac{W_o}{W_o + E_{m,loss}} = \frac{\dot{W}_o}{\dot{W}_{ind}} \tag{27}$$

Unfortunately, since the engine did not operate, the system mechanical energy output was estimated using thermal efficiencies from literature, as discussed in Chapter 5.1.

4 System Design

4.1 Customer Requirements to Engineering Specifications

The system was designed according to the engineering specifications set out in this sub-chapter. Table 4 shows the "customer requirements" and the derived engineering specifications (Dieter and Schmidt, 2013).

Table 4 Customer requirements and engineering specifications

Customer Requirement	Engineering Specification
1. The engine maximum required steam flowrate (two cylinders, no expansion) is 4.36 L/s (vapour) at 1 bar (abs), which equates to 2.56 g/s.	1.1. The system must generate steam at or above 2.56 g/s for at least four hours (arbitrarily chosen, sufficient to demonstrate the working of the prototype) on a sunny summer's day (peak GTI > 1000 W/m^2 and negligible intermittent cloud cover). 1.2. The system must have the capacity to condense steam up to a flowrate of 2.56 g/s.
2. The engine requires a minimum steam supply pressure of 0.8 bar (abs).	2. The system must maintain a supply pressure above 0.8 bar (abs) at flowrates up to the engine maximum supply rate (2.56 g/s).
3. The engine requires a condenser pressure below 0.074 bar (abs).	3. The system must condense the steam and subcool to below 40 °C (saturation pressure at 0.074 bar (abs)) at flowrates up to the engine maximum supply rate (2.56 g/s), which gives an associated pressure differential across the engine piston of 1.01325 – 0.074 bar = 0.94 bar.
4. The engine should operate without needing pressure vessel commissioning.	4. The maximum allowable boiler pressure is 1.5 bar (abs).
5. The system should allow for independent testing of components / sub-systems.	5. The system must be equipped to provide steam at the design flowrate (2.56 g/s) without solar heat.
6. The system should be safe.	6. The system design should be safe according to relevant standards –

	SANS 347:2012, SANS 460:2011, TIASA:2001.
7. The system should be simple enough to operate and maintain by locals in a remote area.	7. The system should require minimal intervention once installed and maintenance should be possible with minimal training.

4.2 Functional Decomposition

Figure 11 shows the functional decomposition derived from the engineering specifications in Table 4, starting at the primary function of the system, which is to co-generate distilled water and power from untreated water and solar radiation, down to each of the various sub-functions needed to achieve this, as well as to test the engine with constant-rate steam supply using auxiliary heating. (Dieter and Schmidt, 2013)

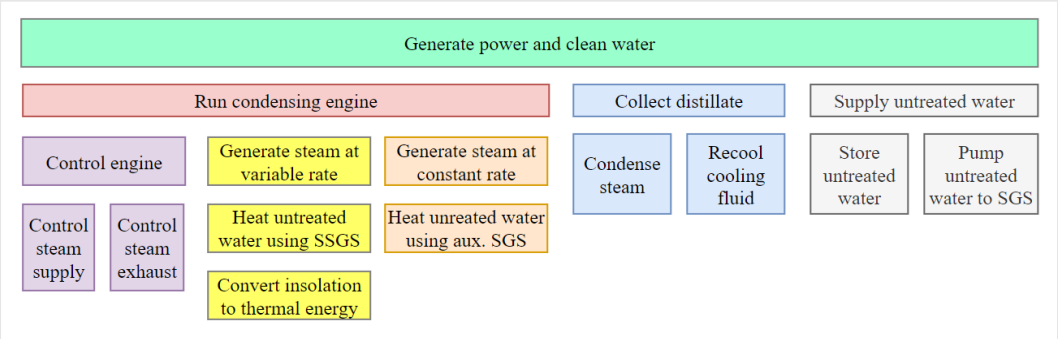

Figure 11 Functional decomposition of experimental system

4.3 Concept Selection

The overall system concept – namely, a solar powered steam expander – was prescribed, along with the specific engine design. Concept generation was thus limited to the components described in Table 5, with the associated selection decisions. (Dieter and Schmidt, 2013).

Table 5 Concept selection decisions

Component	Type	Operation
Solar collector	• Tracking vs non-tracking. • ETC vs CPC, XCPC.	• Direct vs indirect steam generation. • Forced vs natural convection flow.

		• HTF – water vs organic fluid; demineralised water vs municipal water
Boiler	• Kettle vs high-efficiency boilers (e.g., shell-and-tube)	• Pumped vs elevated-tank supply
Condenser	• Water- vs air-cooled. • Use of existing vs purchase of new.	• N/A

The final concept was determined by several iterations, entailing discussions with UoS, solar collector suppliers and boiler manufacturers, and evaluation according to the engineering specifications.

- Only non-tracking collectors were considered, due to the cost and complexity added by tracking in design, installation, and maintenance. The ETC, CPC and XCPC types all appeared suitable based on their operating temperatures (see Table 1) and typical use without tracking.
- Indirect steam generation was selected, upon recommendation of collector suppliers, to avoid excessive fouling in the absorber tubes by recirculating the same fluid in the collector array.
- Water was selected as the collector HTF because it is easily accessible and safe compared to thermal oils, which are typically flammable and expensive. In terms of thermal properties and the required steam supply temperature and pressure as per the engine operating requirements, the detailed design process confirmed that pressurised liquid water was a suitable selection.
- Demineralised water is preferred to municipal (mineral) water for long-term operation of the system because the low mineral content prevents fouling, and the system outputs demineralised water which may be used to refill or supplement the HTF if needed. However, for this project municipal water was more convenient and readily available, and sufficient for the purpose of demonstration.
- Forced circulation in the collector array was selected to allow for more accurate control of flowrate. Furthermore, the cost of a small medium temperature (up to 130°C) circulating pump was predicted to be lower than the cost to enable natural convection circulation, which would require a structure to raise the boiler above the collector array, as well as the engine to minimise piping between the boiler and engine.
- A kettle-type boiler was selected for simplicity.
- Pumped supply of untreated water to the boiler was selected over supply from an elevated tank because the supply tank would need to be raised at least five meters to overcome the maximum boiler back-pressure (1.5 bar (abs)). It also

allows easier control and monitoring of the quantities of cold water added (without a flowmeter), which is required to protect against quenching the boiler.
- Water cooling was selected for the condenser due to the convenience of the existing water reticulation system at the SU Solar Rooftop Laboratory, which allows for supply of water to the condenser, including recooling.
- A double-pipe heat exchanger was available for use. Made of stainless steel, it was suitable for this outdoor application where it would be exposed to a range of corrosive weather conditions. A rating calculation suggested it had sufficient cooling capacity for this project.

The focus of this project was a proof-of-concept prototype, and so some of the selected components may not be ideal for optimising the eventual system but were appropriate in the context of this study.

4.4 Detailed Design

This chapter presents the detailed design of the system, which entailed the sizing and detailing of the collector array and boiler, as well as the selection and rating of the condenser. The P&ID of the final design is shown in Figure 12. For neatness, the single inlet pipe (with a manual ball valve) on the collector array outlet header and the three outlet pipes (each with a manual ball valve) on the collector array inlet pipe, for filling and emptying the collector array at its high and low points, respectively, were omitted.

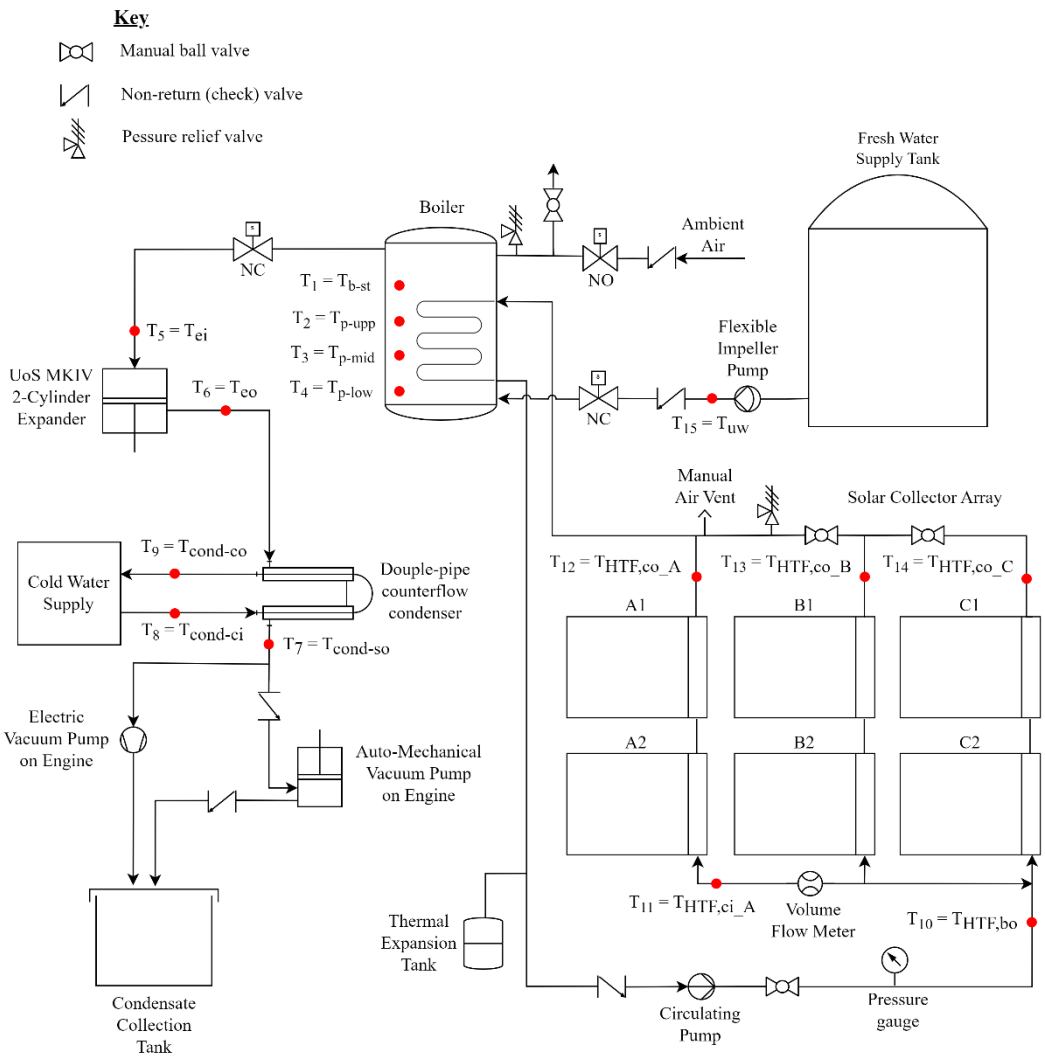

Figure 12 System P&ID

4.4.1 Solar Collector Array

4.4.1.1 Heat Transfer Fluid

The HTF water was kept in the liquid phase – firstly, for safety reasons, since production of steam in a closed collector loop could result in excessive pressure rise; and, secondly, to use controllable forced circulation in the collector array, which requires a single-phase liquid for the circulating pump to operate. The HTF was maintained in the liquid phase by pressurising to ~5 bar (abs), which is the saturation pressure at 151.9 °C, and the allowable temperature limit set to 130 °C. The piping and fittings used in the collector loop had certified operating pressures much higher than 5 bar, as discussed in Chapter 4.4.1.5.

4.4.1.2 Collector Selection

A collector-boiler model was developed in MATLAB (see Appendix J for MATLAB code) with simplifying assumptions and carefully selected boundary conditions to simultaneously size and design the SSGS (collector array and boiler) and finalise the selection of the collector. The model allowed interchangeable efficiency parameters and aperture areas to test different collectors, change the number of collectors in parallel and series to determine the best configuration, and change the boiler size to obtain the required steam generation rate. A conservative approach was taken, with the reasoning that oversizing the collector array is better than undersizing, as the collectors may be physically covered to stop heat gain if needed.

The model simulates a single day of operation. It inputs a parabolic-type GTI distribution and a constant ambient temperature of 15°C. Three different GTI distributions were tested, each simulating an ~11-hour long day with no cloud events, as shown in Figure 13. An 11-hour day was used because the average duration of daytime for the location is ~11.5 hours, so 11 hours seemed a conservative amount. In the worst case then the system would be somewhat oversized for summertime.

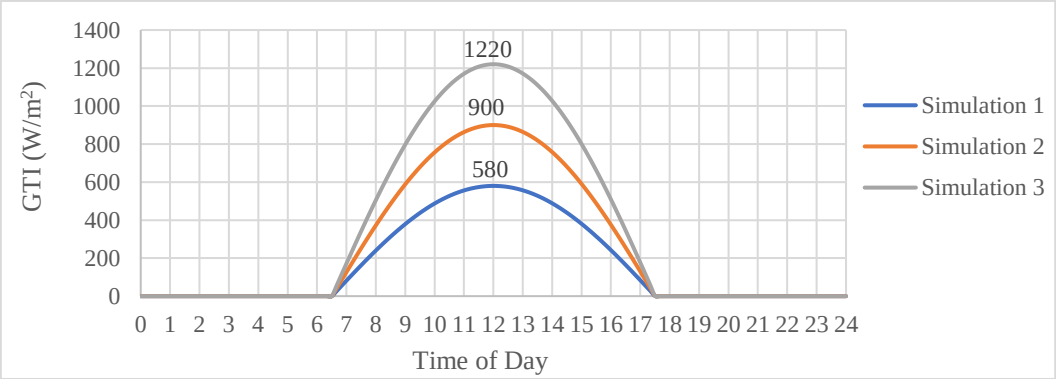

Figure 13 GTI input to collector-boiler MATLAB model

The three inputs varied in their peak values – namely, 580, 900, and 1220 W/m^2. These peaks were approximately the minimum, mean and maximum, respectively, of the monthly averages of daily peak GHI values from Brooks et al. (2015), and represent a poor, average, and good solar day. The GHI values were used to inform the GTI distributions for the model because there were no readily available GTI values.

The methodology used in these simulations does not account for intermittent cloud events, and the distributions are fictitious. However, the results were sufficient to show that the XCPC collector from Artic Solar, Inc. would outperform the ETC and CPC models considered (e.g., the Linuo-Ritter CPC 1512, CPC 1515, and CPC 1518, among others). They were also sufficient to identify the finally selected configuration of the array, as shown in Figure 12, for three largely different GTI

inputs, which was decided to be more comprehensive than designing for a single GTI value. The boiler size was also iteratively varied to determine a suitable size. Figure 14 shows the steam generation rate for each of the three simulations for the Artic Solar XCPC, showing that the system was expected to generate steam at the design rate (2.56 g/s for two cylinders) on both good and average solar days but only enough to run a single cylinder on clear-sky winter days with low peak GTI.

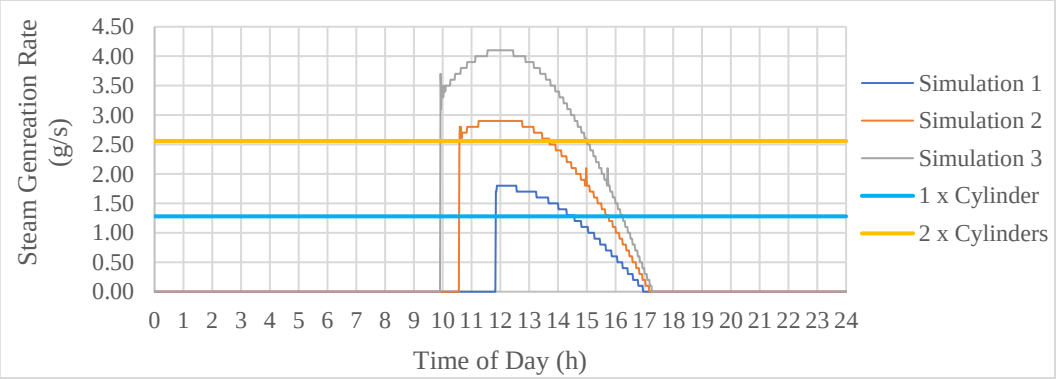

Figure 14 Collector-boiler model steam generation with XCPC collectors

4.4.1.3 The XCPC Collector

The external compound parabolic concentrator (XCPC), developed by Winston Cone Optics in partnership with the University of California Merced, and manufactured by Artic Solar, Inc., was used in this study.

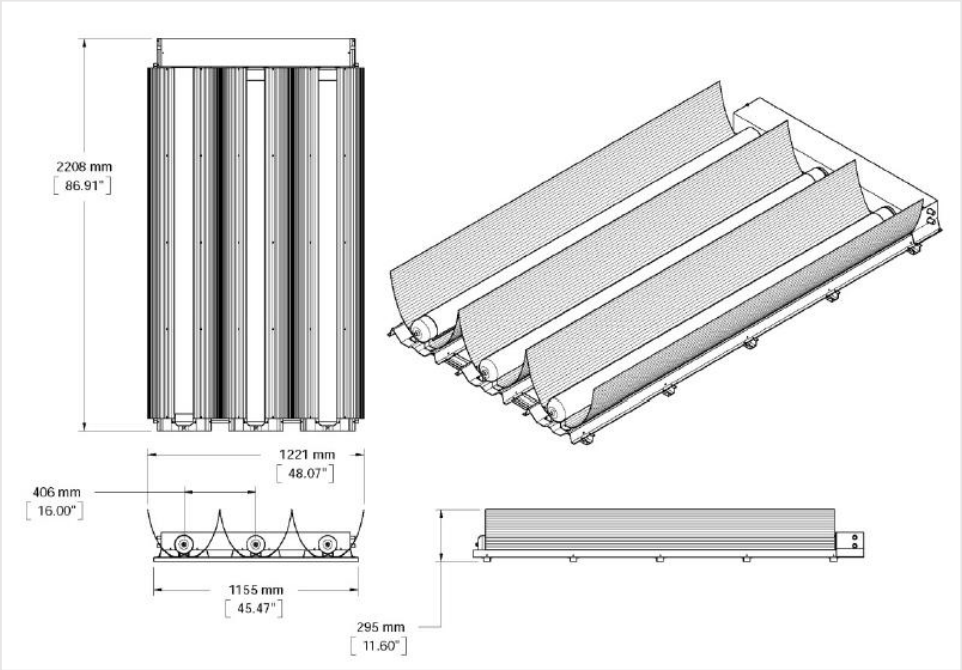

Figure 15 XCPC primary dimensions (Artic Solar, 2021)

The XCPC is a type of non-imaging collector with a geometric concentration ratio of 1.4 (Artic Solar, 2016), which means it utilises both beam and diffuse radiation (GTI) for heating.

The version of the XCPC used in this experiment, with the primary dimensions shown in Figure 15, has three metal-glass evacuated tubes, with their respective aluminium compound parabolic reflectors. The evacuated tubes each enclose a pentagon-shaped fin and U-shaped copper absorber tube that are both coated with a selective absorber coating with a solar absorptivity between 93 and 97 % and thermal emissivity between 3 and 7 % (Widyolar et al., 2021). During operation, most of the solar radiation falls on the fin, heating the fin, and heat is transferred from the fin to the copper absorber tube by conduction. Some of the radiation also falls directly on the absorber tube. Heat is then transferred from the absorber tube to the HTF by forced convection. Heat loss is reduced by the vacuum in the evacuated tube and the low thermal emissivity of the selective absorber coating.

The XCPC has the rated specifications listed in Table 6. The gross and aperture area values are from the product datasheet (Artic Solar Inc., 2021); and the efficiency curve parameters, η_0, a_1 and a_2 were provided to the author in 2021 by Winston Cone Optics. However, as presented in Appendix H, the collectors were calibrated to determine these parameters more accurately (at least for this experimental setup and operating temperature range). The “Calibrated” values are also included in Table 6. It is reasonable for the “Calibrated” heat loss coefficient values to differ from the rated values, as they were determined for a much narrower temperature range. However, the lower optical efficiency suggests a lower optical performance than specified by Winston Cone Optics. Possible reasons for this are

discussed in Appendix H. However, it is non-physical for a_2 to be negative but -0.28 was the value obtained from the polynomial fit of the data. Thus the "Calibrated" values are not to be seen as the true efficiency paramaters of the collector but were the values obtained and were useful for the given operating range for the intended purposes.

Table 6 XCPC rated specifications

Parameter	Symbol	Rated	Calibrated	Units
Gross area	A_g	2.7	-	m^2
Aperture area	A_a	2.41	-	m^2
Optical efficiency	η_0	0.57	0.53	-
First order heat loss coefficient	a_1	0.29	4.0	W/m^2K
Second order heat loss coefficient	a_2	0.003	-0.28	W/m^2K^2

The XCPC uses a double-pass configuration for the absorber tube, as shown in Figure 16, where the copper absorber tube passes through the evacuated tube twice to make a U-shape. The XCPC uses a supply header, which splits the incoming stream between the three evacuated tubes, and a return header, which collects the three streams into a single outlet stream. As such, the three absorber tubes of each collector are in parallel and not series (no serpentine effect).

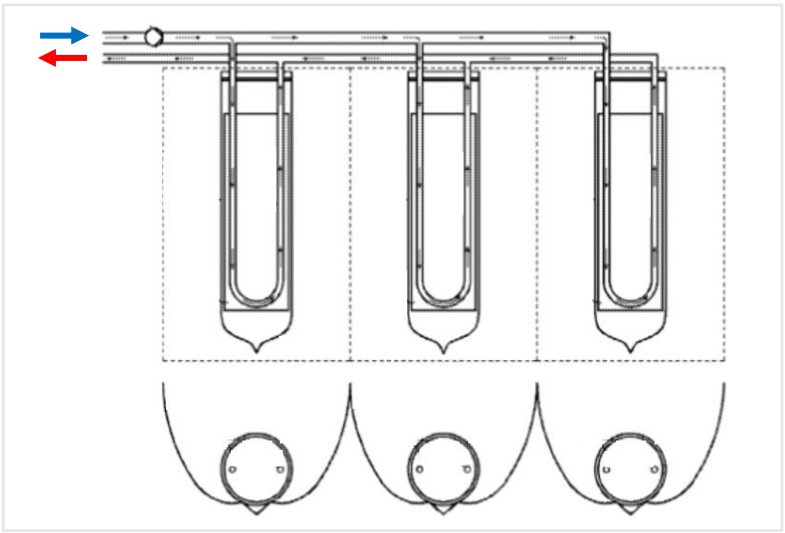

Figure 16 XCPC supply and return headers (Winston, 2016)

4.4.1.4 Layout, Tilt Angle and Circulation

As shown by the P&ID in Figure 12, the collector array uses six collectors arranged in a configuration of two rows by three columns. The stream entering the collector

array is split into three branches – A, B and C. The three streams each pass through two collectors – 1 and 2 – and then join up again to form a single outlet stream. Figure 17 shows the installed collector array before insulating the pipes.

Figure 17 Solar collector array

The ideal tilt angle for non-tracking collectors – i.e., yielding the best possible performance over an entire year without tracking – is equal to the latitude of the site ±10–15°, depending on the application (Kalogirou, 2014). The latitude of the test facility is 33.928°S, which was rounded to 30° for simplicity. Therefore, the frame was tilted at 30° to the horizontal and facing north, with the collectors mounted in an East-West orientation, as shown in Figure 17. A GRUNDFOS ALPHA SOLAR B 25-145 180 pump was selected as the circulating pump for the collector loop.

4.4.1.5 Collector Loop Safety

As per the SABS 460/85 domestic plumbing code, SABS 460 Class 1 BN copper tubing was used for the collector array, connected using SABS-approved compression fittings and soldered copper fittings. The maximum working pressure for the copper tubes, purchased from Copper Tubing Africa Ltd., are 51.3, 45.0 and 35.4 bar for the 15-, 22-, and 28-mm copper tubes, respectively. The maximum operating pressure was selected as 5.5 bar (abs), which allowed adequate safety

factors for all components. The minimum safety factor against overpressure in the piping is therefore 6.44.

Furthermore, the XCPC has been tested and certified by the Solar Rating and Certification Corporation (SRCC), according to the ISO 9806:2013 standard and the SRCC OG-100 certification program. According to its ICC-SRCC certificate, the XCPC has been pressure-tested up to 7.86 bar (abs), which gives a safety factor of 1.43 against overpressure at the selected maximum operating pressure.

The collector loop is fitted with an expansion tank as the first line of pressure relief. The 36-L Duda Energy expansion tank has an EDPM high-temperature diaphragm with a maximum allowable fluid temperature of 130°C. In addition to the expansion tank, a ZURN model P1500XL pressure relief valve is positioned on the outlet header of the collector array, as shown in Figure 12, and its venting port leads to a covered drain to avoid injury to bystanders. The relief valve was set to a venting pressure of ~7 bar (abs), as the final protection against overpressure, which gives an absolute minimum safety factor against overpressure of 1.13.

The collector loop temperature is limited by the maximum rated temperature of the expansion tank and circulating pump – namely, 130 °C. The saturation temperature at 5 bar (abs) is 151.9 °C. Therefore, a safety margin of 21.9 °C protects against boiling. Furthermore, the collector and boiler were sized to avoid exceeding 130 °C, which is made possible by the functioning of the boiler as a heat sink to the collector array; otherwise, the collector HTF could rise unobstructed to temperatures above 250 °C. Therefore, it is imperative that the boiler is filled with liquid water and the water supply to the boiler is on and operating. An easy test used to check that the boiler feedwater system was operational was to open the port below the boiler to let some water out, which should trip the float switch and activate the feedwater pump and solenoid valve. As a final resort, heat gain may be halted by covering the collector evacuated tubes.

Furthermore, according to the Thermal Insulation Association of South Africa (TIASA) (2001), all surfaces above 55 °C should be adequately insulated. Consequently, all the piping on the collector array was covered with high-temperature insulation. For fibreglass and mineral wool, pipe diameters 15 to 32 mm, and fluid temperatures 0 to 200 °C, the recommended insulation thickness is 20 mm (TIASA, 2001). All piping on the collector array was insulated with 50 mm thick mineral wool and fibreglass (this was the standard thickness available from the supplier), covered in a canvas material, and painted with Mastic Weatherproof 835 weatherproofing paint.

4.4.2 Boiler

The boiler was used for both sensible heating and vaporisation of the untreated water. A kettle-type boiler was designed as part of this project, sized using the collector-boiler model, and manufacturing was outsourced to Changzhou Raven New Energy Technology Ltd. The boiler is shown on the left in Figure 18.

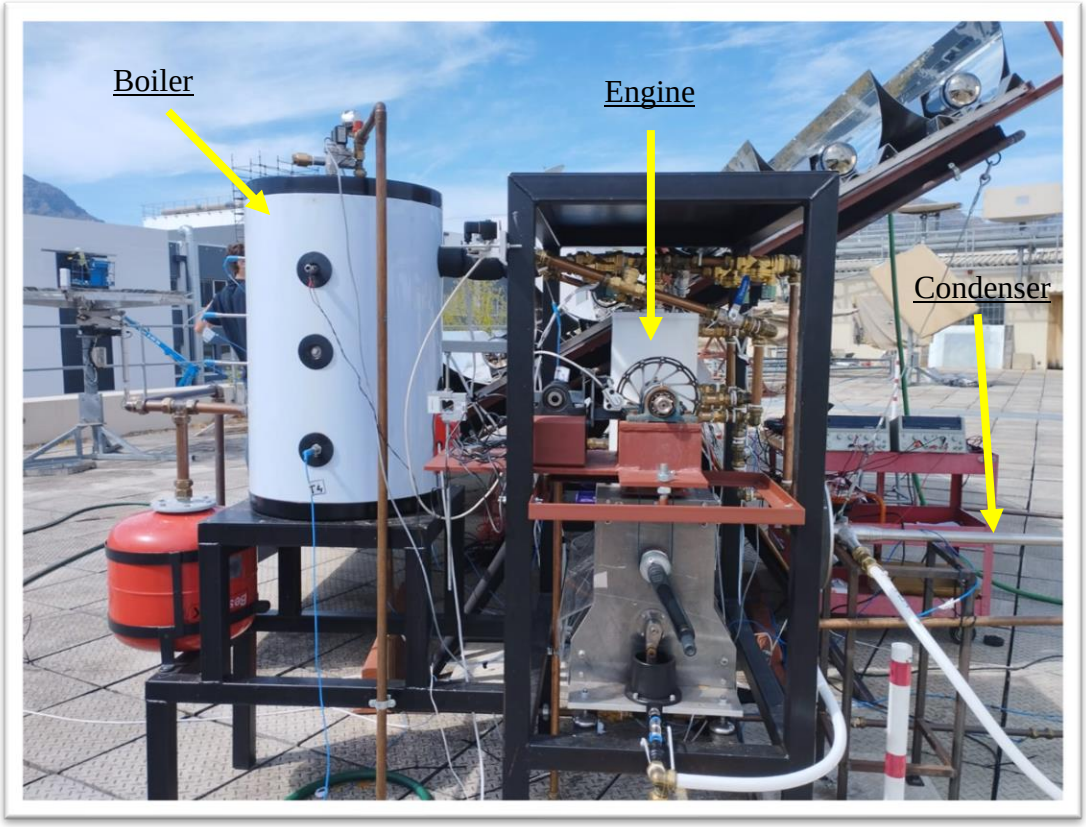

Figure 18 Photo of boiler and engine

4.4.2.1 Heating and Steam Generation

The collector array HTF, is heated in the array, and then passed through the helical coil tube, transferring heat to the pool of liquid water in the boiler vessel. This process necessitates a temperature difference, ΔT, between the collector HTF and the pool of liquid water. In addition to the solar heating, the boiler was equipped with two 3 kW auxiliary heating elements for generating steam at a constant rate.

4.4.2.2 Boiler Physical Dimensions

The physical dimensions of the boiler are given in Table 7. The vessel has a total volume of 80 L: ~59 L pool and ~21 L ullage space, although the water level varies slightly during operation. The actual pool volume is reduced slightly, primarily by the helical coil (~ 4.4 L), but also by other smaller components, such as the two electric heating elements, float switch, and thermocouples. The net pool size (~50 L) was selected iteratively using the collector-boiler model to meet the required steam production rate.

Table 7 Boiler physical dimensions

Dimension	Value (mm)
Vessel diameter	365
Vessel height	760
Vessel wall thickness	1.2
Insulation thickness	52.5
Outer shell diameter	470
Outer shell thickness	0.5
Pool height	560
Ullage space	200
Helical coil tube length	9000
Helical coil tube outer diameter	25

4.4.2.3 Boiler Components

A schematic of the boiler is shown in Figure 19, indicating the relative positioning of each of the components, as listed in Table 8. The positioning of components was limited by the minimum required spacings stipulated by the manufacturer according to standards for welded fittings. Ports that are vertically aligned had a minimum allowable spacing of 160 mm and ports could not be closer than 220 mm to either the top or bottom of the vessel.

Table 8 Boiler components with vertical positions

Label	Component Description	Vertical Position (mm)
1	Cold water supply port	160
2	Steam outlet	600
3	Vacuum breaker, pressure gauge and pressure-relief valve	760
4	Coil inlet – solar collectors return	540
5	Coil outlet – solar collectors supply	220
6	Water removal (blowdown) port	0
7	Pressure transducer, P_b	760
8	Thermocouple, $T_{p\text{-}low}$	160
9	Thermocouple, $T_{p\text{-}mid}$	340
10	Thermocouple, $T_{p\text{-}upp}$	460
11	Thermocouple, $T_{b\text{-}st}$	600
12	Horizontal float switch	560
13	3 kW Electric heating element 1	160
14	3 kW Electric heating element 2	280
15	Extra port - plugged	380
16	Extra port - plugged	280

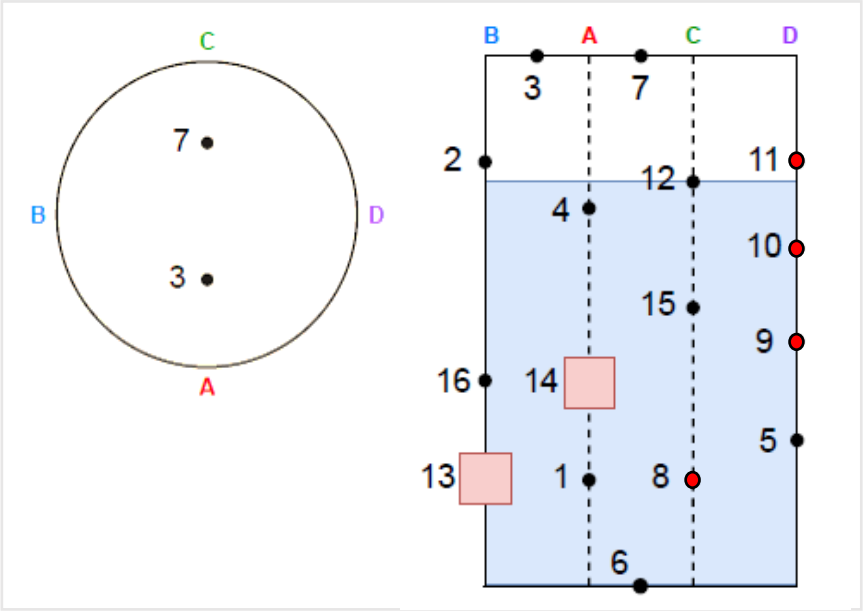

Figure 19 Boiler component positioning

The cold-water supply port (1) is placed at a low point on the boiler to minimise the effect of refilling on steam generation rate. The steam outlet (2) was situated near the top of the boiler to avoid liquid water entering the engine along with the steam. The collector HTF enters the coil at a high point (4) and exits at a low point (5). A magnesium-rod sacrificial anode is used to minimise corrosion of the metallic components – namely, the vessel wall, electrical heating elements (13 and 14), solar heating coil, float switch (12), thermocouple probes and various pipe fittings and plugs. Boiler maintenance requires regular blowdown of the boiler contents through the base port (6).

The boiler is equipped with four T-type thermocouples. These are positioned at different heights to measure the vertical variation in temperature. $T_{b\text{-}st}$ (11) measures the steam temperature in the ullage space above the pool into which steam rises during boiling; $T_{p\text{-}upp}$, $T_{p\text{-}mid}$, and $T_{p\text{-}low}$ measure the pool temperatures at positions 10, 9 and 8, respectively, to monitor the vertical variation in pool temperature. The steam pressure is measured using a pressure transducer connected at the top of the boiler (7). The other port on top of the boiler (3) is used for the vacuum breaker, manual ball valve and pressure gauge.

4.4.2.4 Untreated Water Supply

A sub-system was designed to automatically supply water to the boiler from a 500 L storage tank, which is filled manually with municipal water. The engine requires up to 2.56 g/s of steam. Therefore, if the untreated water were stored at 20°C, the boiler would need to be replenished with up to 9.2 L/hr. By regularly pumping small amounts, instability in the pool temperature profile is avoided.

Ideally an elevated tank supply would be used, to avoid the need for a pump. However, at a boiler steam pressure of 1.5 bar (abs), the back pressure would require the tank to be elevated at least 5 m, which was not practical on the SU Solar Rooftop Laboratory.

A pump is needed to overcome the elevation, as well as the major and minor losses in the piping, but primarily to overcome the back pressure exerted by the steam. Since the boiler pressure may vary between 0.8 and 1.5 bar (abs), the required pump head varies significantly.

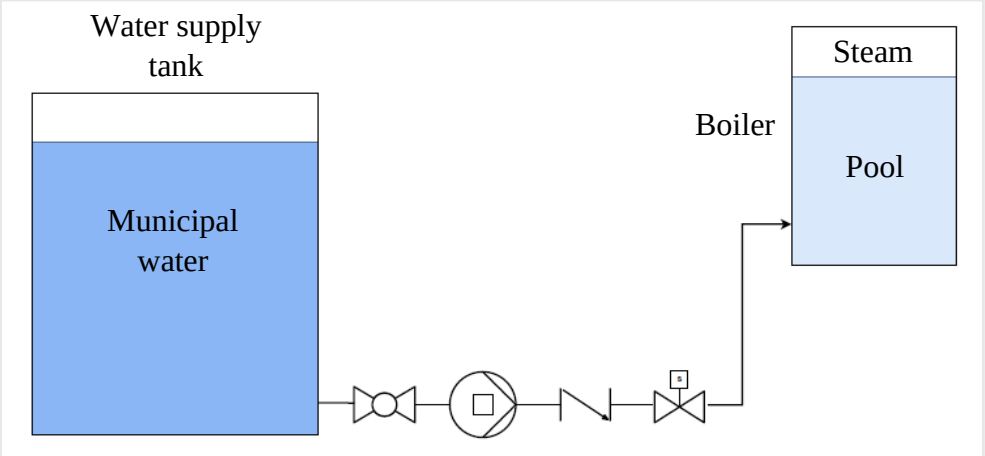

Figure 20 Boiler cold water supply

As a result, a different system curve exists for each boiler pressure. The amount of water added to the boiler in each instance needs to be controlled. As such, either a variable speed drive is required to control the supply rate and have a fixed run time, or a flowmeter is required with feedback to the controller that would then vary the pump run time. However, these are expensive solutions, and therefore not ideal according to the objectives of this project. Alternatively, positive displacement pumps typically have a steeper pump curve (head vs volume flowrate) than other pump types, such that the change in flowrate is small for large changes in required head. With this, the pump produces a flowrate within a known range, narrow enough that the pump can have a set run time and the volume of water added to the boiler is within a known range. The selected pump was a 24-V_{DC} JABSCO Mini Puppy 23620-4103 flexible-impeller pump. Figure 21 shows the pump

characteristic curve and the system curves for various boiler pressures between 0.8 and 1.5 bar (abs), which corresponds to an operating point flowrate range of 3.2 to 6.9 L/min. The system curves were determined using standard fluid mechanics friction factors to determine major and minor losses between the feedwater tank outlet and boiler inlet.

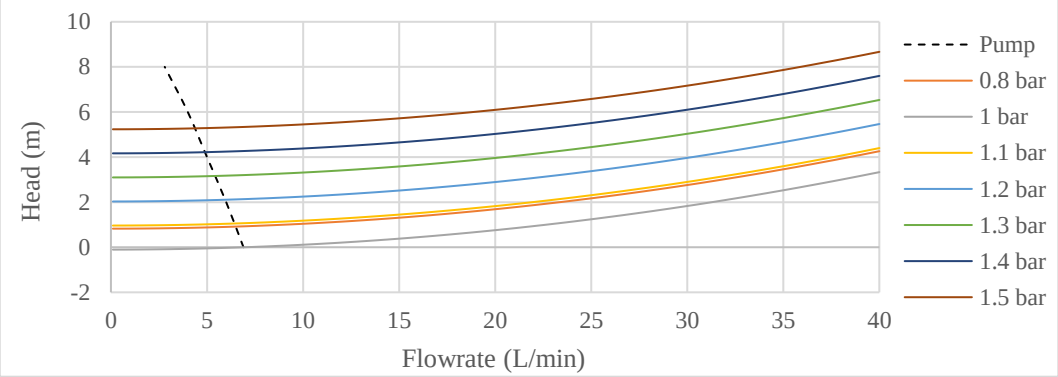

Figure 21 Boiler pump characteristic curve vs possible system curves

An RS PRO stainless steel horizontal float switch was mounted at port 12 on the boiler (Figure 19). When the float switch drops to an angle greater than 15° to the horizontal, the boiler supply pump and inlet solenoid valve are activated for a set period of 15 seconds, adding approximately 0.8 to 1.7 L to the pool volume each time, depending on the boiler pressure. Therefore, at the maximum steam flowrate of 2.56 g/s, the supply pump would run every 5 to 11 minutes (this was observed to be as expected). Therefore, since the added cold-water volume is less than 4 % of the total pool volume and is added infrequently, as well as at a low point of the boiler below the heat exchanger coil, the effect on the pool temperature, particularly near the coil, is small, while at the same time the pump can run for a reasonable time instead of having to frequently switch on and off.

The supply tank is fitted with a manual ball valve on its outlet that may be closed when maintenance procedures are performed on the components between the supply tank and boiler, so the tank does not need to be emptied. The supply pump is fitted with a check valve at its outlet because neither it nor the solenoid valve automatically prevent backflow from the boiler. The solenoid valve is a normally closed EMERSON ASCO SCE238D005.24/DC valve, used to prevent the hot water from the boiler reaching the pump, as the pump has a rated maximum allowable temperature of 70 °C, whereas the solenoid valve is rated at 85 °C.

4.4.2.5 Boiler Safety

The boiler has a rated operating pressure of 8 bar (abs) and a maximum tested pressure of 12 bar (abs), according to the manufacturer. Therefore, for a maximum

operating pressure of 1.5 bar (abs), the safety factor against bursting is 5.33 against the rated pressure. The boiler was fitted with an Altecnic 313-430 pressure relief valve, used as a safety mechanism to relieve pressure in the boiler in the event of excessive pressure build-up. The relief valve specifications are listed in Table 9.

Table 9 Boiler pressure relief valve specifications

Specification	Value	Units
Set pressure	3.0	bar
Discharge pressure	3.6	bar
Re-seating pressure	2.4	bar
Discharge flowrate	2.37	kg/s
Maximum allowable temperature	110	°C

Another potential mode of failure is collapse under a net external pressure loading if a sub-atmospheric pressure is generated inside the vessel and atmospheric pressure acts on the outside of the vessel. The most likely cause for this is quenching if cold water were added to the boiler at a flowrate high enough to cause a significant drop in boiler pool temperature to condense the steam and generate a vacuum. This could also happen when heating stops (e.g., end of the solar day), and heat is lost to the ambient environment.

A safety factor against collapse under a net external pressure was determined for the boiler by analysing it as a cylindrical vessel with an external pressure loading, as shown in Appendix I. For a specified minimum boiler pressure of 0.8 bar (abs), the safety factor against collapse under 1 atm is 2.3 assuming the worst-case scenario of the whole vessel being filled with steam at 0.8 bar (abs). However, to prevent this scenario or even lower pressures, the liquid water level in the boiler must be maintained at a safe level by regularly replenishing this liquid volume with small amounts from the supply tank.

Furthermore, a vacuum breaker mechanism, consisting of a Burkert DS6281-EV 2/2 normally open solenoid valve and a one-way valve (together used as a fail-open mechanism), was used to prevent vacuum pressures below 0.8 bar (abs). The solenoid valve is initially kept closed by the control system but is actuated by the control system to open whenever the boiler pressure drops below 0.8 bar (abs) and recloses when the pressure rises above 0.85 bar (abs). Using a different reclosing pressure prevents excessive switching of the valve. The manual ball valve may be used to vent steam or draw air into the boiler manually if required. The reason for the one-way valve is because the solenoid valve is designed for flow in one direction and does not prevent reverse flow. As such, steam would be vented (undesired) at any pressure greater than 1 atm if not for the one-way valve.

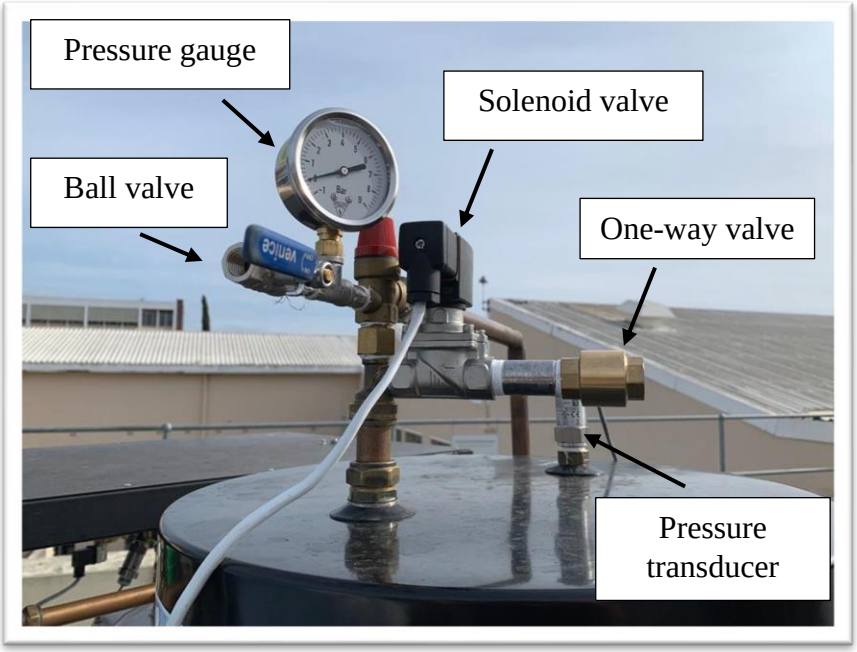

Figure 22 Vacuum and overpressure protection mechanism

4.4.3 Condenser System

4.4.3.1 Condenser Selection

The condenser used in this project was not specifically designed for this system, and there are others that might be more suitable. However, it was selected because it was the most suitable condenser available at the Stellenbosch University Mechanical and Mechatronic Engineering Department where the testing was conducted, based on cooling capacity, suitability for outdoor use and the existence of the Water Reticulation System (WRS) on the SU Solar Rooftop Laboratory (SRL) for supply and recooling of coolant water.

4.4.3.2 Condenser Specifications

The condenser used in this experiment was a simple water-cooled, counterflow, double-pipe heat exchanger with the dimensions defined in Figure 23 and listed in Table 10.

Table 10 Condenser physical dimensions

Dimension	Symbol	Value	Units
Outer tube (jacket) inner diameter	D_i	25	mm
Inner tube outer diameter	d_o	22	mm
Inner tube inner diameter	d_i	19.05	mm
Heat exchange length	L	2457	mm

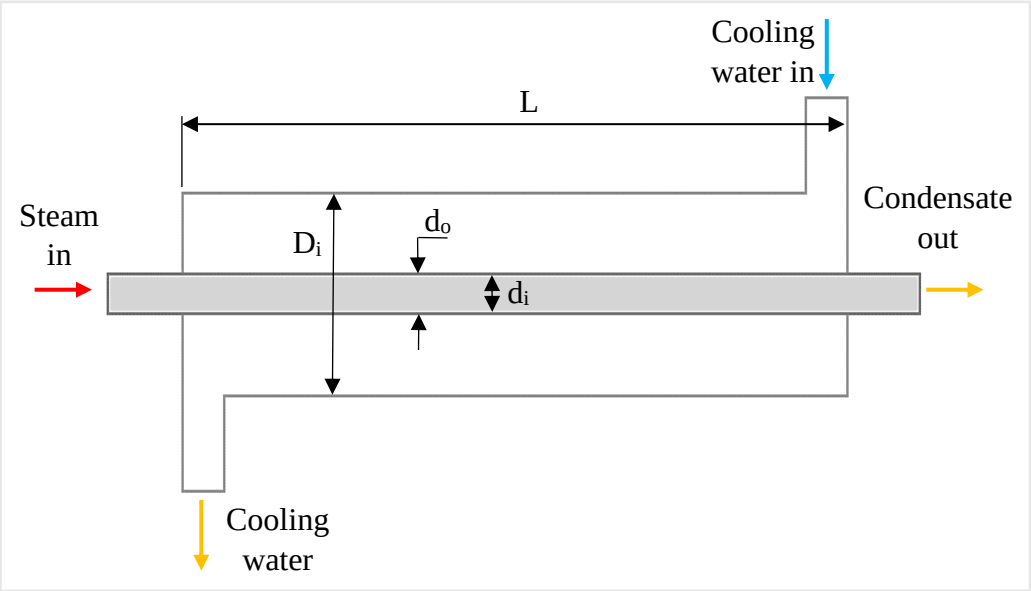

Figure 23 Condenser dimensions

4.4.3.3 Water Reticulation System

The WRS is used to provide cooling water to the condenser and then to chill the cooling water once it returns from the condenser, to continuously supply cold water at ~50 L/min. The WRS uses a Honeywell ML7420 mixing valve to cool the incoming water from the condenser by mixing it with water at room-temperature from a 1600-L storage tank.

4.4.3.4 Condenser Rating

In the initial assessment of the suitability of the condenser, a basic rating calculation was performed, using the Effectiveness-NTU method, with the inputs listed in Table 11, to determine whether the condenser could perform the required cooling. Based on the rating calculation, using the inputs in Table 11, the steam was condensed fully and subcooled to a temperature of ~35 °C. Thus, the condenser was determined to be adequate for use in this application.

Table 11 Inputs for condenser rating calculation

Input	**Value**	**Units**
Steam inlet temperature	100	°C
Cooling water inlet temperature	20	°C
Cooling water flowrate	50	L/min
Steam flowrate	4.36	L/s

4.4.3.5 Electric Vacuum Pump

At start-up, a 12-V_{DC}, 42 W Hitiland VN-C4 electric vacuum pump is used to evacuate the condenser, boiler ullage and engine piping of any entrapped air, non-condensable gases, and condensate, as well as to draw a vacuum in the condenser. Once the system is running, the vacuum in the condenser is maintained by the mechanical pump driven off the engine crankshaft. Importantly, the condenser coolant water should be circulating during this time, ensuring any hot steam or water in the engine piping has been cooled.

4.4.3.6 Condenser Safety

The steam-side inlet of the condenser exceeds the allowable temperature of 55 °C for exposed metallic surfaces, as per TIASA (2001), so the piping between the engine and condenser required insulation. Since the coolant flows in the outer jacket (and steam in the inner tube), and the coolant temperature never exceeded 55 °C, and the condensate outlet temperature remained below 50 °C, the rest of the condenser did not require any insulation.

4.4.4 Condensing Engine

A two-cylinder uniflow condensing engine is used to generate mechanical energy from low-grade steam supplied by the SSGS. The design of the engine was done by the University of Southampton (UoS), so this chapter presents the *final design* of the engine as it was built in this project, instead of a design *process*, as well as some important points on the integration of the engine with the SSGS and the condenser system. This sub-section discusses the as-built design, despite the engine not working as required. The engine performance was estimated theoretically using thermal efficiency data from literature in Chapters 6.2.3 to 6.2.5. A brief discussion of the engine defects is given in Appendix C, but the major defect was that there were leakages on the engine cylinder and cylinder jacket that prevented the requisite formation of a vacuum for the upstroke.

4.4.4.1 Major Engine Components

The major components of the condensing engine are presented in Figure 24 and listed in Table 12.

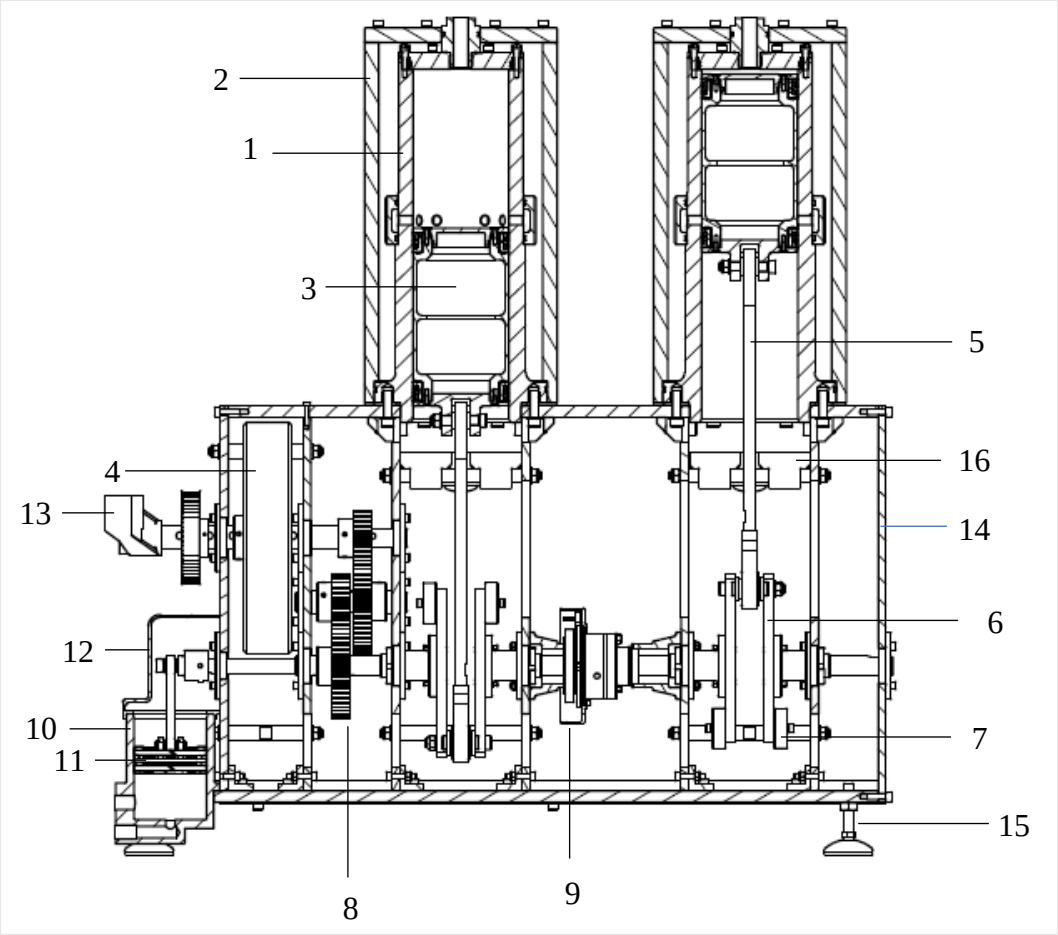

Figure 24 Engine CAD front view with partial section (CAD by UoS)

Table 12 Major condensing engine components

Label	Component Description	Label	Component Description
1	Cylinder	9	Position sensor assembly
2	Cylinder jacket	10	Vacuum pump cylinder
3	Piston	11	Vacuum pump piston
4	Flywheel	12	Vacuum pump housing
5	Conrod	13	Starter handle
6	Crank	14	Aluminium frame and bearing housings
7	Counterweight	15	Adjustable feet
8	Gear train	16	Drip tray

The characteristic cylinder dimensions are defined in Figure 25 and their values listed in Table 13. Based on these dimensions, an expansion ratio up to 1:43 is theoretically possible.

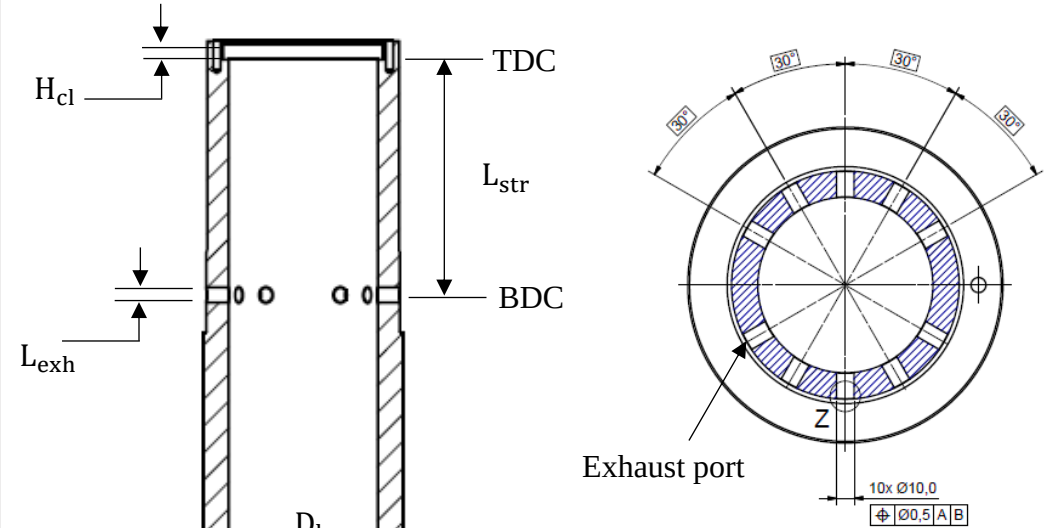

Figure 25 Engine cylinder with operating dimensions (CAD by UoS)

Table 13 Engine cylinder dimensions

Physical Dimension	**Symbol**	**Value**	**Units**
Bore diameter	D_b	100	mm
Stroke	L_{str}	160	mm
Clearance height	H_{cl}	3.7	mm
Exhaust port length	L_{exh}	10	mm
Exhaust length	-	9	mm

The cylinder was manufactured from 6082-T6 aluminium alloy and hard-coated with Nikasil. The exhaust length is shorter than the full length of the exhaust port, so that bottom dead centre (BDC) is 1 mm before the end (bottom tip) of each of the exhaust ports. Each cylinder has eight exhaust ports spaced along the circumference of the cylinder as shown Figure 25. The cylinder jacket, made from Acetal, forms a sealed cavity around the cylinder through which steam can be passed to create a jacket of steam around the cylinder. If a portion of the steam supplied by the SSGS is continuously bled off to the jacket, the steam jacket is at the same temperature as the steam entering the cylinder. If the steam is allowed to expand, increasing engine thermal efficiency, it is supplied with heat from the

jacket, maintaining its temperature, resulting in highly efficient quasi-isothermal expansion.

The piston slides inside the cylinder. On its one face it has the connecting rod (conrod) that connects it to the crank mechanism, which converts the linear motion of the piston to rotary motion in the crankshaft. On the other face of the piston is the steam, which condenses to create a sub-atmospheric pressure in the cylinder. Atmospheric pressure acts on the first face to create a net force upward. The piston has four sets of piston rings: two Slydrings and two Glydrings with O-rings (both by Trelleborg). These allow the piston to slide on the cylinder while sealing the steam on the correct side of the piston. The flywheel is used to store momentum during the piston upstroke, which is then used during the downstroke and parts of the piston cycle that require a greater linear force on the conrod to obtain the same torque. The gear train, comprised of case-hardened steel gears, is used to transfer the rotary mechanical energy from the crankshaft to the output shaft.

The auto-mechanical vacuum pump (AMVP) is used to maintain the vacuum in the condenser during engine operation. The AMVP piston is driven by the engine crankshaft using its own smaller crank mechanism. When the AMVP piston moves upward it creates a vacuum in the AMVP cylinder, drawing the condensate from the condenser. On its downstroke it discharges the condensate into the condensate collection tank. This is made possible by check valves at the inlet and outlet ports of the AMVP cylinder. The valve on the port connecting to the condenser only allows flow into the cylinder, whereas the valve connecting to the distillate collection tank only allows flow out of the cylinder, as shown in the system P&ID in Figure 12.

4.4.4.2 Engine Valve and Sensor Positioning

Figure 26 is a detailed P&ID of the condensing engine, showing the positioning of each of the valves, as well as the pressure transducers and thermocouples. The engine valve system, consisting of five solenoid valves, two manual ball valves, and two check valves, controls steam supply from the boiler to each of the cylinders and the steam jacket. SV_{bo} is the boiler outlet/engine inlet solenoid valve. SV_{C1_in} and SV_{C2_in} are the inlet solenoid valves for cylinders 1 and 2, respectively. Similarly, SV_{C1_out} and SV_{C2_out} are the outlet solenoid valves for cylinders 1 and 2, respectively. MBV_{CJ1} and MBV_{CJ2} are the manual ball valves used to control the steam supply to the cylinder jackets. The check valves ensure there is no recirculation of steam/condensate from the jacket. Pressure transducers P_{C1} and P_{C2} measure the pressure inside the cylinders (which represent P_s for the respective cylinder, as discussed in Chapter 3.3.2), since they are placed after the inlet valve and before the outlet valve for the respective cylinder, as close to the cylinder inlet as was practicably possible. Measuring after the respective inlet valve accounts for the pressure drop in the piping from the boiler and over the inlet valve. P_{eo} is used to measure the pressure at the engine outlet, which is also the inlet of the condenser.

Only the inlet and outlet temperatures for the engine were of interest in this experiment – these were measured by T_{ei} and T_{eo}, respectively.

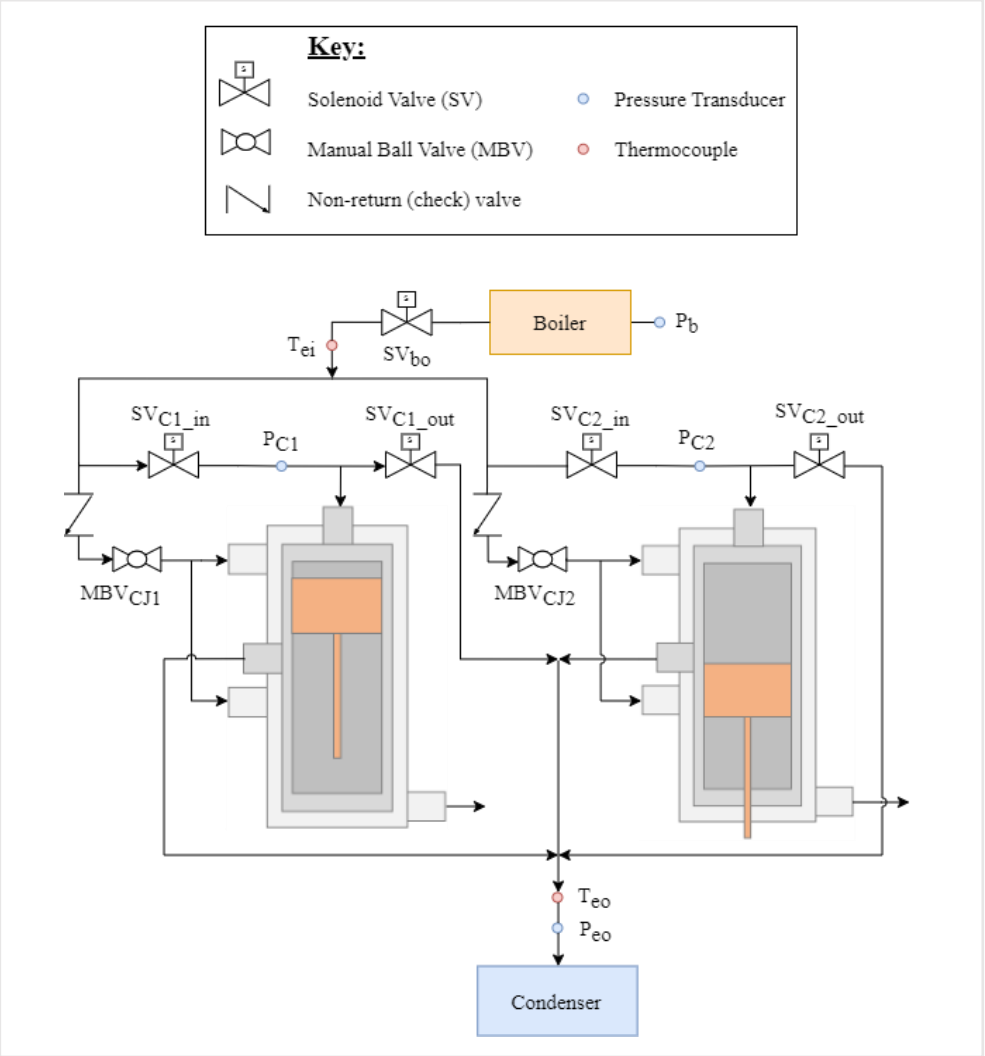

Figure 26 Engine P&ID

4.4.4.3 Engine Operation and Control

The engine was designed to operate between 60 and 120 rpm. A single revolution of the engine includes one downstroke and one upstroke for both pistons, which equates to a single revolution of the crankshaft and four revolutions of the output shaft.

During engine operation, steam is injected alternately into cylinder 1 and 2, from the top of the respective cylinder, as shown in Figure 27. During the downstroke, the outlet solenoid valve is always closed, whereas the inlet solenoid valve is open but may be closed at some point to allow for steam expansion for the rest of the

downstroke – the time of closing the inlet solenoid valve depends on the desired expansion ratio.

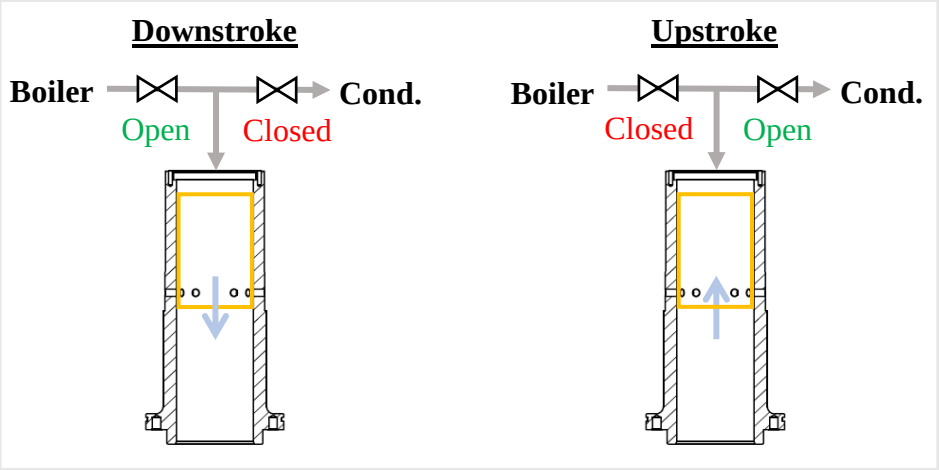

Figure 27 Inlet and outlet operation on down- and upstroke

When expansion is not used, the inlet solenoid valve remains open for the whole downstroke ($r_{exp} = 1$). For the upstroke, the outlet solenoid valve is always open and inlet solenoid valve always closed. The actuation of the valves is initiated based on readings from the engine position sensor. During engine operation, SV_{bo} remains open, because opening and closing it during operation serves no purpose since the steam supply to cylinders 1 and 2 is controlled by SV_{C1_in} and SV_{C2_in}, respectively. However, if for some reason the engine stops, SV_{bo} closes to prevent unnecessary loss of steam through the steam jackets, whose valves are manually operated and in an open position when the jacket is being used for isothermal expansion.

The net force on the piston is comprised of the force on the top face of the piston exerted by the steam, the force exerted by atmospheric pressure on the bottom face of the piston, and the frictional forces between the cylinder and the piston (transferred by the piston rings). The force balances for the downstroke and upstroke are shown in Figure 28 (note the size of the arrows is not representative of force magnitude).

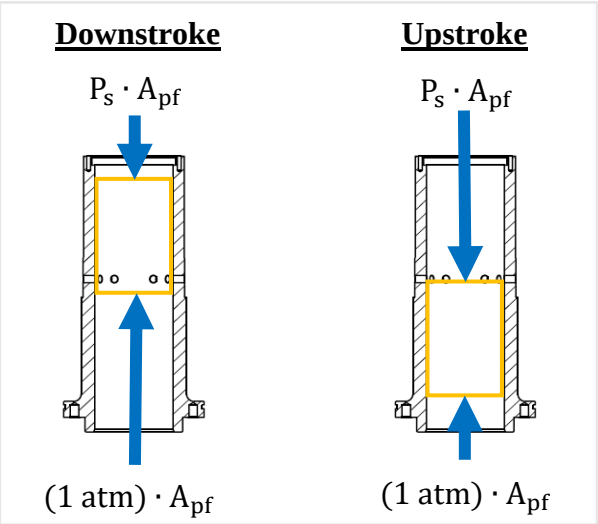

Figure 28 Basic force balance on up- and downstrokes

If steam is supplied at 1 atm or lower, then there is no net driving force on the downstroke. Since the maximum pressure for this system is 1.5 bar (abs), the maximum net force on the downstroke, excluding frictional resistance, and assuming an average pressure drop over the inlet solenoid valve of 0.4 bar, as per the valve datasheet, is 68 N (~6.9 kg) downward. On the upstroke, the force on top of the piston is exerted by the remaining steam after some steam was vented through the exhaust vents and some through the outlet solenoid valve, which is open during the upstroke. The cylinder pressure during the upstroke is at the condenser pressure (note the pressure drop over the outlet solenoid valve does not affect primary exhaustion, since the steam was vented from the exhaust ports). The required condenser pressure is the saturation pressure at 40 °C – namely 0.074 bar (abs). This gives a net force, excluding mechanical resistance, of 738 N (~75 kg) upward. Thus, it is clear from the net force acting on the respective down- and upstrokes, that the condensing engine was designed to gain most of its power on the upstroke by using the low vacuum pressure obtained in the condenser.

Furthermore, the 2-cylinder design is useful in that when cylinder 1 is on its downstroke (weaker stroke) then cylinder 2 is on its upstroke (stronger stroke). The engine is further stabilised in terms of smoothness of rotation by momentum storage in the flywheel (4 in Figure 24).

The piston position is monitored by a rotary sensor assembly. The assembly, as depicted in Figure 29, consists of two reflective object sensors and a disk on the crankshaft. The sensors are spaced 180° apart and remain stationary, while the disk rotates with the crankshaft.

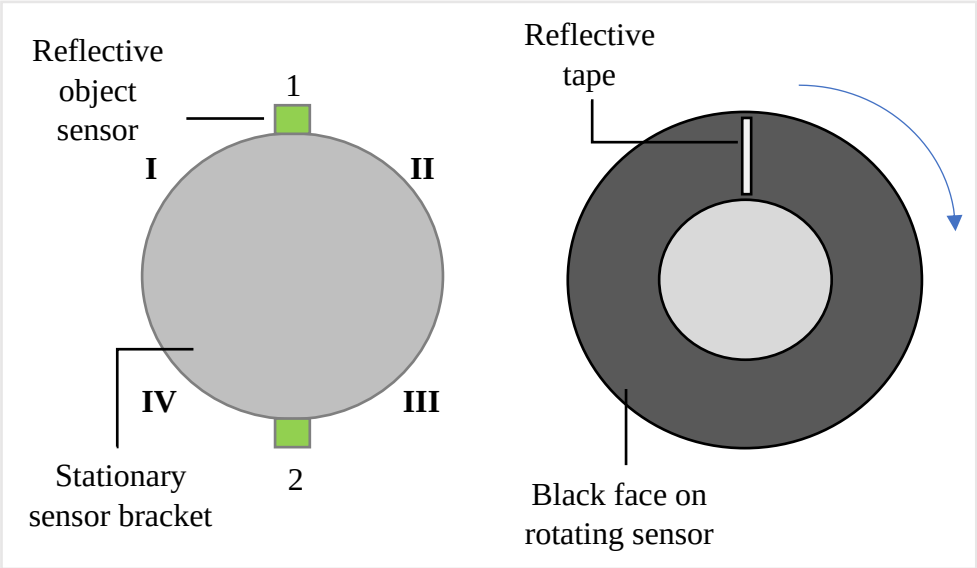

Figure 29 Piston position sensor schematic

The interior surface of the disk, facing the sensor, is painted with a smooth coat of black paint and a thin strip of highly reflective tape is adhered onto this surface. As the crankshaft rotates, the reflective tape moves circumferentially. When the tape passes one of the reflective object sensors, the voltage reading on the Arduino microcontroller analogue port drops rapidly. This drop in voltage is the indicator used by the controller to locate the reflective tape. The reflective tape was positioned so that it lines up with sensor 1 when cylinder 1 is at BDC and cylinder 2 is at top dead centre (TDC), and vice versa for sensor 2.

The engine control logic – with steam expansion – is illustrated in Figure 30. When expansion is used, the respective inlet valve is closed when the piston reaches a specified position $L_x = L_{cut-off}$, where L_x is the distance travelled from TDC of the respective piston over the time period Δt_x, and $L_{cut-off}$ is the cut-off length, which corresponds to the point on the piston downstroke where the cylinder volume corresponds to the set cut-off ratio (therefore also expansion ratio).

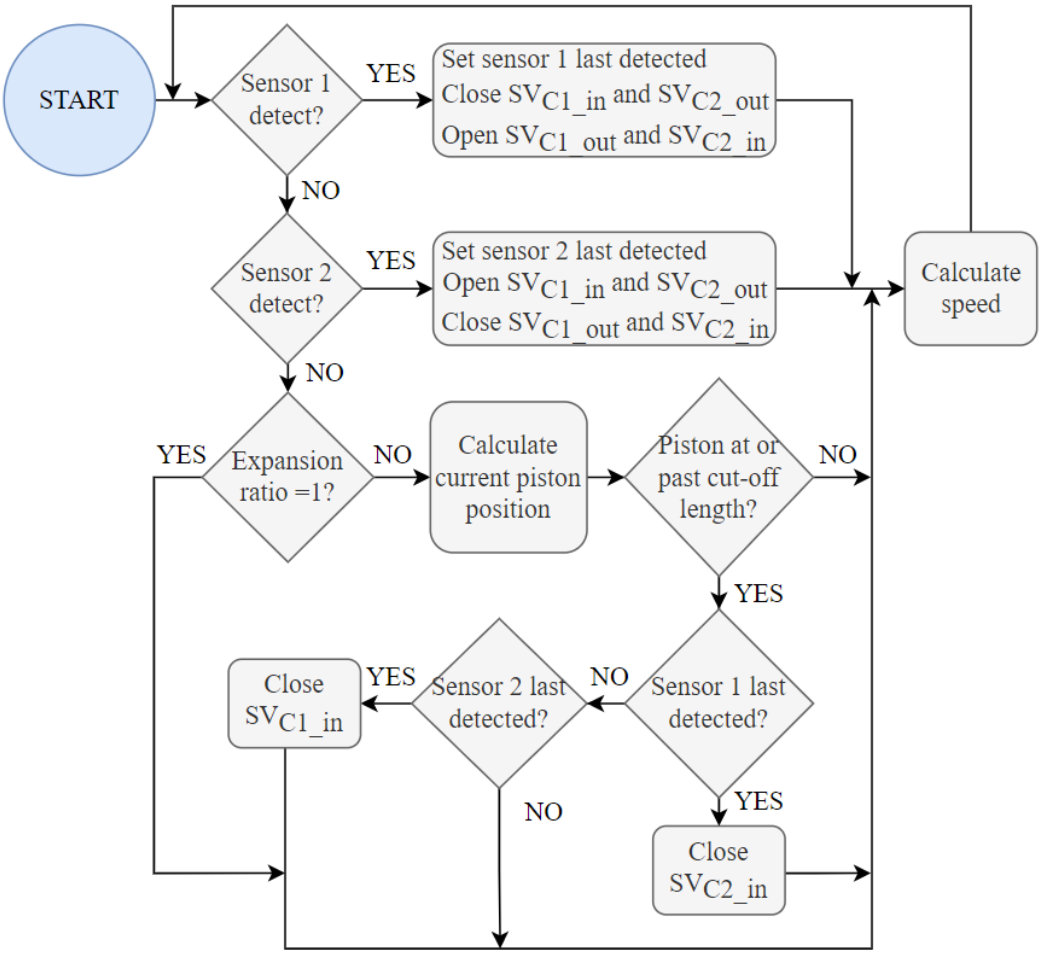

Figure 30 Engine control logic (with expansion)

A complete linear cycle of the piston (downstroke and upstroke) corresponds to a single revolution of the crankshaft. The average crankshaft speed is defined in Equation (28), where $\Delta\vartheta$ is the angular displacement (rad) and Δt is the time taken for that displacement (s). $\Delta\vartheta$ equals π rad when the reflective tape moves from sensor 1 to 2, or vice versa. The time taken between detections of the reflective tape by the successive sensors (Δt) is determined using the 16-MHz Arduino system clock. The average linear piston speed (v_p) is determined using Equation (29).

$$\omega = \frac{\Delta\vartheta}{\Delta t} \tag{28}$$

$$v_p = \frac{\omega\, L_{str}}{\pi} \tag{29}$$

The piston position (L_x) is tracked approximately using the most recent piston speed and the total time since the piston was most recently at either TDC or BDC (Δt_x)

using Equation (30). Knowing the piston position is necessary for initiating expansion at the desired point on the downstroke.

$$L_x = v_p \, \Delta t_x \tag{30}$$

4.4.5 Control and Power System

4.4.5.1 Control

The system was controlled using an Arduino Mega 2560 Rev 3 microcontroller. The Arduino board was programmed to be able to automatically control the power supply to (and thereby switching on and off) the collector loop circulating pump, the boiler supply pump, the electrical vacuum pump, and the seven solenoid valves on the boiler and engine.

The Arduino board also records voltage readings from the reflective object sensors and uses these to determine the position of the engine pistons on their respective cycles, as well as the engine rotational speed. The baud rate of the Arduino was set to 115,200 bit/s, as this was sufficient for both measurement and control with feedback.

4.4.5.2 Power

For control and measurement, various components required electrical power at their respective electrical ratings, as listed in Table 14.

Table 14 Electrical requirements of powered system components

Component	**Quantity**	**Electrical supply**
Arduino Mega 2560 Rev 3	1	9 V_{DC}, 2 A (18 W maximum draw)
Electrical heating elements on boiler	2	Single phase 230 V_{AC}, 50 Hz (3 kW)
EMERSON-ASCO SCE238D005.24/DC solenoid valve (2/2-way NC 1”)	5	24 V_{DC}, 0.17 A (4 W while holding open position)
Burkert 228387 solenoid valve (6281-EV 2/2-way NO 1/2")	1	24 V_{DC}, 0.4 A (9.5 W while holding open position with hot coil)

Table 14 (continued)

Component	**Quantity**	**Electrical supply**
Burkert 221992 solenoid valve (6281-EV 2/2-way NC 3/4")	1	24 V_{DC}, 0.4 A (9.5 W while holding open position with hot coil)
DMP 331 pressure transducers	4	24 V_{DC}, 27.5 mA (660 mW maximum draw)
GRUNDFOS ALPHA SOLAR B 25-145 180 collector loop circulating pump	1	Single phase 230 $V_{AC,}$ 50 Hz (2 – 60 W)
HITILAND VN-C4 electrical vacuum pump	1	12 V_{DC}, 3.5 A (42 W)
JABSCO Mini Puppy 23620-4103 boiler supply pump	1	24 V_{DC}, 2.5 A (60 W maximum draw)
Reflective object sensors	2	5 V_{DC}
TONGLING JQC-3FF-S-Z relay switches	9	5 V_{DC}

5 Experimental Testing

5.1 Performance Metrics

The technical performance of the system was evaluated with the metrics described in this chapter, according to the experimental procedure described in Chapter 5.2.2. Additional notes on how certain energies were determined are also included in this chapter.

5.1.1 Energy Conversion

The overall conversion from solar to electrical energy is illustrated in Figure 31 – with each conversion process having an associated efficiency or effectiveness, as indicated. The overall conversion efficiency is used to compare the system performance to other power generation systems with similar inputs (either low grade heat or solar energy), whereas the efficiency/effectiveness of the intermediate processes may be used to identify areas for potential design improvement.

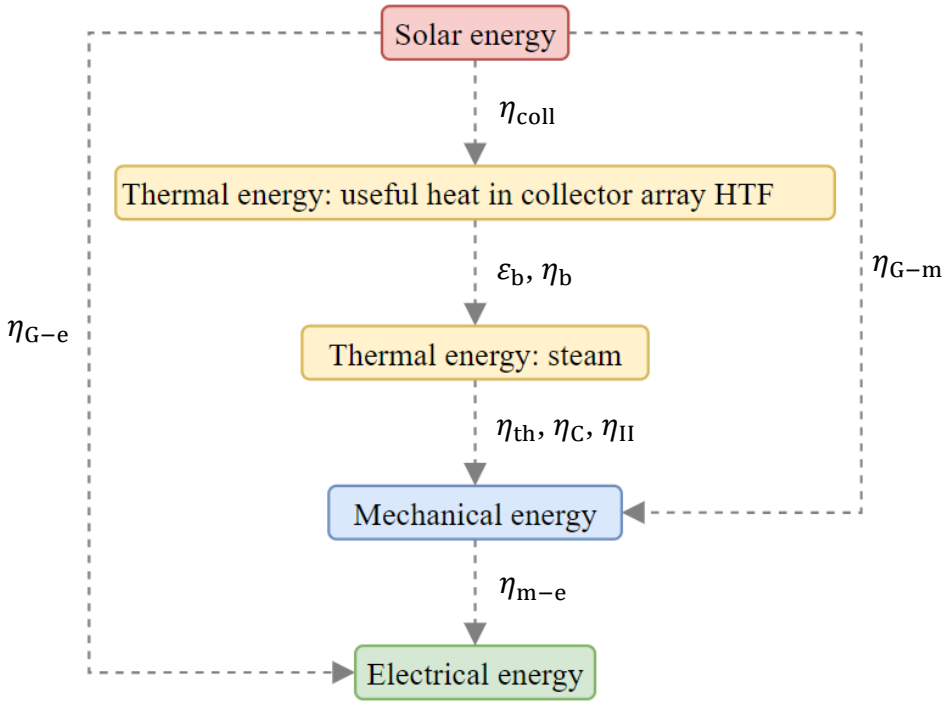

Figure 31 Energy conversion from solar radiation to electricity

5.1.1.1 Solar Radiation to Useful Heat Gain

The efficiency of solar to thermal energy conversion is described by the collector efficiency (η_{coll}), defined in Chapter 3.1.3 and Equation (10), as the ratio of useful

heat gain in the collector HTF to the solar radiation incident on the array aperture. The useful heat gain for the full collector array is the sum of the useful heat gain in each of the three branches, as per Equation (31),

$$\dot{Q}_u = \sum_{i=A}^{C} \left(\dot{m}\, c_p\, \Delta T_{io}\right)_i \tag{31}$$

where, $\dot{Q}_{u,i}$ for each branch is calculated as the enthalpy change over the two collectors in that branch, as per Equation (12). The volume flowrate was measured in branch A (see Figure 12), from which the mass flowrate could be determined. The mass flowrate in the other two branches were subsequently calculated using Equation (18). The measurement of the flowrate in branch A was required for calibration of the collector to determine η_0, a_1, and a_2, as described in Appendix H, which were required for use of Equation (18).

In the end, the mean mass flowrate values for each branch (taken as the mean from 11h00 to 15h00) were used in this analysis instead of the time-varying measurements. This was required as the use of Equation (18) yielded unrealistic mass flowrates in B and C during the early and late parts of the test period. Furthermore, the flowrate in branch A was very stable and so were the temperature measurements in all three branches, which suggested the flowrates in B and C were also stable. Therefore, this approach seemed reasonable.

5.1.1.2 Boiler Heat Gain

The boiler heat transfer effectiveness is defined in Equation (32),

$$\varepsilon_b = \frac{\dot{Q}_b}{\dot{Q}_{max}} \tag{32}$$

where the heat transfer rate ($\dot{Q}_b$) is defined in Equation (33) (heat loss from the HTF equals heat gain by the boiler pool) and the theoretical maximum boiler heat transfer rate ($\dot{Q}_{max}$) is defined in Equation (34),

$$\dot{Q}_b = C_{HTF}\,(T_{HTF,bi} - T_{HTF,bo}) \tag{33}$$

$$\dot{Q}_{max} = C_{min}\,(T_{HTF,bi} - T_{p,i}) \tag{34}$$

where, $C = c_p \dot{m}$ is the heat capacity of the respective fluid and C_{min} is determined as explained below; $c_{p,HTF}$ is the HTF specific heat capacity at the boiler bulk mean fluid temperature ($\overline{T}_{HTF,b}$ as per Equation (35)); $\dot{m}_{HTF,b}$ is the HTF mass flowrate

through the boiler; $T_{HTF,bi}$ and $T_{HTF,bo}$ are the boiler inlet and outlet HTF temperatures, respectively; and $\overline{T}_{p,i}$ is the boiler pool temperature near the coil, estimated using Equation (36).

$$\overline{T}_{HTF,b} = \frac{T_{HTF,bi} + T_{HTF,bo}}{2} \tag{35}$$

$$\overline{T}_{p,i} = \frac{T_{p,upp} + T_{p,mid}}{2} \tag{36}$$

The boiler HTF inlet temperature ($T_{HTF,bi}$) is estimated using Equation (37) as the mean of the three collector branch outlet temperatures.

$$T_{HTF,bi} = \frac{\sum_{i=A}^{C}\left(T_{HTF,co}\right)_i}{3} \tag{37}$$

During sensible heating of the boiler pool up to the saturation temperature, the maximum possible heat transfer rate is dependent on the initial fluid temperatures ($T_{HTF,bi}$ and $T_{p,i}$) and the lowest heat capacity rate between the two fluids, C_{min}. Once the pool temperature, at least surrounding the heat exchanger coil, reaches the saturation temperature at the boiler pressure, heat transfer to the pool is used towards steam generation. Then, for the pool, $C = \infty$ and therefore $C_{min} = C_{HTF}$. (Cengel and Ghajar, 2015).

Another useful metric in this experiment is the efficiency of conversion from useful heat gained in the collector array to heat gained by the boiler pool, defined in Equation (38), which indicates the amount of heat loss in the collector array piping.

$$\eta_b = \frac{\dot{Q}_b}{\dot{Q}_u} \tag{38}$$

5.1.1.3 Heat Engine Thermal-to-Mechanical Energy Efficiency

Since the engine did not operate, it was impossible to accurately determine its thermal efficiency. The analysis of potential engine performance (for the given SSGS and condenser performance) was therefore done by estimating the thermal efficiency based on actual values previously obtained in experiments by UoS in Müller et al. (2018). The thermal efficiency is related to the expansion ratio, and in this thesis variable expansion ratios were assumed to estimate the power output of the engine at each time step, calculated as the ratio of the rated steam supply rate (2.56 g/s) to the actual steam generation rate, with flowrates exceeding 2.56 g/s utilised at the minimum possible expansion ratio of r_{exp} = 1, as per Equation (39).

$$r_{exp} = \max\left[1\,;\,\frac{2.56\ g/s}{\dot{m}_{st}}\right] \tag{39}$$

Müller et al. (2018) obtained thermal efficiencies of 2 to 5.5 % corresponding to expansion ratios r_{exp} = 1 to 4, as shown in Figure 32 (which also shows the efficiency of the Hathorn and Davey engine of 3.7 % at r_{exp} = 1). In this project, a linear relationship was assumed between the thermal efficiency and expansion ratio, as illustrated by the red line overlayed on Figure 32. The linear relationship is a highly simplified approach that seeks merely to illustrate the potential range of thermal efficiencies the condensing engine could provide based on past experience by UoS with condensing engine testing. Furthermore, the data in Müller et al. (2018) had a high degree of random variation and the dataset was small, such that any regression would likely not have a high degree of accuracy in predicting engine performance. Therefore, all values dependent on the mechanical energy generation in this work are meant to represent an estimated range of potential outputs.

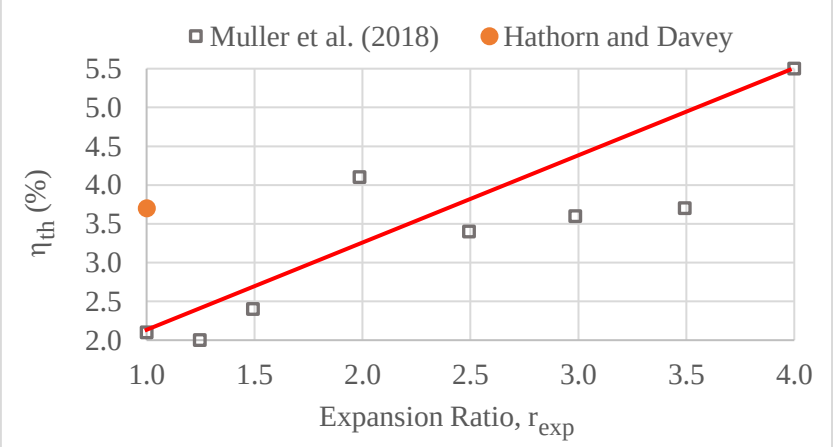

Figure 32 Efficiency vs expansion ratio, adapted from Müller et al. (2018)

The values in Figure 32 were determined at steam temperatures in the range of approximately 90 to 100 °C and for condenser outlet temperatures of 55 to 70 °C. The mean steam supply and condenser temperatures in this study were 100.0 °C and 42.4 °C, so the steam supply and exhaust pressures are better for engine operation than in Müller et al. (2018), which justifies the use of the maximum values at each of the respective expansion ratios. For instance, Müller et al. (2018) observed a range from ~1.1 to 2 % at r_{exp} = 1 in their experiments, but here 2 % was selected as the best case, which is notably lower than the Hathorn and Davey engine which operated up to 3.7 % at best for r_{exp} = 1, so it is still conservative.

The thermal efficiency (η_{th}), defined in Equation (2), evaluates the conversion of heat input in the boiler to mechanical energy output by the condensing engine. The

Second Law efficiency (η_{II}) and Carnot efficiency (η_C) are defined in Equations (1) and (3), respectively, where η_{II} is a temperature-corrected efficiency that provides additional insight by comparing the thermal efficiency to the maximum theoretical efficiency for the given temperature limits.

Furthermore, η_{th} and η_C are defined under the assumption of steady-state operation. Since the useful heat gain by the collector array is transient, the inputs to Equations (2) and (3) are transient. However, the change in temperature of the HTF is gradual over time. Similarly, the boiler pool temperature changes gradually during sensible heating and changes very slowly during boiling. Consequently, $\dot{Q}_b$ and $\dot{W}_o$ may be approximated as pseudo-steady.

5.1.1.4 Engine Mechanical Efficiency

The mechanical efficiency, defined in Equation (27), is the ratio of the shaft output power ($\dot{W}_o$) to the indicated power ($\dot{W}_{ind}$). The shaft output power is the indicated power minus the mechanical losses due to friction and other absorption of power, such as in the cranks and the gear train between the crank shaft and output shaft. In the end, the mechanical efficiency was not determined in this study due to the engine not operating and the use of an assumed thermal efficiency correlation.

5.1.1.5 Generator Mechanical-Electric Efficiency

If the engine were to be used for electricity generation, the efficiency of conversion from mechanical to electrical energy is defined in Equation (40), where $\dot{W}_e$ is the electrical power output by the generator. A mechanical to electric efficiency of 80 % – as used in Müller and Howell (2021) – was used to estimate the electrical power output of this prototype.

$$\eta_{o-e} = \frac{\dot{W}_e}{\dot{W}_o} \tag{40}$$

5.1.1.6 Overall System Efficiency

The overall efficiencies of conversion from solar to mechanical power (η_{G-m}), and solar to electrical power (η_{G-e}) are defined in Equations (41) and (42), respectively.

$$\eta_{G-m} = \frac{\dot{W}_o}{GTI \cdot A} = \eta_{coll} \times \eta_b \times \eta_{th} \tag{41}$$

$$\eta_{G-e} = \frac{\dot{W}_e}{GTI \cdot A} = \eta_{G-m} \times \eta_{m-e} \tag{42}$$

5.1.2 Distillate Production

Specific Energy Consumption (SEC) is a widely used metric for evaluating the energy efficiency of desalination/water purification, such as in Kalogirou (2014) and various other sources, and is the amount of energy used to produce a unit volume of clean water (distilled water in this case), as in Equation (43), where GTI^* is the solar irradiation and V_{dist} is the volume of distillate produced (corresponding to the irradiation period). The SEC may be used to compare the performance of this prototype to other desalination systems.

$$SEC = \frac{GTI^*}{V_{dist}} \tag{43}$$

5.2 Testing

The measurement equipment, experimental procedure, and data processing used to determine the system performance metrics are described here. Testing occurred on the SU SRL, which has a geographic location 33.928425°S and 18.864944°E, and elevation of 119 m. An aerial view of the facility is presented in Appendix A.

5.2.1 Measurement Equipment

Table 15 is a comprehensive list of the measurement equipment used in these experiments with information on the types of measurements taken, equipment accuracy and calibration. For reference, see the P&ID in Figure 12. All the measurements were recorded on an Agilent 34972A data acquisition device (DAQ), using Agilent Benchlink Data Logger 3 software; except for the pressure transducer and pyranometer readings, which were recorded on a National Instruments NI-9219 DAQ and LabVIEW software, and the manual reading of the collector array pressure gauge.

Table 15 Measurement equipment summary

Equipment	Measurement	Equipment Accuracy and Measurement Resolution	Calibration
T-type thermocouples (x15)	Temperature in various parts of system	For the temperatures measured and the specific thermocouples, the error < 1 °C. Data logged every 10 seconds.	See Appendix C
DMP 331 low-pressure industrial pressure	Absolute pressure in boiler, engine,	P_b, P_{C1}, and P_{C2} had the same full-scale (FS) accuracy of 0.35 % over the range 0 to 3 bar (abs);	See Appendix E

transducers (x4)	and condenser piping.	P_{eo} had a FS accuracy of 0.1 % over the same range. Data logged every 10 seconds.	
Winsmeter TH7 volume flowmeter (x1)	Volume flowrate in branch A of collector loop	Error < 0.6 %. Data logged every 10 seconds.	See Appendix G
KIPP and ZONEN CMP6 pyranometer (x1)	GTI on actual test apparatus	Daily uncertainty < 5 %. Data logged as 10-second averages of 10 readings spaced 1 second apart.	See Appendix F
Laboratory measuring beaker	Distillate volume produced over a known period	Resolution of beaker was 5 mL. Manual reading taken very 10 to 15 min.	N/A

5.2.2 Experimental Procedure

Start-up:

1. The solar collectors were cleaned and allowed to dry before testing to ensure a maximum cleanliness factor.
2. The 1600-L storage tank of the WRS was filled with ambient-temperature water. This water was used to recool the condenser coolant water after it has been heated by the condensing steam.
3. The WRS circulation was started, supplying cooling water to the condenser.
4. As a safety precaution, the collector loop was emptied after testing. As such, for each test the collector array needed to be filled. The loop was filled at 5 to 6 bar (abs) from the municipal supply. Some of the water would be vented from the highest point of the loop until the pressure dropped to between 4 and 4.5 bar (abs). The pump would then be started and the pressure at the circulating pump outlet would rise. Water would then be vented again from the highest point of the loop until the pressure at the pump outlet reached between 5 and 5.5 bar (abs), which was the desired operating pressure. The pressure was read from the pressure gauge placed approximately 1 m (~35 pipe diameters) downstream from the pump outlet (see Figure 12 for system P&ID) to allow for hydrodynamic redevelopment of the flow, so that the readings were representative of the actual pressure. The filling/venting procedure was made easier by using a three-way valve system on the hose pipe from the municipal supply used for filling the array. The three-way valve was placed near the pressure gauge so the operator could monitor the pressure while venting to obtain the desired pressure with ease.
5. The boiler was emptied and refilled to ensure the starting temperatures were similar for each of the tests, and to test the working of the automatic untreated

(raw) feedwater supply system. The boiler was also opened to atmosphere via the manual ball valve shown in Figure 22, which set the initial pressure to 1 atm and ensured the pressure and presence of air was similar at the start of each of the tests. However, since opening the boiler to atmosphere allowed air to enter the boiler and this would impede on the correct operation of the engine, it was necessary to remove this air. The method used to achieve this was to allow the pressure in the boiler to rise and then to keep the manual ball valve (see Figure 22) open to vent steam, ensuring the pressure did not drop to 1 atm, preventing air ingress into the boiler. The vent was then closed during operation.

6. If the engine had been incorporated, the electric vacuum pump would have been started to remove all air and non-condensable gases, as well as condensate, in the condenser, engine, and boiler ullage, and to draw a vacuum in the condenser before any steam is supplied to the engine. The engine start-up would then require manual turning of the engine using the starter handle, which would initiate the relevant opening and closing of solenoid valves based on the piston position, and start the AMVP, which would then be responsible for maintaining the vacuum in the condenser. Since the engine did not operate, the AMVP could not be used, and since the electric vacuum pump was not designed to remove steam at the rate generated by the SSGS (only meant to be used once-off at start-up), the only option would have been to use gravity to drain the condensate from the condenser (condenser and piping were installed at a slight inclination) with the condenser outlet open to atmosphere leading into the condensate collection tank. As such, the low vacuum pressures that would be attainable during engine operation had to be inferred as the saturation pressure at the condenser subcooled temperature.

During Operation:

Once the system was up and running, very little intervention was required other than some manual measurements, because the control system was fully automated along with most of the measurements.

1. Once the collector array circulating pump was started, it ran for the entire duration of the test, producing a very stable pressure and flowrate. The collector array pressure was recorded manually every 10 to 15 minutes.
2. The boiler pool rose in temperature from an initial (near ambient) temperature up to the saturation temperature at atmospheric pressure (~100 °C). Therefore, once the pool and steam temperatures reached 100 °C, wet steam was visibly observed exiting via the open manual ball valve on top of the boiler. The valve would then be closed.
3. Shortly after closing the manual ball valve, distillate would start to drip into the distillate collection tank (covered to prevent evaporation). Every 10 to 15 minutes, the distillate would be transferred into a bucket and the volume of distillate measured using several 500 mL laboratory measuring beakers. This would then be used to determine the average distillate production rate throughout the test period.

4. At the end of the test period (just after 17h00), the distillate production rate would decrease significantly, at which point the test would be stopped. The various data were saved from the DAQ software along with the Excel spreadsheet where manual readings were recorded. The power supply to the system would then be switched off and the collector array emptied.

5.2.3 Data Processing

The collected data, with measurement frequencies listed in Table 15, were converted to 10-minute averages and hourly averages for the analysis presented in Chapter 6. The equipment measurement accuracies listed in Table 15 indicate the systematic uncertainty introduced into the data by the instrumentation. The error values stated in Table 15 account for the entire relevant range of measurement so in some cases are conservative.

The standard deviation for each data point was calculated to quantify the random uncertainty brought about by fluctuations within the data samples used to determine the 10-minute averages. In most cases, the associated standard deviation was determined from the same 10-minute sample of data used to determine the 10-minute average data point. However, this is not suitable when the sample is taken on a gradient. For instance, in Figure 33, during sensible heating up to 10h40 the boiler pool temperature changes at ~1°C/min, so the standard deviation in a 10-minute sample is ~3.03°C, which at 40°C, for instance, suggests 7.6 % standard deviation, which is not reflective of random fluctuation in the data but just the actual change in value over time. As such, the standard deviation in these cases was taken for a 1-minute sample. However, after 10h40 the standard deviation is obtained from the full 10-minute sample. The maximum and mean standard deviations are given in Appendix B for all data relevant to Chapter 6.

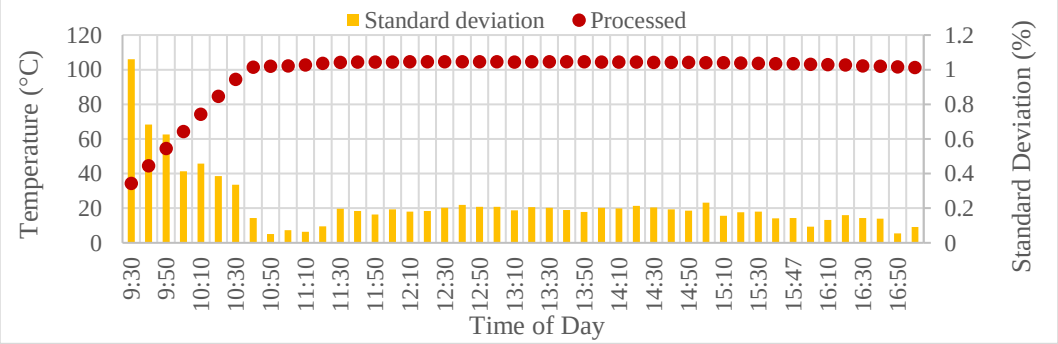

Figure 33 Processed temperature data

In some cases, the results in Chapter 6 are presented as hourly averages, such as the distillate production rate and GTI for SEC calculation. In these cases, the 10-minute average values were used to determine the hourly averages.

6 Results and Analysis

Results from three 8-hour performance tests conducted on 14, 16 and 18 February 2023 are presented in this chapter to showcase the system performance in good solar conditions. Numerous other tests were conducted, although these three days were selected for having the most complete and useful data for the following performance analysis. All three of the selected days are considered good solar days during the global-south summer. February 14th and 16th had finite periods of cloud cover, whereas 18 February had clear skies for the entire test period. The analysis includes evaluation of each of the energy conversion processes and their respective efficiencies, including the overall average conversion efficiency from solar energy to both mechanical and electric energy; evaluation of the distillate production rate and associated specific energy consumption; and estimation of the annual energy and clean water generation capabilities of this technology per unit collector aperture area. The cloudy periods were excluded from the results unless otherwise stated, as the effects observed were arbitrary in the context of this analysis given the final conclusions.

6.1 Test Day Conditions

Figure 34 presents the directly measured GTI distribution for each of the tests. The section highlighted in green represents the ramp-up period during which the boiler water is heated to the saturation temperature, and the yellow section represents the in-operation period when the boiler was generating steam.

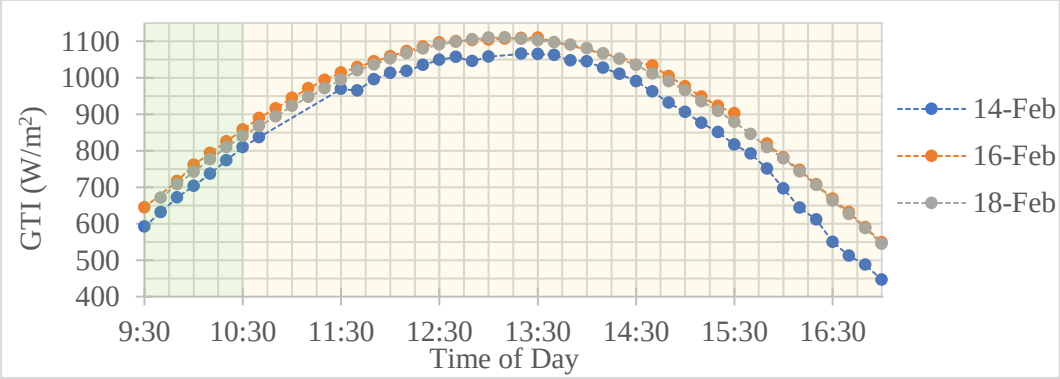

Figure 34 GTI variation with time during test days

The peak GTI on 14, 16 and 18 February was 1.07, 1.11 and 1.11 kW/m^2 and the total GTI in irradiation terms was 5.85, 5.77, and 6.92 kWh$_{solar}$/m^2 (for the test period), respectively. The excluded cloudy periods occurred from approximately 10h50 to 11h25 on 14 February and 13h40 to 14h40 on 16 February. A distinct

haziness was evident on 14 February, even though it was a sunny day, which is the suspected cause for the lower GTI throughout the day compared to 16 and 18 February.

The ambient air temperature, shown in Figure 35, varied the most across the three days of any of the measured variables. Additionally, the wind speed and direction are plotted as hourly averages in Appendix A, but these were not included in the performance analysis because the wind speeds were not unusually high on any of the days.

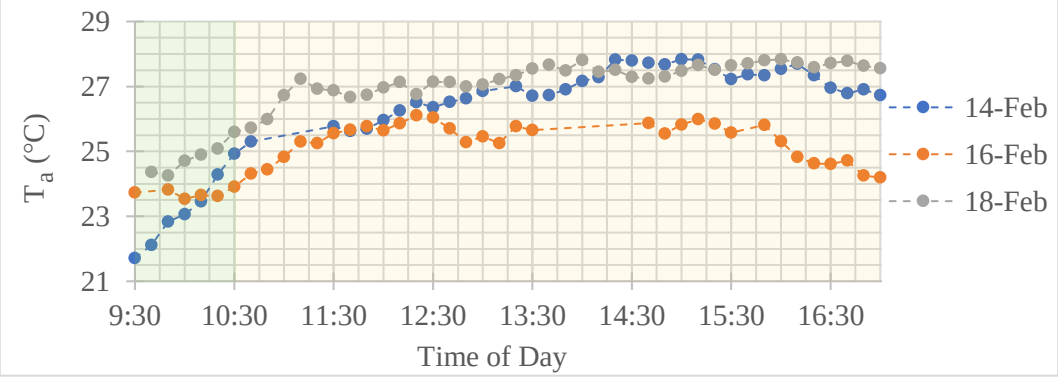

Figure 35 Ambient air temperature variation with time during test days

6.2 Energy Conversion

6.2.1 Solar Radiation to Useful Heat Gain

Figure 36 presents the total useful heat gain by the collector array HTF, determined using Equation (31), as well as the theoretical useful heat gain calculated using Equation (11) with the measured GTI, temperatures, and the rated values for the collector efficiency parameters (η_0, a_1, and a_2) listed in Table 6.

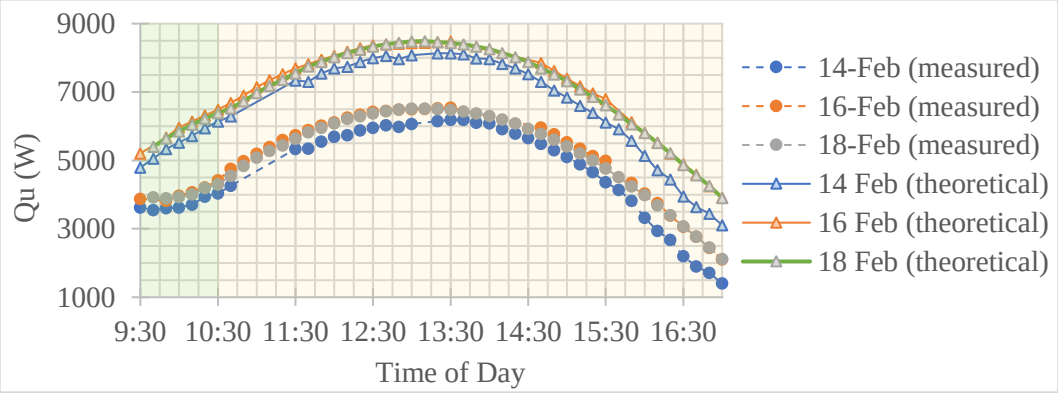

Figure 36 Useful heat gain variation with time during test days

As with the GTI in Figure 34, the useful heat gain on 16 and 18 February followed each other closely while 14 February was lower in magnitude. The peak heat gain for 14, 16 and 18 February was 6.18, 6.55 and 6.52 kW, and total heat gain for each of the tests was 2.19, 2.20, and 2.65 kWh_{th}/m^2, respectively. The total useful heat gain was 71.4, 72.7, and 72.9 % of the theoretical useful heat gain for 14, 16 and 18 February, respectively, which prevented the system from performing to the full potential predicted in the collector-boiler model.

Figure 37 shows the solar-to-thermal efficiencies, calculated using Equation (10), which were lower than the theoretical efficiencies determined with the rated coefficients. The mean efficiency was 36.6, 37.5, and 37.8 %; and the peak efficiency (only considering 10h30 onward, during boiling) was 42.3, 41.6, and 40.6 %, for each of the tests respectively. The suspected cause for the lower-than-rated efficiency is addressed in the collector calibration presented in Appendix H, but in brief: the heat gain is reduced by suspected defects in the collectors – particularly related to the absorber tube and fin, with the tube sagging near the centre of the span and losing some of its contact with the fin. Furthermore, the rated collector efficiency parameters were obtained under ideal conditions (G_{beam} = 850 W/m^2, $G_{diffuse}$ = 150 W/m^2), but the GTI is much lower in quality than this near the start and end of the day – i.e., the ratio of diffuse to beam irradiance is larger due to the large incident angle, which means lower levels of concentration and lower levels of irradiance on the receiver tube). The convection heat loss effect of wind is not believed to be a possible cause for lower efficiency.

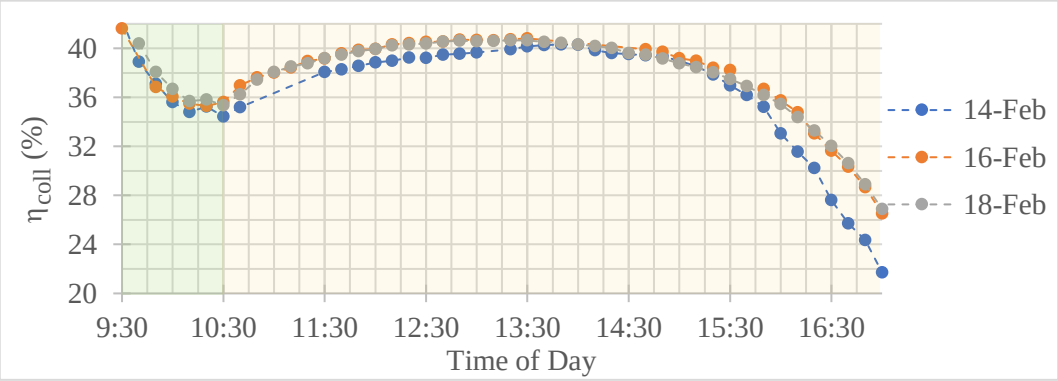

Figure 37 Solar-to-thermal efficiency variation with time during test days

Collector efficiency is typically higher at lower collector temperatures relative to ambient due to lower heat loss; and since lower GTI would yield lower temperatures, one would expect a slightly higher efficiency on 14 February. However, haziness reduces the ratio of beam to diffuse radiation, which reduces the amount of irradiance concentrated onto the receiver – lower quality GTI. As such, the efficiency is lower for lower quality GTI, which is the likely cause of lower efficiency on 14 February. Furthermore, the variation in ambient temperature across

the three days appear to be negligible, seeing as the efficiencies observed on 16 and 18 February are almost identical despite the lower ambient temperature throughout the day on 16 February.

The maximum collector array HTF temperatures are shown in Table 16. There is an apparent correlation between the maximum GTI and maximum temperature. However, the values are within 1.3 % of each other for all three branches on each of the days, which shows good repeatability in the tests and consistency in system performance.

Table 16 Maximum collector HTF temperatures

Day	$T_{HTF,co-A}$ (°C)	$T_{HTF,co-B}$ (°C)	$T_{HTF,co-C}$ (°C)
14 Feb 2023	113.4	114.8	114.7
16 Feb 2023	115.0	116.1	115.9
18 Feb 2023	115.5	116.6	116.8

The mean mass flowrates, determined between 11h00 and 15h00, are listed in Table 17. The standard deviation across the three branches for any given day was less than 8 %, showing that while there was a slight flow imbalance in the solar field, it was within reasonable limits; and for any given branch across the three days the standard deviation was found to be less than 4.3 %, showing good repeatability in the three tests.

Table 17 Mean mass flowrates for branches A, B and C

Day	$\dot{m}_A$ (kg/s)	$\dot{m}_B$ (kg/s)	$\dot{m}_C$ (kg/s)
14 Feb 2023	0.0603	0.0521	0.0534
16 Feb 2023	0.0561	0.0509	0.0537
18 Feb 2023	0.0560	0.0498	0.0498

6.2.2 Boiler Heat Gain

The rate of heat gain by the boiler, determined using Equation (33), is shown in Figure 38. The first 60 to 70 minutes comprised sensible heating of the liquid pool up to the saturation temperature, followed by phase change to steam for the rest of the test period. The heat transfer rate was dependent on the temperature difference between the HTF and boiler pool – particularly near the helical coil tube – and the heat exchanger effectiveness. The peak boiler heat gain was 5.94, 6.25, and 6.39 kW; and the total daily heat gain was 2.04, 1.93, and 2.46 kWh_{th}/m^2 for 14, 16, and 18 February, respectively.

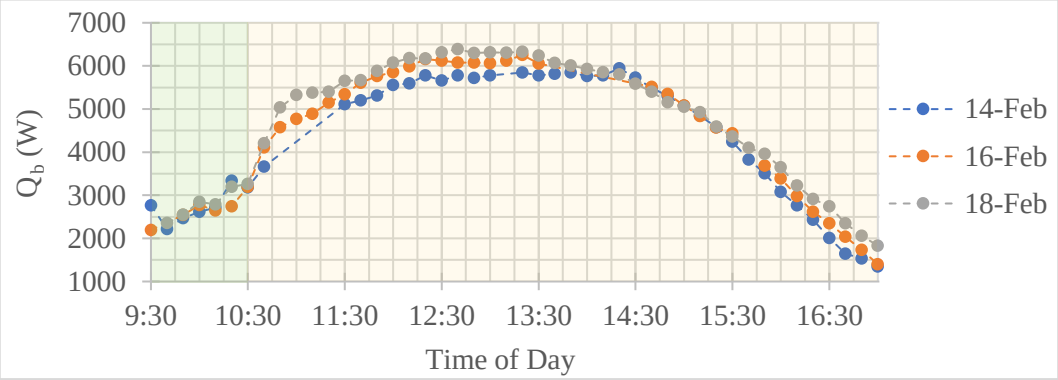

Figure 38 Boiler heat gain variation with time during test days

The SSGS displayed a high efficiency, calculated using Equation (38), in transferring the useful heat gained by the collector HTF to heat gain in the boiler pool, particularly during boiling, as shown in Figure 39.

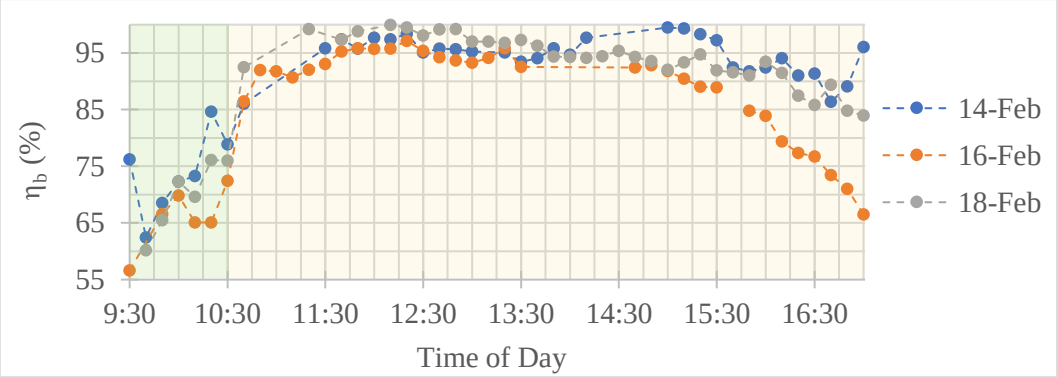

Figure 39 Collector to boiler thermal transfer efficiency variation with time during test days

The efficiency increased gradually from the start of the test until boiling commenced and then remained mostly above 90 %, although it then decreased again towards the end of the test period as the heat exchanger effectiveness – determined using Equation (32) – decreased, as presented in Figure 40. The mean collector-to-boiler heat transfer efficiency was 91.7, 85.2, and 91.5 %; and the mean heat exchanger effectiveness during boiling (10h40 onward) was 79.8, 77.0, and 81.5 % for 14, 16, and 18 February, respectively.

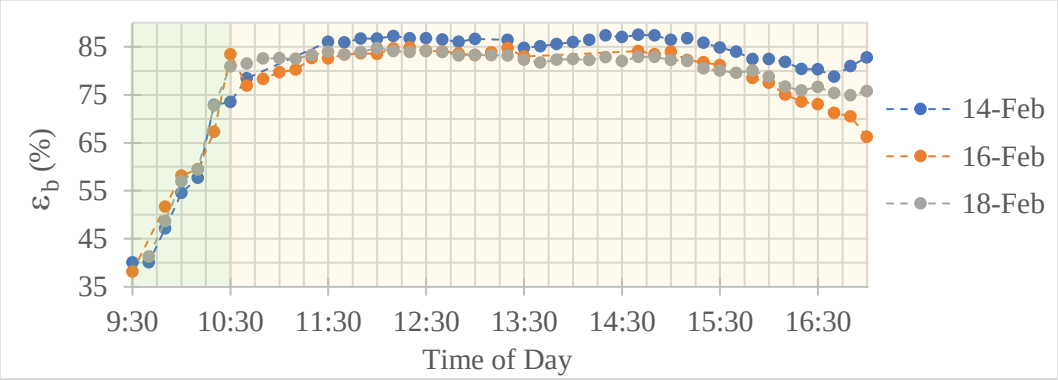

Figure 40 Boiler effectiveness variation with time during test days

As shown in Figure 41, the steam generation rate was close to the required rate of 2.56 g/s (full load: no expansion and two cylinders in operation) during the middle part of the day for all three tests (2-3 hours), reaching a maximum of 2.65, 2.79, and 2.85 g/s; with a mean value of 2.10, 2.10, and 2.25 g/s on 14, 16, and 18 February, respectively.

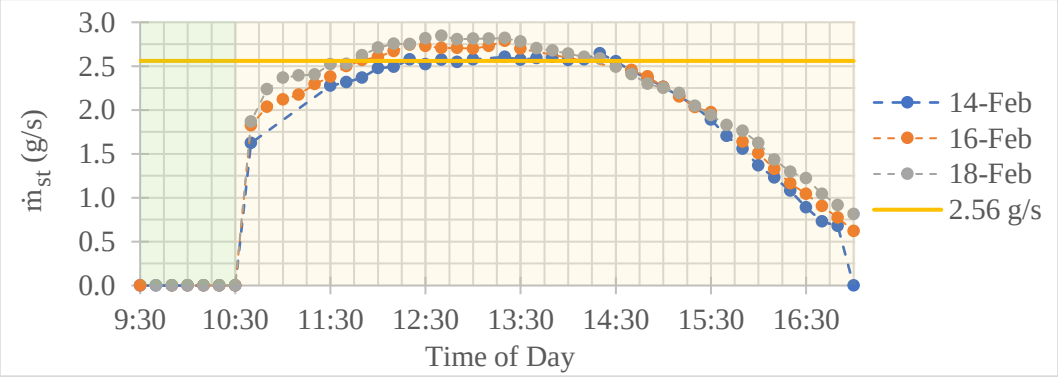

Figure 41 Mass rate of steam production variation with time during test days

Seeing as the tests were conducted on good solar days, the SSGS requires upsizing of the solar field and boiler to meet the required steam generation rate during winter and to increase the duration of full-load generation during summer. Upscaling the SSGS for these purposes would motivate for a thermal energy storage system to store excess thermal energy during peak solar periods. This would also enable constant rate generation if desired and potentially assist with reducing the ramp up period and the effect of intermittent clouds.

For the case where variable mechanical power is allowed the system could, depending on the rate of steam supply to the engine, use variable expansion ratios or adapt the number of cylinders being supplied at any given time, both of which

require careful valve control. As discussed later in this chapter, the power output was estimated assuming variable expansion ratios between 1 and 4.

Furthermore, the SSGS generated the steam within the required pressure limits – 0.8 to 1.5 bar (abs) – as shown in Figure 42, which is the pressure measured at the cylinder inlet (after the inlet solenoid valve losses).

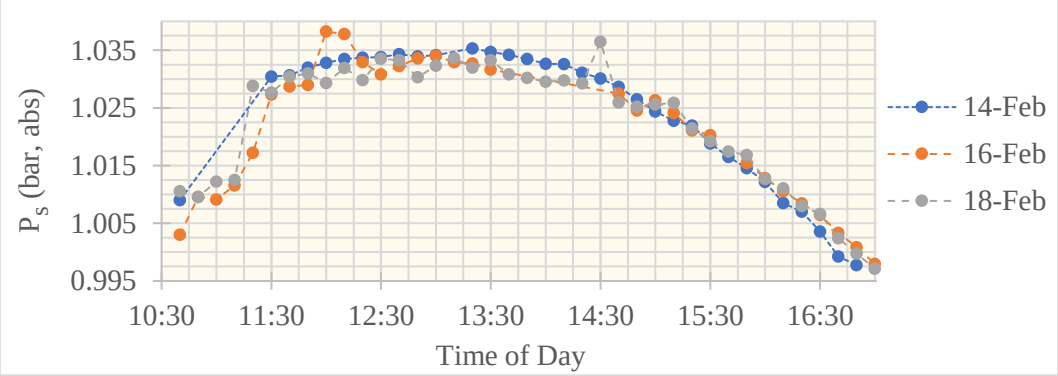

Figure 42 Cylinder inlet pressure variation with time during test days

The maximum pool and steam temperatures are presented in Table 18. The high repeatability suggests the results are a good indication of the maximum temperatures achievable with this collector-boiler design during this time of the year (with higher temperatures possible in December or January).

Table 18 Maximum boiler pool and steam temperatures

Day	T_p (°C)	T_{b-st} (°C)
14 Feb 2023	104.7	103.1
16 Feb 2023	104.7	103.2
18 Feb 2023	104.9	103.2

6.2.3 Heat Engine Thermal to Mechanical Energy Conversion

The estimated shaft output power, calculated using Equation (2) and the relationship between thermal efficiency and expansion ratio (as discussed in Chapter 5.1.1), is presented in Figure 43. The peak output power was 119, 125, and 128 W; the mean output power was 111, 112, and 114 W; and the daily total output energy per unit area was 0.036, 0.035, and 0.046 kWh_m/m^2 on 14, 16, and 18 February, respectively.

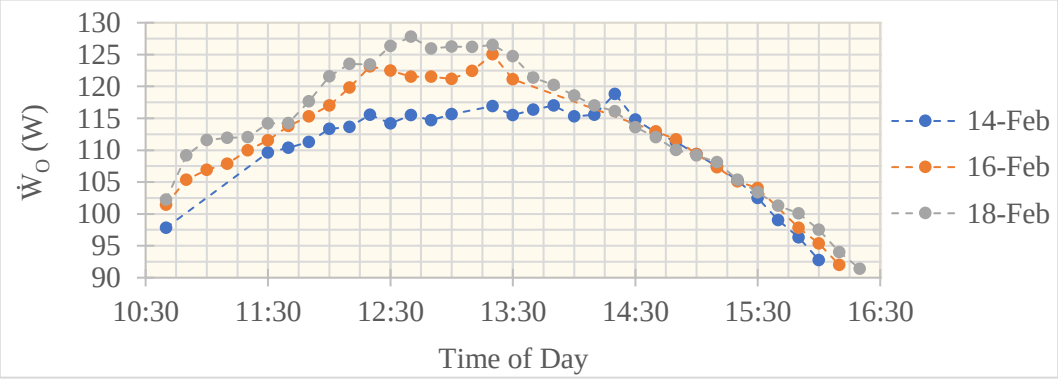

Figure 43 Estimated engine mechanical power variation with time during test days

The mechanical power output is notably lower than the ORCs in Müller and Howell (2021) with a mean estimated thermal efficiency of 2.18 % (affected by the expansion ratio, which in turn depended on the steam generation rate) compared to 4.2 to 6.8 % for the ORCs. However, it should be noted that the thermal efficiency of 2 % for an expansion ratio of r_{exp} = 1 is a conservative value, seeing as the Hathorn and Davey engine of 1885 was able to generate up to 3.7 % thermal efficiency without expansion. Therefore, the power output would only be competitive with ORCs if the thermal efficiency of the condensing engine were optimised to get closer to the theoretical values, which Müller and Howell (2021) suggested is practicably possible.

The Carnot efficiency is presented in Figure 44, which had peaks of 17.3, 18.5, 18.0 %; and mean values of 15.8, 16.6, 15.6 % on 14, 16, and 18 February, respectively.

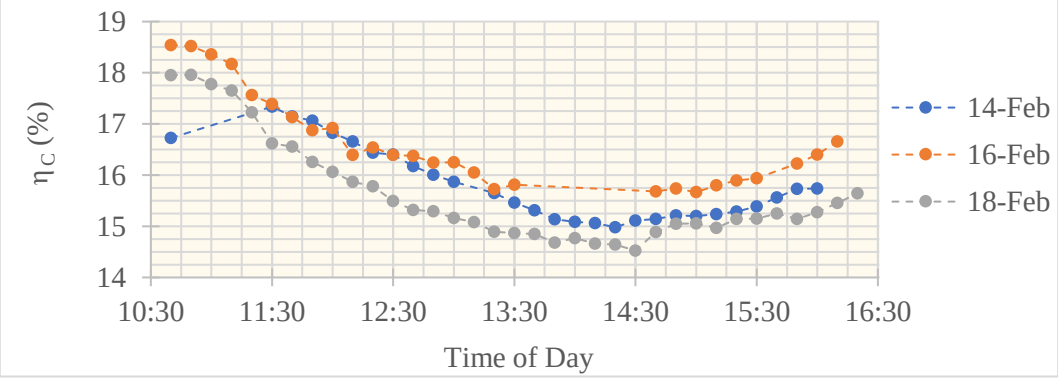

Figure 44 Carnot efficiency variation with time during test days

The thermal efficiency is presented in Figure 45, having had mean values 2.17, 2.19, and 2.17 %; and peak values 3.02, 3.08, and 3.14 % on 14, 16, and 18

February, respectively. The thermal efficiency is at a minimum of 2 % for most of the middle part of the day because the output power is maximised by running at an expansion ratio of r_{exp} = 1 (less efficient than with expansion) for all steam generation rates greater than or equal to the rated 2.56 g/s, as explained in Chapter 5.1.1.

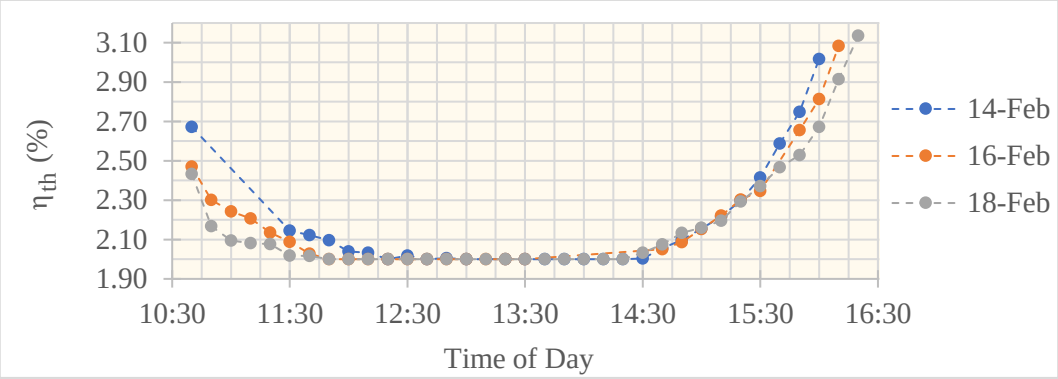

Figure 45 Thermal efficiency variation with time during test days

The Second Law efficiency, shown in Figure 46, had peak values of 19.2, 18.5, and 20.0 %; and mean values of 13.7, 13.2, and 13.9 % on 14, 16, and 18 February, respectively.

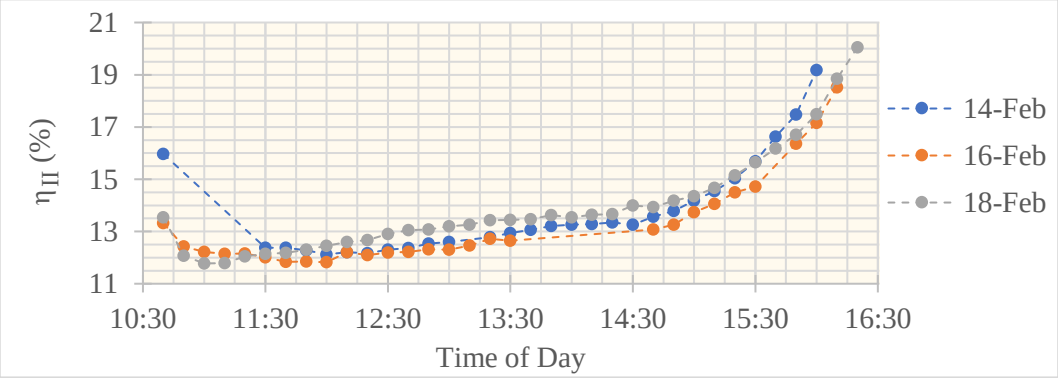

Figure 46 Second Law efficiency variation with time during test days

The condenser outlet temperature is presented in Figure 47, illustrating that the condenser subcooled close to the engineering specification, as per Chapter 4.1, of 40 °C or below, with an overall mean observed condenser temperature of 42.4 °C and maximum of 48.3 °C. As such, the associated maximum saturation pressure is 0.113 bar (abs), which means the minimum inferred pressure differential across the piston is 0.9 bar and on average is 0.93, compared to the engineering specification of 0.94.

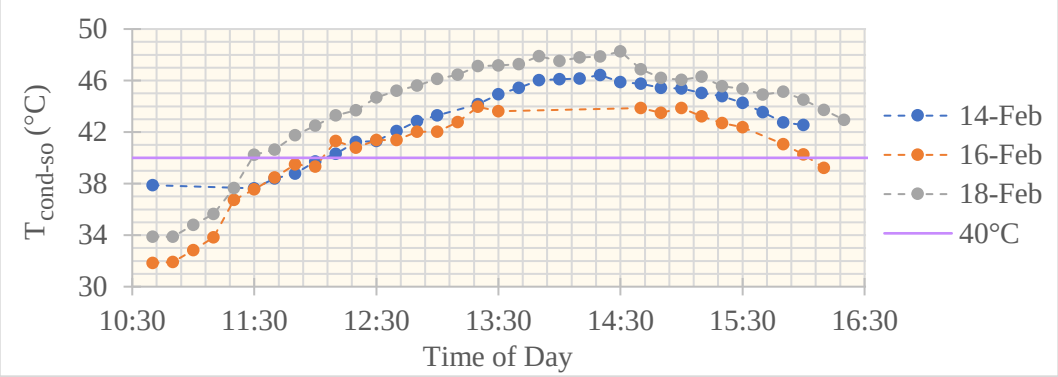

Figure 47 Condenser steam side outlet temperature variation with time during test days

The primary reason why the condenser steam-side outlet temperature varied throughout the test period was because the WRS was unable to supply coolant water at a consistent, low temperature because the 1600-L water storage tank for recooling (chilling) was slightly undersized and could not dissipate the heat gained at a fast enough rate.

6.2.4 Mechanical to Electrical Energy Conversion

The estimated electrical power output was determined using a mechanical-to-electric conversion efficiency of 80 %. The peak electrical power output was 95.1, 100, and 102 W; the mean electrical output power was 88.5, 89.6, and 91.1 W; and the daily total electrical output energy per unit area was 0.029, 0.028, and 0.037 kWh_e/m^2 on 14, 16, and 18 February, respectively.

6.2.5 Overall Energy Conversion

The conversion efficiency from solar to mechanical energy (η_{G-m}) had peak values 0.92, 0.85, and 0.90 %; and mean values 0.80, 0.78, and 0.80 % on 14, 16 and 18 February, respectively. Therefore, the overall mean solar-to-mechanical energy conversion efficiency is 0.79 %, which can be used with monthly GTI data to estimate monthly (and therefore annual) mechanical generation.

Furthermore, the conversion efficiency from solar to electrical energy (η_{G-e}) had peak values 0.74, 0.68, and 0.72 %; and mean values 0.64, 0.62, and 0.64 % on 14, 16 and 18 February, respectively. Therefore, the overall mean solar-to-electrical energy conversion efficiency is 0.63 %, which can be used with monthly GTI data to estimate monthly (and therefore annual) electrical generation.

The overall efficiencies are exceedingly low compared to both ORCs and solar PV systems but since the system is designed for co-generation, one needs to first consider the distillation performance of the system before making a conclusion about the performance of the overall system.

6.3 Distillation

6.3.1 Distillate Production Rate

Figure 48 shows the average hourly distillate production rate (DPR) as measured during the experiment (possible due to bypass of the engine in this experiment). Distillate production only began around 10h30 on each day, so the average hourly DPR is only recorded from 11h00 and takes some time to ramp up until it starts to follow the same characteristic profile as the GTI input. The total distillate produced was 38.5, 43.0, and 44.8 L/day on 14, 16 and 18 February, respectively.

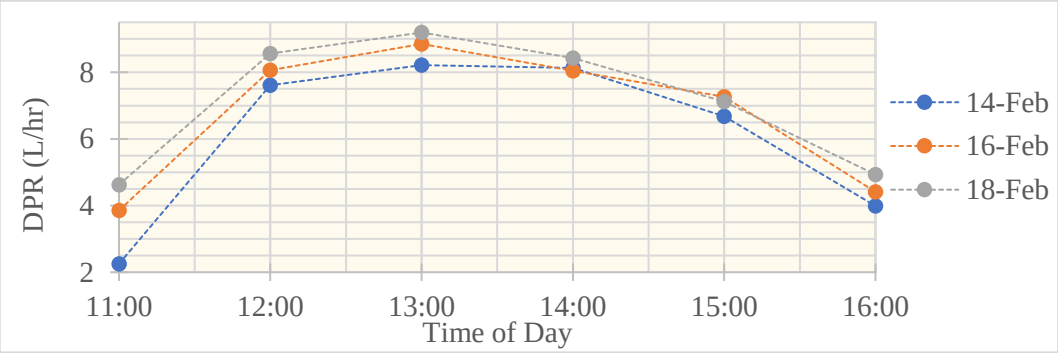

Figure 48 Hourly distillate production rate variation with time during test days

6.3.2 Specific Energy Consumption

The SEC (kWh_{solar}/m^3) is presented in Figure 49. 11h00 for 14 February and 14h00 for 16 February are excluded due to the cloud cover during these periods.

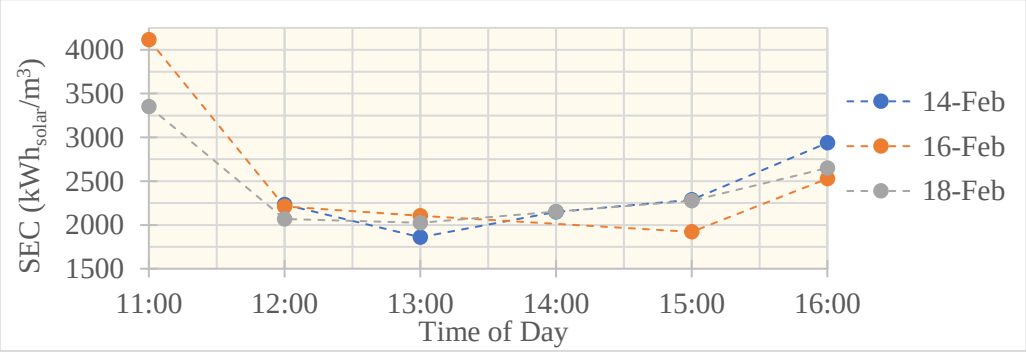

Figure 49 Specific energy consumption variation with time during test days

The mean SEC from 12h00 (once the SEC was stable) to 16h00 (when the SEC starts to increase rapidly as the solar resource quality diminishes towards the end of the solar day) was 2293, 2191, and 2234 kWh_{solar}/m^3 on 14, 16, and 18 February, respectively. The total daily mean (total solar energy divided by total distillate produced) was 2198, 1942, and 2234 kWh_{solar}/m^3 on 14, 16, and 18 February, respectively. Therefore, the overall mean for the three days was 2125 kWh_{solar}/m^3.

The mean SEC observed in this analysis is significantly higher than the existing solar desalination technologies discussed in Chapter 2.3.2, which generally operate well below 100 kWh_{solar}/m^3. The most prominent solar thermal desalination technologies – MSF and MED – operate between 30 and 90 kWh_{solar}/m^3, which significantly outperforms the system in this experiment. The lowest SEC noted in Chapter 2.3.2 was 4 kWh_{solar}/m^3 by PV-RO desalination. Considering these existing technologies, this prototype is not competitive based on SEC.

The variation in SEC across the three days was reasonable from 12h00 onward (standard deviation less than 10 % for each time step), suggesting good repeatability of the results, and implies these results are representative of what may be expected in terms of system performance in summer-time sunny conditions.

6.3.3 Thermal Inactivation Potential

The pool (lower, middle, and upper) temperature remained between 100 and 105°C for the entire boiling period for all three tests (at least for the 10-minute averages). The mean pool temperature is presented in Figure 50.

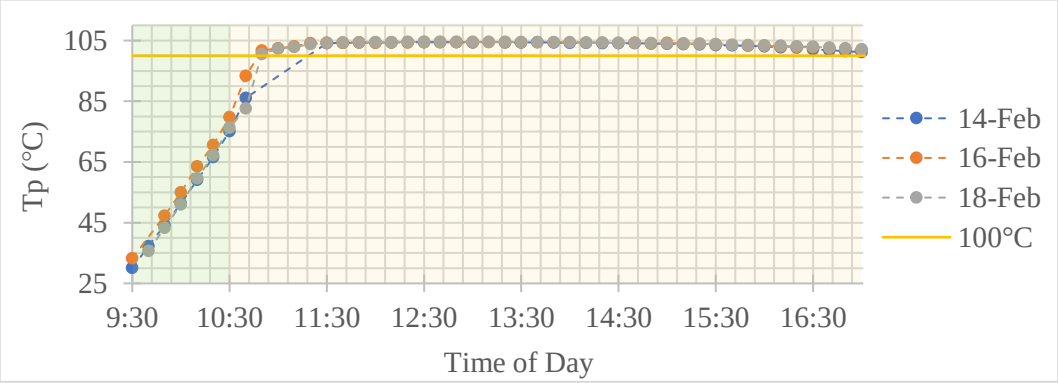

Figure 50 Mean pool temperature variation with time during test days

Apart from momentary temperature drops during cold water addition, the lower section of the pool remained within 1 °C of the upper section of the pool from approximately 11h00 onward, and the middle and upper sections of the pool appeared virtually unaffected by the addition of cold water. Furthermore, for the pool volume of ~50 L and water usage (steam supply) at approximately 0.16 L/min

in liquid terms (about 0.3 % of the total pool volume per minute) most of the pool remained close to 100 °C for extended periods, which appears sufficient for deactivation of the bio-contaminants as discussed in Chapter 2.3.3.

6.4 Longer-Term System Performance

6.4.1 Monthly and Annual GTI Resource

Monthly GTI was obtained from SOLARGIS (2022) for a north-facing collector at a 30° inclination, located in Stellenbosch (33.928425°S and 18.864944°E), as shown in Figure 51. The total annual GTI is 2149.7 kWh_{solar}/m^2 at this location.

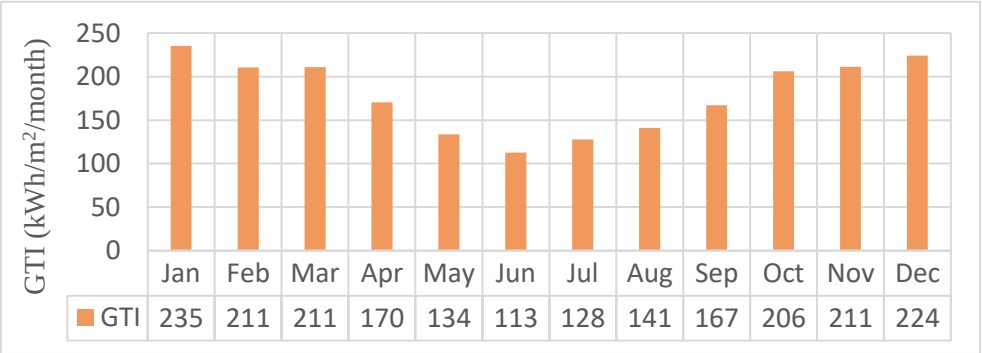

Figure 51 Monthly GTI

6.4.2 Monthly and Annual Power Generation

From the monthly GTI distribution in Figure 51 and the average solar-to-mechanical power efficiency of 0.79 % and mechanical-to-electric efficiency of 80 %, the estimated monthly specific mechanical and electrical energy generation were determined, as presented in Figure 52.

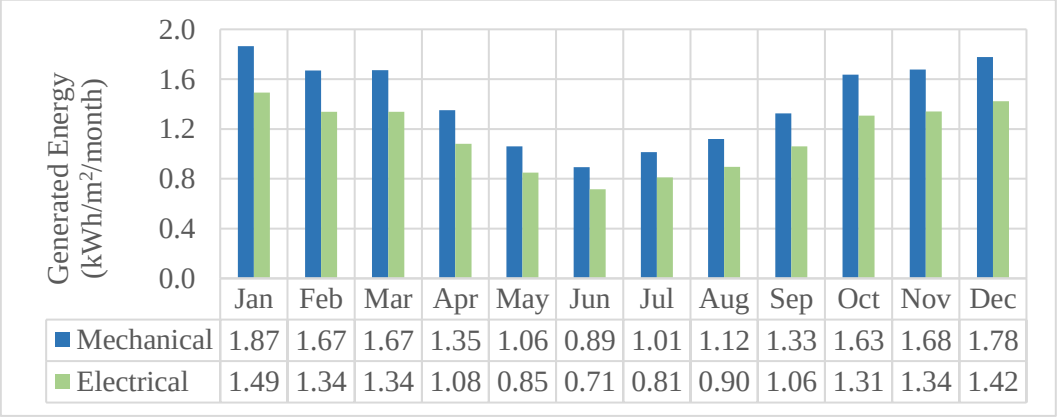

Figure 52 Monthly mechanical energy output

This equates to an annual mechanical energy generation of 17.1 kWh_m/m^2/annum and annual electrical energy generation of 13.6 kWh_e/m^2/annum.

As such, the electrical generation of this system is expected to be approximately 0.047 kWh_e/m^2 per day in summer, assuming 28 days in February, and 0.026 kWh_e/m^2 per day in winter. These values are notably low if you consider the Free Basic Electricity (FBE) policy in South Africa allocates 50 kWh_e/month electricity to low-income households (Department of Energy, 2012), which for a 30-day month would require a system with a solar array of up to 65 m^2 (27 XCPC collectors), and at 30° inclination requires a 56 m^2 area, excluding spacing between collectors, which is approximately the floor size of a low-cost house in South Africa – 53 m^2 (Mabuya and Scholes, 2020).

6.4.3 Monthly and Annual Clean Water Production

From the monthly GTI distribution in Figure 51 and the daily average SEC of 2125 kWh_{solar}/m^3, the estimated monthly distillate production was determined, as presented in Figure 53, which equates to a total annual amount of 1012 L/m^2.

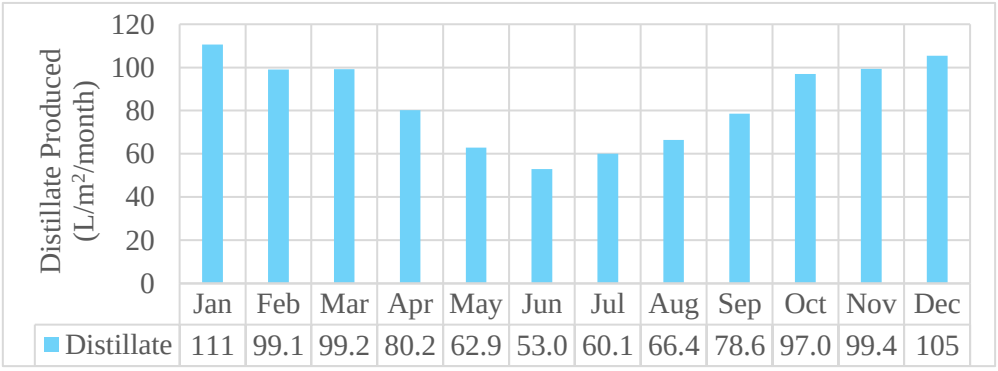

Figure 53 Monthly distillate production

The average daily distillate production is 3.50 L/m^2 in summer and 1.91 L/m^2 in winter. As discussed in Chapter 2.3.2, existing solar desalination technologies, such as PV-RO, have SECs as low as 4 kWh_{solar}/m^3, which means they can produce up to about 530 times more for the same solar irradiance and aperture area. Thus, the system is also clearly not competitive in terms of water purification efficacy.

6.4.4 Comparison with PV

A comparison is done here with a commercially available power source – namely, solar PV – which can be used for both electricity generation and to purify water

using PV-RO, thus giving the same two outputs as the system investigated in this work.

As per SOLARGIS (2022) data, a 1 kW_p solar PV system operating in the same location as this experiment would produce an average of 5.76 kWh_e/day in summer and 3.43 kWh_e/day in winter. A 1 kWp PV panel is commonly available in sizes between 1 and 2 m^2. Furthermore, assuming an SEC of 0.5 kWh_e/m^3 for PV-RO (typically ranges from 0.5 to 3 kWh_e/m^3, as mentioned in Chapter 2.3.2), a 1 kW_p PV-RO system would produce 11.52 m^3/day in summer and 6.86 m^3/day in winter.

Using the FBE amount of 50 kWh_e/month as the reference, a 65 m^2 XCPC array in the system considered in this work would generate 50.7 kWh_e/month and produce 3725 L/month distilled water in winter. On the other hand, a 0.5 m^2 PV panel (assuming a 1 kW_p panel has a size of 1 m^2) would be sufficient to generate 51.45 kWh_e/month in winter and an additional 0.5 m^2 PV panel can produce the 3725 L in a single day compared to a month by the 65 m^2 XCPC array.

Therefore, a 1-2 m^2 PV panel could outperform a 65 m^2 version of the 14.46 m^2 prototype built in this study in both electricity and clean water generation, which illustrates clearly that this system is not feasible compared to commercially available technology, which is also much less complex.

6.5 Performance Summary

Table 19 provides a summary of the performance analysis, which highlights the specific areas where the system achieved or underperformed relative to expectations and the engineering requirements in Chapter 4.1.

Table 19 Performance analysis summary

Criteria	Rating/Comment
SSGS performance	The SSGS demonstrated steam generation capability up to and above the condensing engine rated requirement of 2.56 g/s and between 0.8 and 1.5 bar (abs) for a sunny day with a GTI peak > 1000 W/m^2, but not up to four hours as per engineering requirement 1.1. The primary reason for underperformance of the SSGS is the lower collector efficiencies compared to the rated efficiency – suspected to be due to collector defects related to the absorber tube and fin, and because the rated efficiency parameters are not valid near the start and end of the solar day. Engineering requirement 1.1 was partially satisfied, while 2 and 4 were satisfied.

Table 19 (continued)

	The collector to boiler heat gain efficiency of < 100 % suggests heat loss in the collector array piping could be reduced somewhat. The boiler performed well, with an overall average effectiveness of 79.4 %, demonstrating steam generation rates ≥ 2.56 g/s, suggesting a good design, with adequate sizing and interfacing with the collector array. The boiler was equipped with 6 kW electrical heaters, which satisfies engineering requirement 5.
Condenser performance	The WRS was unable to supply cooling water at a consistently low temperature, which resulted in a condenser outlet temperature above the required 40 °C – up to 48.3 °C. Engineering requirement 3 was partially satisfied because condensation at > 2.56 g/s was demonstrated.
Power output	The power output is low compared to existing low-grade heat power generation technology, such as ORCs. However, the potential remains that the condensing engine can outperform ORCs on Second Law efficiency. However, this will require higher thermal efficiencies only yet proven theoretically and not experimentally. Furthermore, compared to commercial technology such solar PV, this prototype is not competitive and requires significantly more land or roof area for installation.
Thermal inactivation	The boiler pool is maintained at sufficient temperatures and for periods suitable for inactivation of the bio-contaminants in WHO (2015).
Distillate production	The SEC is notably high compared to existing desalination technology and this prototype therefore does not compete with these technologies based on SEC.

Furthermore, the system was designed according to relevant standards (SANS 347:2012, SANS 460:2011, and TIASA:2001) to be safe, satisfying engineering requirement 6. Once installed, the system was simple to start up and ran without much user input, and some maintenance required during the project was very straightforward, satisfying engineering requirement 7.

7 Conclusion

A concept for low temperature solar thermal combined power and clean water co-generation was investigated, aimed at addressing the United Nations SDGs 6 and 7. The system consists of a 6.5 kW_{th} solar thermal steam generator coupled with a reciprocating expander condensing engine. A prototype was developed in this project, consisting of a 14.46 m^2 XCPC solar collector array and kettle-type boiler, coupled with a condensing engine. The University of Southampton designed the engine, and it was subsequently manufactured and assembled in this project. Unfortunately, the engine did not operate correctly and, due to time constraints and the low feasibility of the system, efforts to incorporate the engine were abandoned. Thus, the SSGS and condenser were tested to demonstrate that the system could in practice provide the engine rated operating inlet/outlet conditions. The SSGS demonstrated reliable and consistent performance, generating steam at the engine design rate of 2.56 g/s, and up to a maximum rate of 2.85 g/s, while the condenser condensed all the steam and subcooled to an overall average temperature of 42.4 °C. The non-imaging XCPC in a non-tracking format was confirmed to be a suitable collector and the array had been sufficiently sized in conjunction with the boiler, using the MATLAB collector-boiler model. However, it was observed that the XCPC collectors performed below their rated efficiency. The primary suspected cause is a defect related to sagging of the absorber tube near the centre of the span causing separation between the absorber tube and fin near the ends of the evacuated tube.

From the results of the three daily on-sun tests, the SEC for distillate production (overall mean of 2125 kWh_{solar}/m^3); mechanical energy output (overall daily mean of 0.039 kWh_m/m^2) and electrical energy output (overall daily mean of 0.031 kWh_e/m^2) per unit collector aperture area were estimated using the measured boiler thermal input and the heat engine thermal efficiency from literature for a variable expansion ratio (r_{exp} = 1 to 4 for η_{th} = 2 to 5.5 %, respectively). Furthermore, the monthly and annual distillate production and energy generation were estimated, which indicate the longer-term expected outputs of the system. The results, when compared with existing technologies – namely, ORCs for low-grade heat power generation and commercial solar power generation technology such as solar PV; as well as solar desalination technologies such as solar-powered PV-RO, ED, MSF, and MED – suggest this prototype is not competitive, due to the low efficiency observed for both power generation and water purification. It was shown that a 1-2 m^2 solar PV system could provide the same power and significantly more clean water than a 65 m^2 version of the system investigated in this study.

Therefore, this concept does not seem feasible given the low efficiencies combined with high complexity. If the thermal efficiency of the condensing engine could be improved to approach the theoretical values suggested in literature, this system could be competitive with ORCs for Second Law efficiency in applications such as waste heat recovery. Similarly, the XCPC collectors are promising for other applications, such as low-grade process heat.

Appendix A Additional Figures

An aerial view of the test facility is shown in Figure 54 with the red location icon positioned in the centre of the collector array.

Figure 54 Satellite aerial view of test facility (SOLARGIS, 2022)

Figure 55 and Figure 56 show the hourly averaged wind speed and wind direction, respectively, obtained from Brooks et al. (2015).

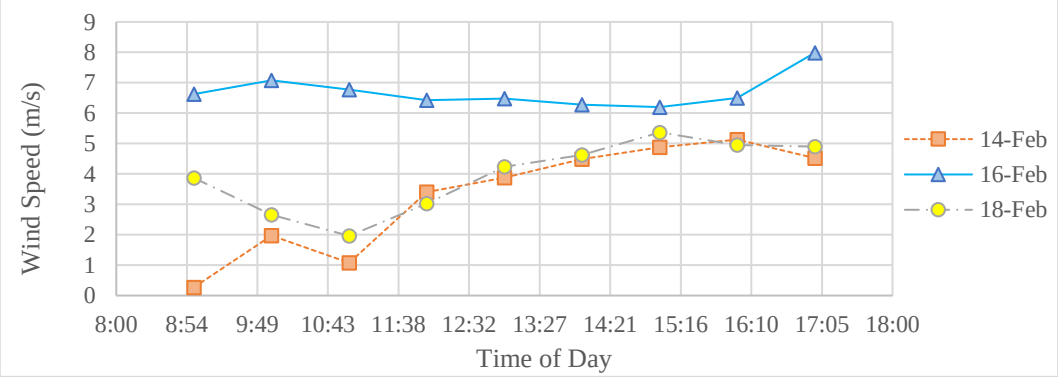

Figure 55 Hourly wind speed

Note for Figure 56:

- North to south = 0/360°
- West to east = 90°
- South to north = 180°

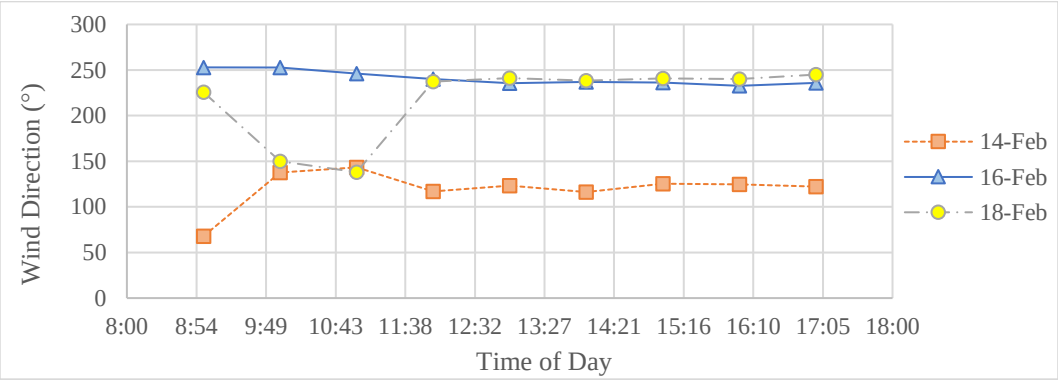

Figure 56 Hourly wind direction

Appendix B Standard Deviation Summary

The information presented in this report is either in the form of 10-minute, hourly or daily averages. The 10-minute averages were used to determine the hourly and daily averages. It was important to quantity the random uncertainty in the data brought about by fluctuation within the 10-minute samples. This was done by calculating the standard deviation for each 10-minute sample (in some cases a 1-minute sample was taken for the standard deviation calculation if the data was on a steep gradient). Table 20 presents the mean and maximum standard deviation for the respective measured variable.

Table 20 Standard deviation summary for measured data

	14 Feb 2023		16 Feb 2023		18 Feb 2023	
Measured variable	**Mean (%)**	**Maximum (%)**	**Mean (%)**	**Maximum (%)**	**Mean (%)**	**Maximum (%)**
GTI	1.48	3.52	1.36	4.49	1.44	5.03
T_a	0.80	2.78	0.65	1.24	0.60	1.39
P_{b-st}	0.58	2.55	0.67	3.0	0.53	2.31
P_s	0.23	1.17	0.22	0.76	0.15	0.85
T_{b-st}	1.05	7.14	0.19	0.55	0.20	0.68
T_{p-upp}	1.03	9.01	0.22	0.78	0.23	0.84
T_{p-mid}	1.10	9.65	0.26	1.30	0.26	0.97
T_{p-low}	0.84	6.33	0.47	4.84	0.52	6.25
T_{ei}	0.36	7.01	0.06	0.16	0.05	0.09
T_{eo}	0.13	1.26	0.02	0.08	0.03	0.11
$T_{cond-so}$	0.77	5.00	1.03	4.67	0.80	3.45
$T_{cond-ci}$	0.62	6.19	0.41	1.35	0.41	1.08
$T_{cond-co}$	0.86	5.88	0.75	2.70	0.67	2.32
T_{HTF-bo}	0.91	7.49	0.18	1.01	0.16	0.64
$T_{HTF,ci-A}$	0.92	7.58	0.19	0.88	0.17	0.68
$T_{HTF,co-A}$	0.96	6.17	0.29	0.62	0.27	0.69
$T_{HTF,co-B}$	0.89	6.48	0.21	0.62	0.19	0.65
$T_{HTF,co-C}$	0.88	6.00	0.21	0.68	0.19	0.67
T_{uw}	4.58	11.7	4.20	15.4	4.94	11.28
$\dot{V}_A$	0.48	1.77	0.46	1.74	0.53	0.82

Appendix C Major Engine Defects

The major suspected reasons why the engine did not operate are leakages, which allow air into the cylinder to prevent the requisite vacuum from forming in the cylinder, and excessive friction due to manufacturing defects.

The leaks were identified when the solenoid valves at both cylinder inlets and outlets were closed once a vacuum had been drawn by the electric vacuum pump, and the cylinder pressure measurements on both cylinders clearly showed how the vacuum was lost as the pressure rose from below 0.3 bar (abs) back to 1 atm. This raises the concern regarding manufacturing tolerances and the author's opinion is that the cylinder and jacket design, as well as the various pipe fittings required, provide too much opportunity for leaks and this significantly increases installation time to identify and fix these leaks.

Higher-than-desired friction between the piston and cylinder, and/or mechanical resistance in the gears and cranks, is suspected because when turning the engine there was a distinct section of the cycle where the resistance to turning increased significantly, which could be caused by the walls of the cylinder or piston tapering slightly, which is a possibility when boring such long strokes (160 mm).

Appendix D Thermocouple Calibration

Figure 57 shows the measured error at each reference temperature for the fifteen T-type thermocouples during calibration. The reference temperature, with respect to which the error was calculated, was measured using a high-accuracy RTD and a Fluke Field Meteorology Well.

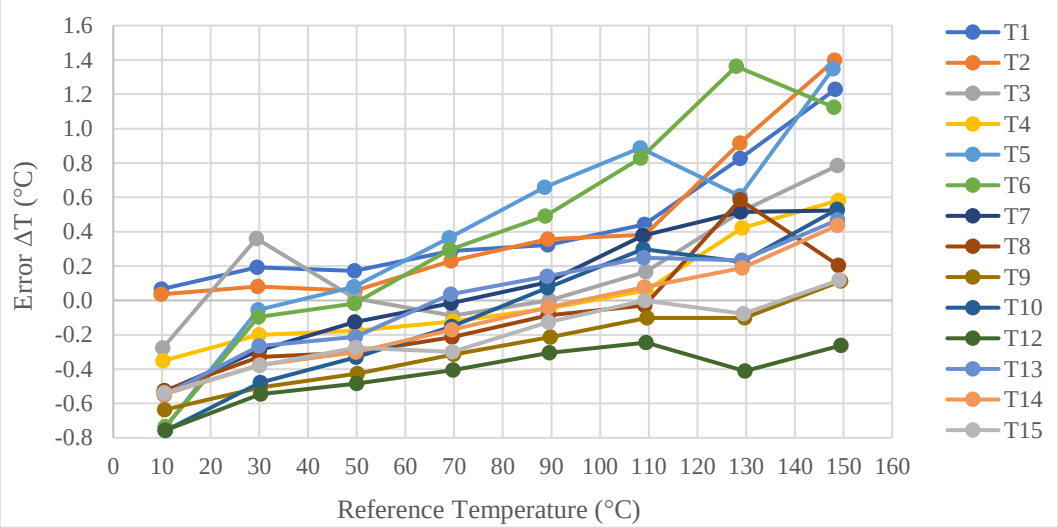

Figure 57 Thermocouple calibration error plot

During the calibration procedure, the field meteorology well aimed to reach the specified temperature (e.g., 100°C) in the well, using its heating and cooling functions, but then the actual temperature measured by the calibrated RTD was output from the well as a resistance value corresponding to the actual temperature (e.g., 100.15°C). The relationship between resistance and temperature for the RTD was found on the calibration certificate in the form of the 2nd-order polynomial in Equation (44).

$$T_{Ref\ RTD}(\Omega) = 0.0013\Omega^2 + 2.2922\Omega - 241.93\ (°C) \qquad (44)$$

From the thermocouple measurements and the corresponding RTD measurements, the maximum error across the range of 10 to 150°C was determined for each thermocouple and deemed to be within the expected range for calibrated T-type thermocouples, such that the error listed in Table 15 is correct. The actual temperatures measured in the experiment were well within the calibrated range.

Appendix E Pressure Transducer Calibration

The four BD DMP331 pressure transducers were calibrated by the manufacturer between the pressure limits of 0 and 3 bar (abs), with full scale accuracies of 0.35 % for P_b, P_{C1}, and P_{C2}, and 0.1 % for P_{eo}. As a simple validation, the transducers were also compared to the measurements of a FLUKE 700G31 digital pressure gauge. The pressure was controlled with a FLUKE 700PTP1 pneumatic test pump with vacuum generation capability.

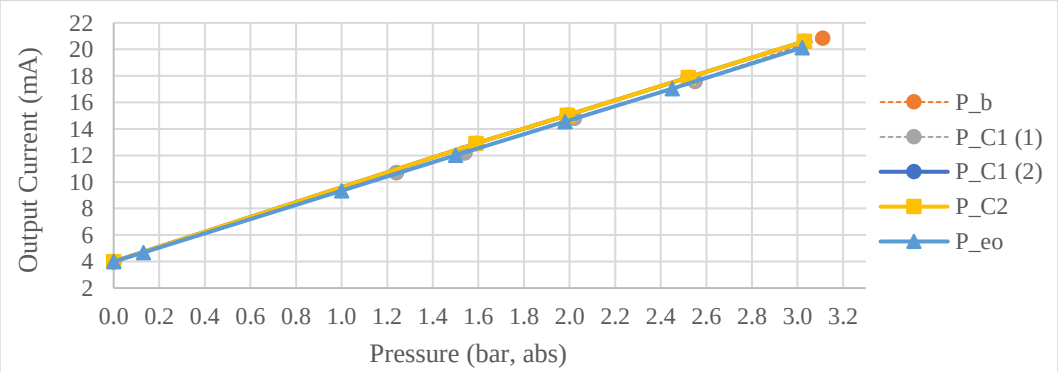

Figure 58 Pressure transducer calibration plot – pressure vs output current

The calibration occurred in three parts. The first test was with transducers P_b and P_{C1}, the second with P_{C1} and P_{C2} and the fourth with P_{eo}. All the transducers showed a linear relationship between the output current and pressure in agreement with the design range of 0 to 3 bar (abs). The slight deviation between $P_{C1(1)}$ and $P_{C1(2)}$ shows the systematic error in this test (due to the test not the transducers), since $P_{C1(1)}$ and P_b were essentially equal, and $P_{C1(2)}$ and P_{C2} were essentially equal, so the deviation of P_{C1} is likely due to a small leak in the test apparatus (a T-junction with two transducers and the reference gauge connected). In conclusion, the manufacturer calibration took precedence, but the calibration performed by the author confirmed the pressure transducers behaved as expected when connected to the relevant data acquisition device.

Appendix F Solar Measurement Calibration

The KIPP and ZONEN CMP6 pyranometer used in this project for direct GTI measurement was calibrated by GeoSUN AFRICA in 2020, according to the calibration certificate on the following page. According to the KIPP and ZONEN manual for CMP pyranometers, the CMP6 gives an output signal as a voltage between 0 and 30 mV, corresponding to insolation of 0 to 1500 W/m^2. The relationship between output voltage and solar irradiance is presented in Equation (45).

$$G(V) = \frac{V}{S} \tag{45}$$

G is the solar irradiance, V is the pyranometer output voltage, and S is associated the calibration factor, which, according to the manual should be $S = 20\ \mu V \cdot m^2/W$. However, the calibration certificate gives $S = 19.60\ \mu V \cdot m^2/W$, which corresponds to a range of 0 to 1530 W/m^2 for an output voltage of 0 to 30 mV.

Calibration Certificate

GeoSUN AFRICA

Pyranometer ISO 9847 Calibration Certificate Number: GSACA-0943

Calibrated Instrument

Instrument: Pyranometer
Manufacturer: Kipp & Zonen
Model: CMP6
ISO 9060:1990 Class: First Class

Calibration Date: 07 February 2020
Serial Number: 101194
New Sensitivity: 19.60 µV/W/m²

Calibration Methodology

GeoSUN performed an indoor calibration through exposure of both the calibrated instrument (instrument under test) and a reference instrument to an artificial light as radiation source and comparing the sensor outputs. The instruments were installed on a common horizontal base and regularly checked to ensure that it remained clean and level for the duration of the reference data being collected. The calibration was performed in accordance with the ISO 9847 (1992) standard, procedure type IIc.

Reference Instrument and its Traceability

The reference instrument is a Kipp & Zonen CMP21 pyranometer (SN 110811). The instrument was calibrated on 8 November 2019 at ISO-CAL North America against absolute cavity radiometer AHF–28560 which successfully participated at IPC-XII with the World Standard Group of radiometers. The location of ISO-CAL is at 20th street, Phoenix, Arizona in the USA at latitude 33.8176944°, longitude -112.0396083° and altitude 570 m AMSL. The reference instrument was calibrated at normal incidence with the sun and sky radiation as the source using the "alternating sun-and-shade method". The readings are referenced to the World Radiometric Reference (WRR) as stated in the WMO Technical Regulations, originally with an SI relative uncertainty estimated at ±0.3%. The diagram on the right shows the traceability hierarchy.

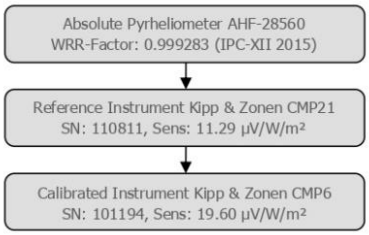

Absolute Uncertainty

The absolute uncertainty is the combined result of three uncertainties namely:

1) The expanded uncertainty during calibration of the reference instrument, given as ±0.44%.
2) The uncertainty in the correction of directional errors (cosine errors), estimated by scientific judgement as ±0.5%.
3) The expanded uncertainty of the transfer procedure (calibration by comparison), estimated by scientific judgement as ±1%.

The combined expanded uncertainty is the root sum of the squares, resulting in $\sqrt{(0.44^2 + 0.5^2 + 1^2)} = \pm 1.20\%$.

Calibration Environment, Results and Instrument Status

The calibration was performed at latitude -33.96543°, longitude 18.83626° and altitude 134 m AMSL and was concluded on 07 February 2020 at 10:24. A calibration was done using the measured output of the test instrument, of which the calibration environment and results are stated below. The measurement results recorded in this certificate were correct at the time of calibration. The subsequent accuracy will depend on factors such as care, handling and frequency of use. The calibration certificate or report may not be reproduced except in full, without the written approval of the laboratory. Considering the operating conditions and the IEC 61724-1:2017 standard requirements, GeoSUN recommends an annual calibration.

Instrument	Status
Bubble Level:	Dry, Replaced
Dome:	Good
Desiccant:	Replaced

Calibration Environment -	Average [Range]
Irradiation:	423 [422 - 424] W/m²
Ambient Temperature:	27.0 [26.8 - 27.1] °C
Reference Instrument Temp.:	27.1 [26.9 - 27.3] °C

Original	Calibration
Original Sensitivity:	19.83 µV/W/m²
Original Calib. Date:	16 December 2009

Calibration	Results
New Sensitivity:	19.60116 µV/W/m²
Sensitivity Standard Deviation (σ_{n-1}):	0.00463 µV/W/m²
Calibration Uncertainty (k = 2):	±0.2355 µV/W/m² (±1.20%)
Data Quantity :	4 Series, 16 Samples
Next Calibration:	February 2021

Calibrated by: W.C. Engelbrecht

Authorised by: M.L. de Jager

ISO 9001:2015

GeoSUN Africa (Pty) Ltd
Unit 1, CS Africa Building, 1 Meson Street, Techno Park, Stellenbosch, South Africa
info@geosun.co.za, www.geosun.co.za,+27 21 882 8354

Appendix G Flowmeter Calibration

The collector loop flowmeter was calibrated by testing at various flowrates within the range relevant to the experiment (up to 250 L/hr). The data from the flowmeter was recorded on an Agilent 34972A DAQ, using Agilent Benchlink Data Logger 3 software. The wires over which the signal was transmitted from the flowmeter to the DAQ were approximately 30 m long. Alternatively the flowmeter has USB compatibility that allows it to be connected directly to a PC or laptop and data is recorded using the Winsmeter TH7 software, which records the output current via the USB cable and calculates the flowrate based on the most recently entered calibration parameters, which were the factory entered values.

The flowmeter output signal recorded on the DAQ was within 0.2 % of the current measured over the short USB cable, which showed the length of cable had a negligible effect on the recorded output signal. The two signals are plotted together in Figure 59 with respect to the flowrate which was manually recorded from the analogue meter. The correlation was good between the measured output and the factory calibration of 4 to 20 mA corresponding to 0 to 250 L/hr.

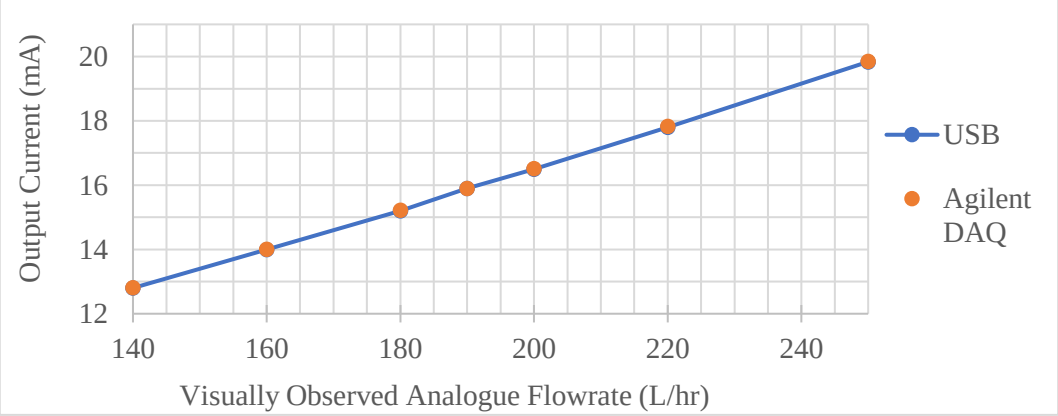

Figure 59 Output signal vs analogue flowrate reading

As such, the calibration was more of a general validation, since the factory set values for the correlation of flowrate vs output current were used – the reasons being that this was a brand-new high-quality meter and the analogue measurement is inherently inaccurate, with an estimated human visual error of about ±3 °C.

Appendix H Collector Calibration

The collector calibration was used to obtain the efficiency parameters used in the standard solar thermal collector efficiency formula, Equation (11) – η_0, a_1 and a_2. – for the range $25 < \Delta T_{ma} < 90°C$ – which is the range relevant to this study.

The purpose for determining the parameters was to gauge whether the dynamically measured efficiency parameter values corresponded to the rated efficiency parameters provided by the developer, to understand the difference between the rated and actual dynamic performance of the collectors.

Furthermore, the calibrated efficiency parameters were used to determine the flowrates and subsequently heat gain in branch B and C of the collector array, because the project budget did not allow for flowrate measurement in these branches, so heat gain could not be directly measured. The assumption was that the efficiency parameters of the collectors in the other branches would be similar within a reasonable degree of accuracy. The two collectors in branch A therefore represent a 1/3 sample of the total population of six collectors in the overall array.

The parameters were obtained from the data of the full-day test on 18 February 2023, which was a clear sunny day with no periods of cloud cover, making it the best possible day to determine the efficiency parameters over the relevant temperature range, as well as for a large portion of the solar day and for a flowrate in the same range as observed in all three performance tests (14, 16, and 18 February).

Thus, the obtained parameters account for time, temperature, and flowrate. The time element is particularly important because efficiency parameters are typically obtained under very controlled conditions near solar noon and are therefore only truly valid during that period, but these parameters are valid for the entire test period at a high level of accuracy. However, it is essential to emphasise that they will likely not be accurate for application in other times of the year and for overcast days, since the ratio of beam to diffuse were very specific, yet similar enough for the three days considered in this study to implement this strategy.

Figure 60 shows the measured GTI distribution over the test period. The profile is smooth because there were no cloudy periods throughout the test, which makes the data from this test ideal to determine the efficiency parameters, as compared to the abrupt fluctuations in the data observed on the other two full-day tests, which did not provide useful values for the efficiency parameters when the same process was used, as will be discussed below.

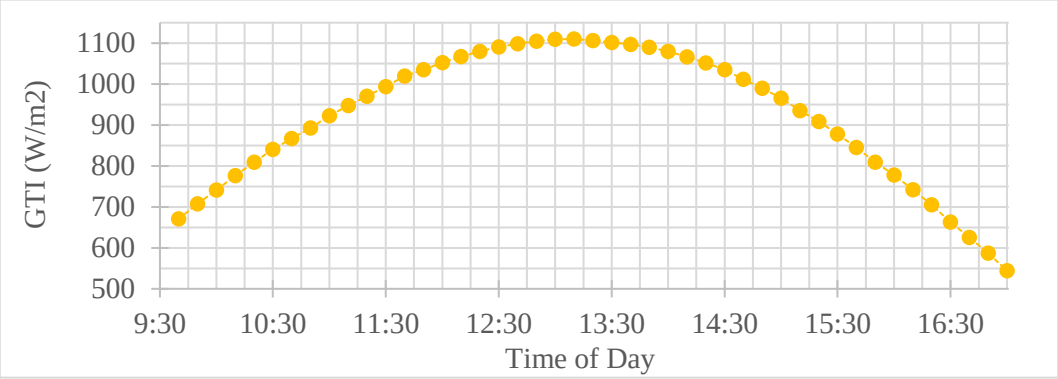

Figure 60 GTI on 18 February 2023

Figure 61 shows the ambient air temperature distribution over the test period.

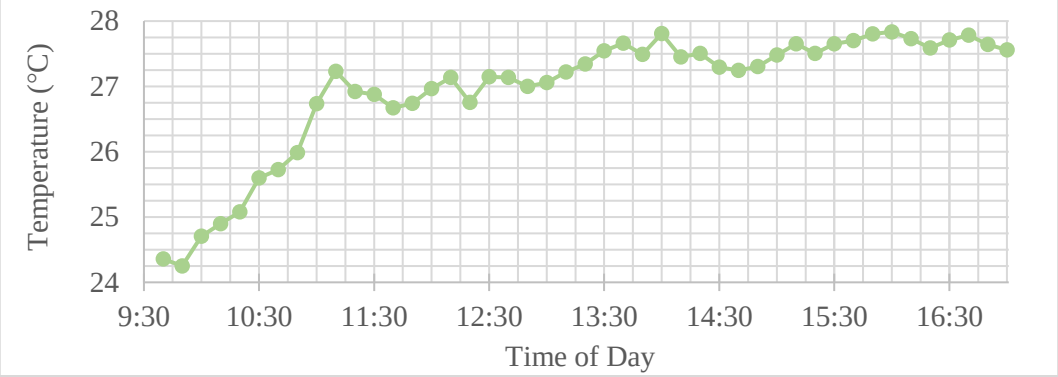

Figure 61 Ambient air temperature on 18 February 2023

The data from the entire test period was used to determine the efficiency parameters using matrix algebra, as follows:

The useful heat gain is known and was determined from the enthalpy change of the HTF over the collector row A, as per Equation (12). We also know that the useful heat gain for a collector according to Equation (11) is dependent on the solar irradiance (in this case the measured GTI) and the difference between the mean collector temperature and ambient air temperature (ΔT_{ma}). Therefore, setting Equation (11) equal to Equation (12), the only unknowns are the collector efficiency parameters.

This equation was applied to each data point and the data for each time step throughout the entire test period arranged into three matrices to fit the form **Ax** = **b**, as shown in Equation (46). These matrices were created in MATLAB and the *backslash* function used to determine **x** by **x** = **A\b**. Table 6 shows the values

obtained for the efficiency parameters compared to those specified by the developer.

$$\begin{bmatrix} Q_{u_1} \\ \dots \\ Q_{u_N} \end{bmatrix}_A = A_{aperture} \begin{bmatrix} G_1 & -\Delta T_{ma_1} & -\Delta T_{ma_1}{}^2 \\ \dots & \dots & \dots \\ G_N & -\Delta T_{ma_N} & -\Delta T_{ma_N}{}^2 \end{bmatrix}_A \begin{bmatrix} \eta_0 \\ a_1 \\ a_2 \end{bmatrix} \quad (46)$$

The maximum and mean errors between the measured useful heat gain and the useful heat gain calculated using Equation (11) and the newly determined efficiency parameters were 5.83 % and 1.94 %, respectively, over the entire test period, which included a range of temperatures and range of GTI, including various combinations of temperature and GTI.

There is also the possibility that fixing the optical efficiency in the matrix algebra would give different heat loss coefficients. To check this, the optical efficiency was fixed at the rated value of 0.57. The result was that the heat loss coefficients were even further away from the rated values ($a_1 = 4.69$ and $a_2 = -0.031$) and the maximum error over the entire test period was higher at 9 %.

The results suggest the collector optical efficiency, at least under these test conditions, is 7.4 % lower than the rated value, and the first order heat loss coefficient is 12.7 % higher than the rated value, while the second order heat loss coefficient is 10.3 % lower than the rated value. However, the former two parameters have a greater effect on collector performance at lower temperatures, such that it is clear the collector does not yield the heat gain predicted in the collector-boiler model, at least not in this dynamic application that differs from the standard calibration conditions. Nonetheless, these calibrated values were more useful for use in this experiment than the rated values.

There are a few possible reason for the difference in rated and observed values for the efficiency parameters, other than those that suggest the collectors are worse in performance than those tested by the developers. Most notably,

1. The parameters were determined for a smaller range of temperature values than by the developers. This would specifically influence the heat loss coefficients.
2. The parameters were obtained using data over a long test period as opposed to only near solar noon or for the standard calibration conditions of G_{beam} 850 W/m^2 and $G_{diffuse}$ = 150 W/m^2. However, the rated efficiency near solar noon was still significantly worse than the rated efficiency in all three tests in the analysis done in this thesis, such that the rated efficiencies were not nearly attainable in practice, which suggests inadequate performance and points to potential defects.

Possible reasons for inadequate collector performance include,

1. Damage to the absorber tube and fin due to sagging of the absorber tube near the centre of the span (as shown in Figure 62), which caused loss of contact between the tube and the fin near the ends of the evacuated tube, which would be an obvious cause for reduced heat gain. This sagging continued and about six to seven months after testing had been completed it appeared the tubes and fins in all six collectors had been significantly deformed.

Figure 62 Copper absorber tube and fin damage around 6 months after testing

2. Increased heat loss due to imperfect insulation of the collector header. Heat loss in interconnecting piping should not have affected the calibrated values because the thermocouples were placed very close to the collector inlet and outlet and the pipes were insulated.
3. Vacuum loss from the evacuated tubes. This could be a potential reason for reduced performance due to increased heat loss from the absorber tube and fin. Furthermore, if the vacuum loss is due to air penetration, then this could be a potential cause for failure of the tubes, since entrapped air would increase heating in the glass tube, and a pressure differential over the absorber tube could cause the observed deformation of the absorber tube and fin.

Appendix I External Pressure Calculation

The calculation procedure demonstrated here for the calculation of the safety factors against failure under external atmospheric pressure loading of the boiler vessel is taken from Sturm (1941), with the use of Figure 63 from Windenburg and Trilling (1934). The equations are not described in detail due to lack of space, but they are easily available in Sturm (1941).

The boiler used in this study has five buckling lobes, dependent on the geometry of the cylinder, determined from Figure 63, assuming the worst-case scenario where the vessel is filled completely with saturated steam (no liquid pool).

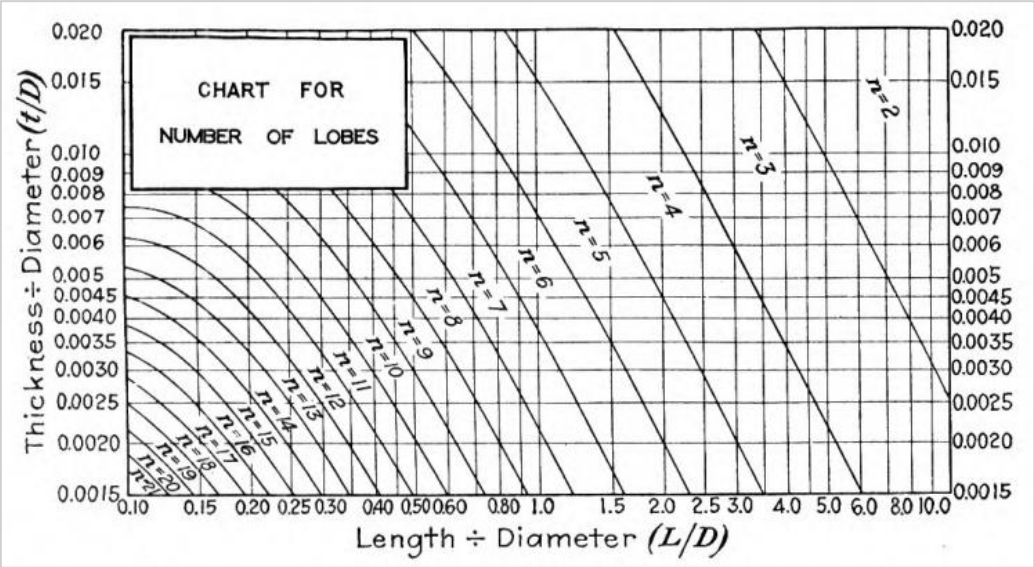

Figure 63 Collapse lobes for cylinder under uniform radial and axial load

The calculation inputs are shown in Table 21, with the subsequent calculation.

Table 21 Boiler specifications for external pressure calculation

Symbol	Property	Value	Units
L	Length excl. insulation	760	mm
D	Diameter excl. insulation	365	mm
R	Radius excl. insulation	182.5	mm
t	Wall thickness	1.2	mm
N	Number of deflection lobes at neutral equilibrium	5	-
I	Moment of inertia per unit length of shell	1.44×10^{-10}	m^3
	Poisson's ratio	2.75	-
E	Young's modulus of elasticity	193	GPa

$$I = \frac{t^3}{12} = 1.44 \text{ x } 10^{-10} \text{ m}^3 \quad (47)$$

$$\frac{L}{D} = 2.082 \quad (48)$$

$$\frac{D}{t} = 0.0033 \quad (49)$$

$$K_1 = \frac{2}{3}\frac{N^2\,(N^2\,\lambda^2 - \mu\,(\lambda - 1) - 1) - \frac{\alpha + 1 + \mu}{\alpha\,\lambda}\left(N^2\left(1 + (\lambda - 1)(2 - \mu)\right) - 1\right)}{F\,(1 - \mu^2)} = 18.14 \quad (50)$$

$$K_2 = \frac{2}{\alpha^2\,F} = 4.129 \text{ x } 10^{-5} \quad (51)$$

$$K = K_1 + K_2\left(\frac{D}{t}\right)^2 \quad (52)$$

$$W_{collapse} = K\,E\left(\frac{t}{D}\right)^2 \quad (53)$$

$$\lambda = \left(\frac{\pi\,R}{N\,L}\right)^2 + 1 = 1.023 \quad (54)$$

$$\alpha = \left(\frac{N\,L}{\pi\,R}\right)^2 + 1 = 44.93 \quad (55)$$

$$F = N^2 - 1 + \frac{1}{\alpha^2} - \frac{\mu}{\alpha\,\lambda} = 23.99 \quad (56)$$

External pressure: 1 atm = 1.01325 bar

Minimum internal pressure: 0.8 bar

Effective (net) external pressure:

$$P_{ext} = 1 \text{ atm} - 0.8 \text{ bar} = 0.213 \text{ bar} \quad (57)$$

$$SF_{collapse} = \frac{W_{collapse}}{P_{ext}} = 7.1 \quad (58)$$

$$SF_{33\%} = 33\%\ SF_{collapse} = 2.3 \quad (59)$$

Appendix J Collector-Boiler MATLAB Model

The following MATLAB code and outputs are for the case of 580 W/m^2 peak GTI and for the Artic Solar XCPC collector and boiler as implemented in the prototype built and tested in this project.

```
clear
```

Constants

```
dK = 273.15;        % [K]
g = 9.81;           % [m/s^2]
k_SS = 13.4;        % [W/m*K] - conductivity of stainless steel AISI 316 from Table
A-3
C_sf = 0.0130;      % Table 10-3 C&G water-stainless steel (mechanically polished)
n = 1.0;            % Table 10-3 C&G water-stainless steel (mechanically polished)
```

Fluid properties

**The following fluid property functions were determined from actual values in the tables of Cengel and Ghajar (2015) before the author was aware of packages such as XSteam with built-in functions. However, this has no effect on the accuracy of the results as the simulations remained well within the limits of the values used to determine the functions, and the correlation between the values and functions is evident in the visual representative figures. However, the plots have been excluded from the report for conciseness.

Prandtl number for liquid water - Pr_L

```
Pr_L = [13.5 11.2 9.45 8.09 7.01 6.14 5.42 4.83 4.32 3.91 3.55 3.25 2.99 2.75 2.55
2.38 2.22 2.08 1.96 1.85 1.75 1.58 1.44 1.33 1.24 1.16 1.09 1.03 0.983 0.947 0.910
0.865 0.836 0.832 0.854 0.902 1.00 1.23 2.06];
T2 = [0.01 5 10 15 20 25 30 35 40 45 50 55 60 65 70 75 80 85 90 95 100 110 120 130
140 150 160 170 180 190 200 220 240 260 280 300 320 340 360] + 273.15;
f_Pr_L = @(T1) spline(T2, Pr_L, T1);
T_space = linspace(0+dK, 374.14+dK);
%plot(T2-dK, Pr_L, '*', T_space-dK, f_Pr_L(T_space), '-'), legend('Data', 'Spline
fit')
```

Beta

```
T = [275 280 285 290 295 300 305 310 315 320 325 330 335 340 345 350 355 360 365
370 375 380];
beta = [0.780333 6.184114 11.45765 16.59011 21.57093 26.38963 31.03593 35.49975
39.77122 43.84070 47.69877 51.33626 54.74422 57.91392 60.83688 63.50480 65.90961
68.04338 69.89838 71.46697 72.74164 73.71494]*10^-5;
T3 = [0.01 5 10 15 20 25 30 35 40 45 50 55 60 65 70 75 80 85 90 95 100 110 120 130
140 150 160 170 180 190 200 220 240 260 280 300] + 273.15;
beta2 = [-0.068 0.015 0.0733 0.138 0.195 0.247 0.294 0.337 0.377 0.415 0.451 0.484
0.517 0.548 0.578 0.607 0.653 0.670 0.702 0.716 0.750 0.798 0.858 0.913 0.970 1.025
1.145 1.178 1.210 1.280 1.350 1.520 1.720 2.000 2.380 2.950].*10^-3;
f_beta = @(T1) spline(T3, beta2, T1);
%plot(T3-dK, beta2, '*', T_space-dK, f_beta(T_space), '-'), legend('Data', 'Spline
fit', 'Location', 'best')
```

Density of liquid water - rho_L

```
T4 = [0.01 5 10 15 20 25 30 35 40 45 50 55 60 65 70 75 80 85 90 95 100 110 120 130
140 150 160 170 180 190 200 220 240 260 280 300 320 340 360 374.14] + 273.15;
```

```
rho_L = [999.8 999.9 999.7 999.1 998.0 997.0 996.0 994.0 992.1 990.1 988.1 985.2
983.3 980.4 977.5 974.7 971.8 968.1 965.3 961.5 957.9 950.6 943.4 934.6 921.7
916.6 907.4 897.7 887.3 876.4 864.3 840.3 813.7 783.7 750.8 713.8 667.1 610.5 528.3
317.0];
f_rho_L = @(rhoL) spline(T4, rho_L, rhoL);
f_rho_L2 = @(T) 1./(1.49343E-3 - (3.7164E-6)*T + (7.09782E-9)*T.^2 -
(1.90321E-20)*T.^6); % kg/m^3
%plot(T4-dK, rho_L, '*', T_space-dK, f_rho_L(T_space), '-', T_space-dK,
f_rho_L2(T_space), '-'), legend('Data', 'Spline fit', 'Curve fit from Kroger',
'Location', 'best')
```

Density of vapour water - rho_v

```
rho_v = [0.0048 0.0068 0.0094 0.0128 0.0173 0.0231 0.0304 0.0397 0.0512 0.0655
0.0831 0.1045 0.1304 0.1614 0.1983 0.2421 0.2935 0.3536 0.4235 0.5045 0.5978 0.8263
1.121 1.496 1.965 2.546 3.256 4.119 5.153 6.388 7.852 11.60 16.73 23.69 33.15 46.15
64.57 92.62 144.0 317.0];
f_rho_v = @(T) spline(T4, rho_v, T);
f_rho_v2 = @(T) -4.062329056 + 0.10277044*T - (9.76300388E-4)*T.^2 +
(4.475240795E-6)*T.^3 - (1.004596894E-8)*T.^4 + (8.9154895E-12)*T.^5; % kg/m^3
%plot(T4-dK, rho_v, '*', T_space-dK, f_rho_v(T_space), '-', T_space-dK,
f_rho_v2(T_space), '-'), legend('Data', 'Spline fit', 'Curve fit from Kroger',
'Location', 'best')
```

Dynamic viscosity - mu

```
mu_L = [1.792 1.519 1.307 1.138 1.002 0.891 0.798 0.720 0.653 0.596 0.547 0.504
0.467 0.433 0.404 0.378 0.355 0.333 0.315 0.297 0.282 0.255 0.232 0.213 0.197
0.183 0.170 0.160 0.150 0.142 0.134 0.122 0.111 0.102 0.094 0.086 0.078 0.070 0.060
0.043].*10^-3;
f_mu_L = @(T) spline(T4, mu_L, T);
f_mu_L2 = @(T) (2.414E-5)*10.^(247.8./(T-140)); %kg/m*s
%plot(T4-dK, mu_L, '*', T_space-dK, f_mu_L(T_space), '-', T_space-dK,
f_mu_L2(T_space), '-'), legend('Data', 'Spline fit', 'Curve fit from Kroger')
```

Specific heat capacity of liquid water - Cp_L

```
f_Cp_L2 = @(T) 8.15599*10^3 - (2.80627*10)*T + (5.11283*10^(-2))*T.^2 -
(2.17582*10^(-13))*T.^6;
Cp_L = [4217 4205 4194 4185 4182 4180 4178 4178 4179 4180 4181 4183 4185 4187 4190
4193 4197 4201 4206 4212 4217 4229 4244 4263 4286 4311 4340 4370 4410 4460 4500
4610 4760 4970 5280 5750 6540 8240 14690];
f_Cp_L = @(T) spline(T2, Cp_L, T);
%plot(T2-dK, Cp_L, '*', T_space-dK, f_Cp_L(T_space), '-', T_space-dK,
f_Cp_L2(T_space), '-'), legend('Data', 'Spline fit', 'Curve fit from Kroger')
```

Enthalpy of vaporisation - h_fg

```
h_fg = [2501 2490 2478 2466 2454 2442 2431 2419 2407 2395 2383 2371 2359 2346 2334
2321 2309 2296 2283 2270 2257 2230 2203 2174 2145 2114 2083 2050 2015 1979 1941
1859 1767 1663 1544 1405 1239 1028 720 0].*10^3;
f_h_fg = @(T) spline(T4, h_fg, T);
```

```
f_h_fg2 = @(T) 3.4831814E6 - 5.8627703E3*T + 12.139568*T.^2 - 1.40290431E-2*T.^3;
%plot(T4-dK, h_fg, '*', T_space-dK, f_h_fg(T_space), '-', T_space-dK,
f_h_fg2(T_space), '-'), legend('Data', 'Spline fit', 'Curve fit from Kroger')
```

Surface tension - sigma

```
f_sigma = @(T) 5.148103E-2 + (3.998714E-4)*T - (1.4721869E-6)*T.^2 +
(1.21405335E-9)*T.^3; %N/m
%plot(T_space, f_sigma(T_space))
```

Thermal conductivity of liquid water - k_L

```
k_L = [0.561 0.571 0.580 0.589 0.598 0.607 0.615 0.623 0.631 0.637 0.644 0.649
0.654 0.659 0.663 0.667 0.670 0.673 0.675 0.677 0.679 0.682 0.683 0.684 0.683 0.682
0.680 0.677 0.673 0.669 0.663 0.650 0.632 0.609 0.581 0.548 0.509 0.469 0.427];
f_k_L = @(T) spline(T2, k_L, T);
f_k_L2 = @(T) -6.14255E-1 + 6.9962E-3*T - 1.01075E-5*T.^2 + 4.74737E-12*T.^4;
%plot(T2-dK, k_L, '*', T_space-dK, f_k_L(T_space), '-', T_space-dK,
f_k_L2(T_space), '-'), legend('Data', 'Spline fit', 'Curve fit from Kroger',
'Location', 'best')
```

Collector Specs

```
a1 = 0.29;                    % [W/m^2*K] - 1st order heat loss coefficient
a2 = 0.003;                   % [W/m^2*K^2] - 2nd order heat loss coefficient
eta_0 = 0.57;                 % zero-loss/optical efficiency
m_c = (1000*3.29/(1000*60))     % kg/s - 3.29-4.25 L/min = recommended flow rate
for XCPC -> assume density = 1000kg/m^3
```

```
m_c = 0.0548
```

```
A_aperture_perCollector = 2.41;     % [m^2] - gross collector area (per collector)
num_CollectorsParallel = 3;     % used to increase the total output of steam
(because flow rate through 1 collector is limited to 4.25m^3/hr)
num_CollectorsSeries = 2;       % used to increase collector outlet temp - Tcol_o =
f(Qu)
A_aperture_total = num_CollectorsSeries*A_aperture_perCollector;   % [m^2] - this
is the heat transfer area that affects gives Tcol_o = f(Qu)
d_colTube = 7.25/1000;                                  % [m] - inner diameter of
collector riser tube - Artic Solar XCPC specs document
A_colTubeCS = pi*(d_colTube^2)/4;                       % [m^2] - cross-sectional
area of collector riser tube
L_colTube = 11.1;                                       % [m] - total length of
collector riser tubes per collector: 3 x 2 x ~1.85m = 11.1m

v_c = m_c/(1000*A_colTubeCS)                            % [m/s] - fluid velocity
through collector riser tube -> assume density of 1000kg/m^3
```

```
v_c = 1.3282
```

Boiler Specs

```
m_b = num_CollectorsParallel*m_c    % number of collectors connected in parallel
determines total flow rate through boiler
```

```
m_b = 0.1645
```

```
do = 25/1000;                           % [m] - from https://www.steeltube.sk/zelpo/
vyrobky.nsf/Tab2UK?OpenPage
t = 1.2/1000;                           % [m] - from https://www.steeltube.sk/zelpo/
vyrobky.nsf/Tab2UK?OpenPage
di = do - 2*t;                          % [m] - from https://www.steeltube.sk/zelpo/
vyrobky.nsf/Tab2UK?OpenPage
Ai = 0.7; % pi*di*L_tube;               % [m^2] - total inner surface area of
boiler tube
L_tube = Ai/(pi*di)                     % [m] - total length of the boiler tube(s),
calculated but later realised actually 9 m long (assume negligible difference)
```

```
L_tube = 9.8592
```

```
Ao = pi*do*L_tube;                      % [m^2] - total inner surface area of
boiler tube
A_boilerTubeCS = pi*(di^2)/4;
Lc_o = do;                                  % [m] - characteristic length for
boiling on outside surface of tubes
Lc_i = di;                                  % [m] - characteristic length for
convection heat transfer on inside surface of tubes
R_cond = log(do/di)/(2*pi*L_tube*k_SS);     % [K/W] C&G Eq. 3-39

V_pool = 50/1000;                           % [m^3] - eg. 50L = 0.05m^3
m_pool = V_pool*1000;                       % [kg] - eg. 50L = 50kg - estimate ->
density of water = 1000kg/m^3

v_b = m_b/(1000*A_boilerTubeCS)             % [m/s] - fluid velocity through boiler
tube -> assume density of 1000kg/m^3
```

```
v_b = 0.4101
```

```
L_connection = 10;                          % [m] - predicted length of piping used
to connect the boiler to the collector array
```

Meteorological Data

Time steps

Time steps are taken in minute terms (now fractions of minutes) because it allows for the use of minute-by-minute data, which may be used later

We assume there are 2m of piping connecting the collector and boiler with the same diameter as the boiler tube.

```
% Time taken for a full collector-boiler cycle
delta_t = (num_CollectorsSeries*L_colTube/v_c + (L_connection + L_tube)/v_b)/60
% [minutes]
```

```
delta_t = 1.0857
```

```
% Time taken for the HTF to pass through the collector
delta_t_collector = ((num_CollectorsSeries*L_colTube)/v_c)/60          % [minutes]
```

```
delta_t_collector = 0.2786
```

```
% Time taken for the HTF to pass through the boiler
delta_t_Boiler = ((L_tube)/v_b)/60                                     % [minutes]
```

```
delta_t_Boiler = 0.4007
```

```
% t_space steps in fractions of minutes
t_space = 1:delta_t:(24*60);                                           % [minutes]

T_a = (15+dK)*ones(1, length(t_space));                                % [K]
A = 580;                                          % [W/m^2] - G max
f_G = @(t) -A*sin((((24/(2*11))*(2*pi))/(24*60))*t - 5);
GTI = max(0, f_G(t_space))
```

```
GTI = 1×1326
     0     0     0     0     0     0     0     0     0     0     0     0     0···
```

```
plot(t_space./60, GTI, t_space./60, T_a), grid on
legend('G (W/m^2)', 'T_{a} (K)', 'Location','best')
```

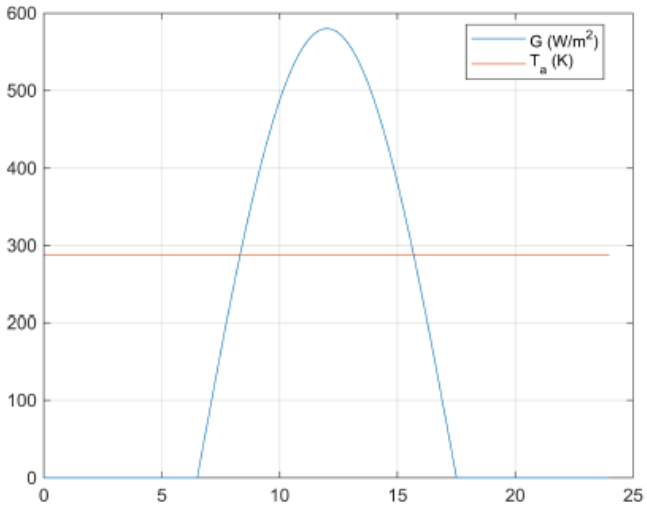

Calculation

Initial conditions

```
Tcol_i = T_a(1);            % collector inlet temp = boiler tube-side inlet temp
Tcol_o = T_a(1);            % collector outlet temp = boiler tube-side outlet temp
T_m = (Tcol_i + Tcol_o)/2;  % i.e. T_m = Ta(1) @ t = 0  -> mean collector temp =
mean of inlet and outlet temps
T_pool = T_a(1);            % bulk mean pool temp
```

Initial estimates

```
T_so = (T_m + T_pool)/2;    % i.e T_so = Ta(1) @ t = 0  -> mean temp of outer
surface of boiler tube
T_si = T_so;                % i.e T_si = Ta(1) @ t = 0  -> mean temp of inner
surface of boiler tube
T_fo = (T_so + T_pool)/2;   % i.e T_fo = Ta(1) @ t = 0  -> film temp on outside of
boiler tube
T_fi = (T_si + T_m)/2;      % i.e T_fi = Ta(1) @ t = 0  -> film temp on inside of
boiler tube
```

Matrices for storage

```
% these matrices are used to store one value per time step for an entire day
M_Tcol_i = zeros(1, length(GTI));
M_Tcol_o = zeros(1, length(GTI));
M_Tpool = zeros(1, length(GTI));
M_Tm = zeros(1, length(GTI));
M_Tsi = zeros(1, length(GTI));
M_Tso = zeros(1, length(GTI));
M_deltaT_excess = zeros(1, length(GTI));
M_Qu = zeros(1, length(GTI));
M_Qsens = zeros(1, length(GTI));
M_Qboil = zeros(1, length(GTI));
M_m_steam = zeros(1, length(GTI));
M_effectiveness_Sens = zeros(1, length(GTI));
M_effectiveness_Latent = zeros(1, length(GTI));
M_errorQ = zeros(1, length(GTI));
M_errorTpool = zeros(1, length(GTI));
M_errorTso = zeros(1, length(GTI));
M_errorTsi = zeros(1, length(GTI));
M_NTU = zeros(1, length(GTI));

activateSignal = 1;
```

Loop through day

```
for i = 1:1:length(GTI)

% Collector heat loss driving potential
deltaT_ma = T_m - T_a(i);
```

```
% Solar input to collector - useful heat gain
Q_u = A_aperture_total*(GTI(i)*eta_0 - a1*deltaT_ma - a2*deltaT_ma^2);

% New collector outlet temp after fluid volume at Tcol_i has moved all the way
through the collector - assume only sensible heat transfer
Tcol_o = Tcol_i + Q_u/(f_Cp_L(T_m)*m_c);

% Update mean HTF temp
T_m = (Tcol_i + Tcol_o)/2;

% New estimate for surface temp on outside of boiler tube
T_soEst = (T_m + T_pool)/2;

% Update deltaT_excess - used to calculate conv. HT coefficient on pool-side of
boiler and also nucleate boiling HT rate
deltaT_excess = T_soEst - T_pool;

% errorQ is one of 4 that are used when iteratively solving for the estimated
surface and film temperatures
errorQ = 1000;

% Reset sensible and latent HT values to zero at the beginning of each time step
Q_sensible = 0;
Q_sensibleNEW = 0;
Q_latent = 0;
eps = 0;

cnt = 1; % this count is used when iteratively solving for the estimated surface
and film temperatures
```

Sensible heat gain or loss by pool

```
% ***** Sensible HT into pool *****

% will occur when (A) Tm > Tpool while Tpool < 100C ... OR ... (B) when Tm < Tpool
while Tpool = any value

if (T_pool < 100+dK && T_m > T_pool) || (T_m < T_pool)

    while (errorQ > 1E-6  || errorTpool > 1E-6 || errorTso > 1E-6  || errorTsi >
1E-6) && cnt < 1000
    % this while loop is used to solve iteratively for Qsens, starting with
estimates for surface and film temps

        v_i = m_b/(f_rho_L(T_m)*A_boilerTubeCS);
        Re_i = f_rho_L(T_m)*v_i*di/f_mu_L(T_m);     % C&G Eq. 8-5
```

```
        f_i = (0.790*log(Re_i)-1.64)^(-2);          % Petukhov (1970) -> surface
friction - for turbulent flow in smooth pipes

        % Nusselt number for hi - conv HT coefficient on inside of boiler tubes
        if Re_i < 3000 % laminar flow
            % we assume constant surface temp conv. HT - more conservative than
constant heat flux 4.36
            Nu_i = 3.66;
        elseif Re_i > 3000 && Re_i < 5*10^6 % turbulent flow
            Nu_i = (f_i/8)*(Re_i - 1000)*f_Pr_L(T_m)/(1 + 12.7*((f_i/
8)^0.5)*(f_Pr_L(T_m)^(2/3) - 1)); % Gnielinski (1976)
        else
            "Re out of bounds"
        end

        % Convection HT on inside of boiler tubes
        h_i = Nu_i*f_k_L(T_m)/Lc_i;    % C&G Eq. 6-5
        Rconv_i_NEW = 1/(h_i*Ai);       % C&G Eq. 3-8

        % Convection HT on outside of boiler tubes
        beta = f_beta(T_fo);
        Pr_L = f_Pr_L(T_fo);
        mu_L = f_mu_L(T_fo);
        rho_L = f_rho_L(T_fo);

        Ra_D = (g*beta*abs(deltaT_excess)*(Lc_o^3)*Pr_L)/((mu_L/rho_L)^2);
% C&G Eq. 9-17
        Nu_o = (0.6 + (0.387*Ra_D^(1/6))/((1 + (0.559/Pr_L)^(9/16))^(8/27)))^2;
% C&G Eq. 9-25
        h_o = Nu_o*f_k_L(T_fo)/Lc_o;    % C&G Eq. 6-5
        Rconv_o_NEW = 1/(h_o*Ao);       % C&G Eq. 3-8

        % Total HT resistance from boiler tube-side fluid to pool
        if ~isreal(Rconv_o_NEW)
            T_soNEW = (T_m + T_pool)/2
        elseif ~isreal(Rconv_i_NEW)
            T_siNEW = (T_m + T_pool)/2
        else
            Rconv_i = Rconv_i_NEW;
            Rconv_o = Rconv_o_NEW;

            R_total = Rconv_i + R_cond + Rconv_o;       % C&G Eq. 3-16

            UA = 1/R_total;                             % C&G Eq. 11-4

            C1 = m_b*f_Cp_L(T_m);                                   % tube side ->
unmixed
            C2 = (m_pool/(delta_t_Boiler*60))*f_Cp_L(T_pool);       % shell side ->
mixed
```

```
            Cmin = min(C1, C2);
            Cmax = max(C1, C2);

            c = Cmin/Cmax;                                  % C&G Eq. 11-40

            Qsens_max = Cmin*(Tcol_o - T_pool);             % C&G Eq. 11-32

            NTU = UA/Cmin;                                  % C&G Eq. 11-39

            % We approximate the bulk pool temp to be constant for each time step -
therefore, Cmin = 0 -> c = 0
            eps = 1 - exp(-NTU);                            % C&G

            % Sensible HT rate
            Q_sensibleNEW = eps*Qsens_max;                  % C&G Eq. 11-33

            % Bisection-type method - used to solve for estimated surface
temperatures
            T_si_1 = T_m - Q_sensibleNEW*Rconv_i;
            T_so_1 = T_si_1 - Q_sensibleNEW*R_cond;
            T_so_2 = T_pool + Q_sensibleNEW*Rconv_o;
            T_si_2 = T_so_2 + Q_sensibleNEW*R_cond;

            T_siNEW = (T_si_1 + T_si_2)/2;
            T_soNEW = (T_so_1 + T_so_2)/2;

            if T_siNEW > 350+dK || T_siNEW < 350+dK
               T_siNEW = (T_m + T_pool)/2;
            end

            if T_soNEW > 350+dK || T_soNEW < 350+dK
               T_soNEW = (T_m + T_pool)/2;
            end

        end

        % Update film temperatures
        T_fi = (T_siNEW + T_m)/2;
        T_fo = (T_soNEW + T_pool)/2;

        % Since we know Tpool but can also calculate it using Tso and Qsens, we
compare actual to calculated Tpool to measure convergence
        T_poolCheck = T_soNEW - Q_sensibleNEW*Rconv_o;

        % Update error/convergence indicator values
        errorTpool = abs((T_pool - T_poolCheck)/T_pool);
        errorTso = abs((T_so - T_soNEW)/T_so);
        errorTsi = abs((T_si - T_siNEW)/T_si);

        if Q_sensible ~= 0
```

```
            errorQ = abs((Q_sensibleNEW-Q_sensible)/Q_sensible); % can use this
only when Q_sens is not equal to zero
        elseif Q_sensible == 0 && GTI(i) == 0 && activateSignal == 1
            errorQ = 1E-10; % set the error to very small, because Q_sens == 0 is
indeed true until G > 0 for the first time
        elseif cnt == 1
            errorQ = 1000;
        else
            disp(delta_t*i/(60))
        end

        % Update surface temps and Qsens once error has been calculated
        T_so = T_soNEW;
        T_si = T_siNEW;
        Q_sensible = Q_sensibleNEW;

        deltaT_excess = T_so - T_pool;

        cnt = cnt+1;
    end

    % Update tube side temp - the sensible or latent HT into/out of the pool equals
the HT out of/into the tube-side fluid
    Tcol_i = Tcol_o - Q_sensible/(m_b*f_Cp_L(T_m));  % ?

    T_pool = T_pool + Q_sensible*(delta_t_Boiler*60)/(f_Cp_L(T_pool)*m_pool);   %
this is the new pool temperature for the NEXT time step

    % Update mean collector temp
    T_m = (Tcol_i + Tcol_o)/2;

    % Update matrices
    M_errorQ(i) = errorQ;
    M_errorTpool(i) = errorTpool;
    M_errorTso(i) = errorTso;
    M_errorTsi(i) = errorTsi;
    M_effectiveness_Sens(i) = eps;
    M_NTU(i) = NTU;
```

Boiling in pool

```
% ***** Latent HT into pool (boiling) *****
% will occur when Tpool >= 100C and Tm > Tpool

elseif T_pool >= 100+dK && T_m > T_pool

    while (errorQ > 1E-6  || errorTpool > 1E-6 || errorTso > 1E-6  || errorTsi >
1E-6) && cnt < 1000
```

```
    % this while loop is used to solve iteratively for Qsens, starting with
estimates for surface and film temps

        v_i = m_b/(f_rho_L(T_m)*(pi*(di^2)/4));
        Re_i = f_rho_L(T_m)*v_i*di/f_mu_L(T_m);     % C&G Eq. 8-5
        f_i = (0.790*log(Re_i)-1.64)^(-2);          % Petukhov (1970) -> surface
friction - for turbulent flow in smooth pipes

        % Nusselt number for hi - conv HT coefficient on inside of boiler tubes
        if Re_i < 3000 % laminar flow
            % we assume constant surface temp conv. HT - more conservative than
constant heat flux 4.36
            Nu_i = 3.66;
        elseif Re_i > 3000 && Re_i < 5*10^6 % turbulent flow
            Nu_i = (f_i/8)*(Re_i - 1000)*f_Pr_L(T_m)/(1 + 12.7*((f_i/
8)^0.5)*(f_Pr_L(T_m)^(2/3) - 1)); % Gnielinski (1976)
        else
            "Re out of bounds"
        end

        % Convection HT on inside of boiler tubes
        h_i = Nu_i*f_k_L(T_fi)/Lc_i;    % C&G Eq. 6-5
        Rconv_i_NEW = 1/(h_i*Ai);       % C&G Eq. 3-8

        % HT on outside of boiler tubes

        if (deltaT_excess > 0) && (deltaT_excess <=5)

            % Natural convection boiling - fluid properties evaluated at mean film
temp

            Ra_D = (g*f_beta(T_fo)*abs(deltaT_excess)*(Lc_o^3)*f_Pr_L(T_fo))/
((f_mu_L(T_fo)/f_rho_L(T_fo))^2); % C&G Eq. 9-17
            Nu_o = (0.6 + (0.387*Ra_D^(1/6))/((1 + (0.559/
f_Pr_L(T_fo))^(9/16))^(8/27)))^2; % C&G Eq. 9-25
            h_o = Nu_o*f_k_L(T_fo)/Lc_o;    % C&G Eq. 6-5
            Rconv_o_NEW = 1/(h_o*Ao);       % C&G Eq. 3-8

        elseif (deltaT_excess > 5) && (deltaT_excess <= 30)

            % Nucleate boiling - fluid properties evaluated at Tsat = Tpool
            q_nucleate = f_mu_L(T_pool)*f_h_fg(T_pool)*((g*(f_rho_L(T_pool) -
f_rho_v(T_pool))/f_sigma(T_pool))^0.5)...
                *(f_Cp_L(T_pool)*deltaT_excess/
(C_sf*f_h_fg(T_pool)*f_Pr_L(T_pool)^n))^3 % [W/m^2] - Rohsenhow (1952)

            q_nucleate_kW = q_nucleate/1000;  % [kW/m^2]

            if q_nucleate_kW < 16
```

```
                h_o = 1042*deltaT_excess^(1/3);                % Holman (1976)
table 9-3
            elseif (q_nucleate_kW > 16) && (q_nucleate_kW < 240)
                h_o = 5.56*deltaT_excess^3;                    % Holman (1976)
table 9-3
            else
                disp("Exception (nucleate boiling)")
            end

            Rconv_o_NEW = 1/(h_o*Ao);       % C&G Eq. 3-8

        else
            disp("Boiling out of bounds")
        end


        % Total HT resistance from boiler tube-side fluid to pool
        if ~isreal(Rconv_o_NEW)
            T_soNEW = (T_m + T_pool)/2;
        elseif ~isreal(Rconv_i_NEW)
            T_siNEW = (T_m + T_pool)/2;
        else
            Rconv_i = Rconv_i_NEW;
            Rconv_o = Rconv_o_NEW;

            R_total = Rconv_i + R_cond + Rconv_o;       % C&G Eq. 3-16

            UA = 1/R_total;                             % C&G Eq. 11-4

            C1 = m_b*f_Cp_L(T_m);                                   % tube side ->
unmixed
            C2 = (m_pool/(delta_t_Boiler*60))*f_Cp_L(T_pool);       % shell side ->
mixed

            Cmin = min(C1, C2);
            Cmax = max(C1, C2);

            c = Cmin/Cmax;                          % C&G Eq. 11-40

            Qlatent_max = Cmin*(Tcol_o - T_pool);   % C&G Eq. 11-32

            NTU = UA/Cmin;                          % C&G Eq. 11-39

            eps = 1 - exp(-NTU);                    % C&G Eq. 11-41 ->
effectiveness of all HXs with phase change

            % Latent HT rate
            Q_latentNEW = eps*Qlatent_max;          % C&G Eq. 11-33
```

```
            % Bisection-type method - used to solve for estimated surface
temperatures
            T_si_1 = T_m - Q_latentNEW*Rconv_i;
            T_so_1 = T_si_1 - Q_latentNEW*R_cond;
            T_so_2 = T_pool + Q_latentNEW*Rconv_o;
            T_si_2 = T_so_2 + Q_latentNEW*R_cond;

            T_siNEW = (T_si_1 + T_si_2)/2;
            T_soNEW = (T_so_1 + T_so_2)/2;

            if T_siNEW > 350+dK || T_siNEW < 350+dK
               T_siNEW = (T_m + T_pool)/2;
            end

            if T_soNEW > 350+dK || T_soNEW < 350+dK
               T_soNEW = (T_m + T_pool)/2;
            end

        end

        % Update film temperatures
        T_fi = (T_siNEW + T_m)/2;
        T_fo = (T_soNEW + T_pool)/2;

        % Since we know Tpool but can also calculate it using Tso and Qsens, we
compare actual to calculated Tpool to measure convergence
        T_poolCheck = T_soNEW - Q_latentNEW*Rconv_o;

        % Update error/convergence indicator values
        errorTpool = abs((T_pool - T_poolCheck)/T_pool);
        errorTso = abs((T_so - T_soNEW)/T_so);
        errorTsi = abs((T_si - T_siNEW)/T_si);

        if Q_latent ~= 0
            errorQ = abs((Q_latentNEW-Q_latent)/Q_latent); % On the first
iteration, Q_latent will = zero -> this will give NaN
        elseif cnt == 1
            errorQ = 1000;
        else
            disp(delta_t*i/(60))
        end

        % Update surface temps and Qsens once error has been calculated
        T_so = T_soNEW;
        T_si = T_siNEW;
        Q_latent = Q_latentNEW;

        deltaT_excess = T_so - T_pool;

        cnt = cnt+1;
```

```
    end

    % Update tube side temp - the sensible or latent HT into/out of the pool equals
the HT out of/into the tube-side fluid
    Tcol_i = Tcol_o - Q_latent/(m_b*f_Cp_L(T_m)); % note that Q_latent on the pool
side = Q_sensible on the tube side

    % Update mean collector temp
    T_m = (Tcol_i + Tcol_o)/2;

    % Update matrices
    M_effectiveness_Latent(i) = eps;
    M_errorQ(i) = errorQ;
    M_errorTpool(i) = errorTpool;
    M_errorTso(i) = errorTso;
    M_errorTsi(i) = errorTsi;
    M_NTU(i) = NTU;

else % EXCEPTION
    Q_sensible = 0;
    Q_latent = 0;
    if GTI(i) ~= 0
        disp("Exception")
    end
end

% Calculate the amount of steam generated in this cycle
m_steam = Q_latent/f_h_fg(T_pool);

% Update matrices with values for this cycle
M_Tcol_i(i) = Tcol_i;
M_Tcol_o(i) = Tcol_o;
M_Tsi(i) = T_si;
M_Tso(i) = T_so;
M_Tm(i) = T_m;
M_Tpool(i) = T_pool;
M_deltaT_excess(i) = deltaT_excess;
M_Qu(i) = Q_u;
M_Qsens(i) = Q_sensible;
M_Qboil(i) = Q_latent;
M_m_steam(i) = m_steam;
end
```

Results

```
plot(t_space./60, M_Qu, t_space./60, GTI*A_aperture_total), legend('Q',
'GTI*A_{aperture tot}'), grid on
xlabel('Time (hrs)')
ylabel('Energy (W)')
```

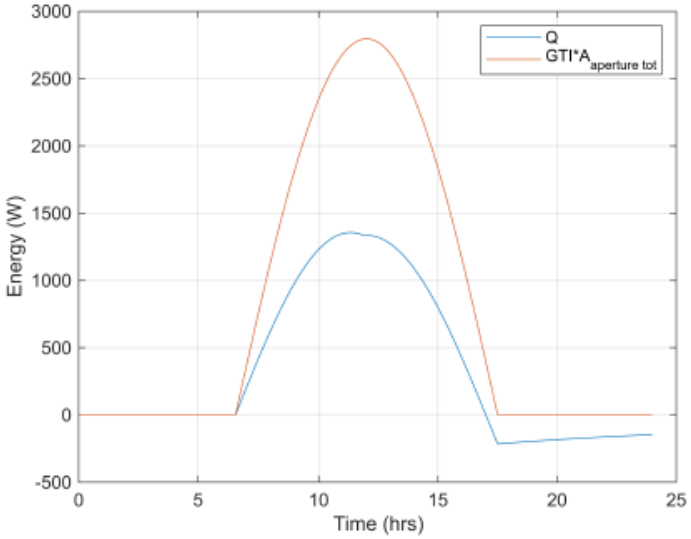


```
plot(t_space./60, num_CollectorsParallel*M_Qu, t_space./60, M_Qsens, t_space./60,
M_Qboil), legend('Q_{u}', 'Q_{sensible}', 'Q_{boil}', 'Location', 'best'), grid on
xlabel('Time (hrs)')
ylabel('Energy (W)')
```

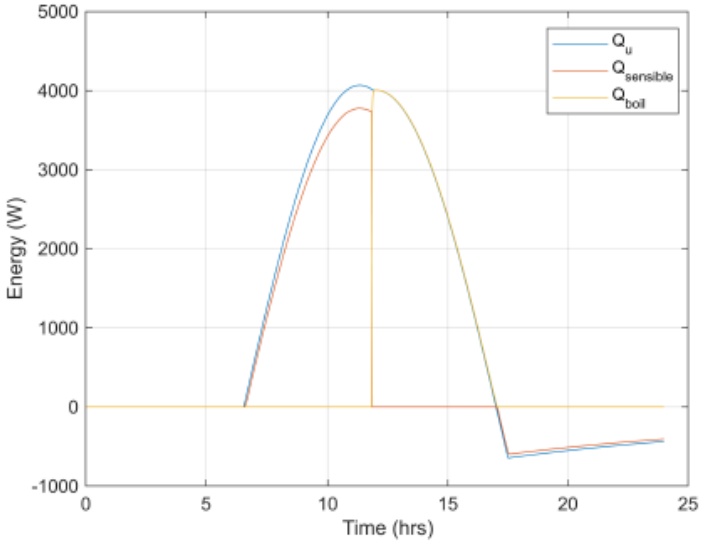


```
plot(t_space./60, M_Tcol_i - dK, t_space./60, M_Tcol_o - dK, t_space./60, M_Tpool -
dK, t_space./60, M_Tm - dK, t_space./60, M_Tsi - dK, t_space./60, M_Tso - dK), grid
on
legend('T_{col in}', 'T_{col out}', 'T_{pool}', 'T_{m}', 'T_{si}', 'T_{so}',
'Location', 'best')
xlabel('Time (hrs)')
ylabel('Temperature (°C)')
```

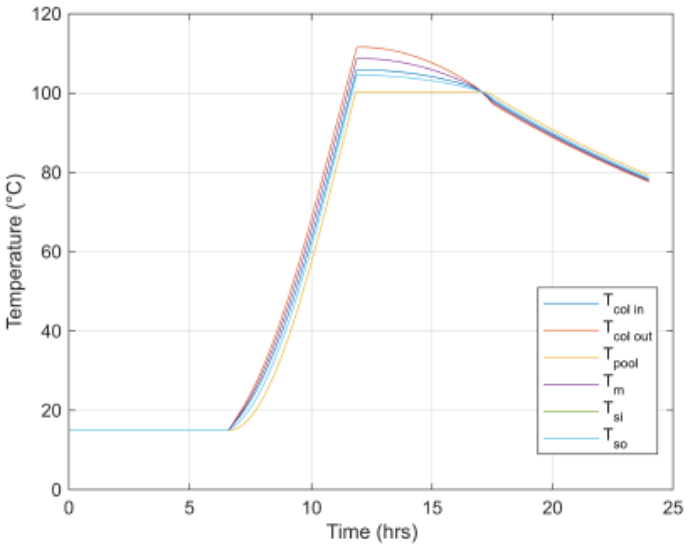


```
plot(t_space./60,  M_deltaT_excess), grid on
```

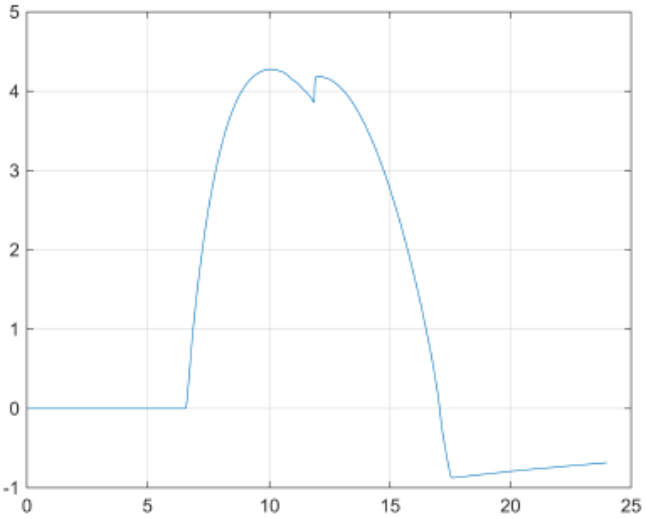

```
m_required = 1.28*10^-3; % kg/s - max for for 1 cylinder
plot(t_space./60, M_m_steam.*1000, t_space./60, m_required*ones(1,
length(GTI)).*1000, t_space./60, 2*m_required*ones(1, length(GTI)).*1000,
"MarkerSize", 1), grid on
legend('m_{steam}', 'm_{req for 1 x cyl}', 'm_{req for 2 x cyl}', 'Location',
'best')
xlabel('Time (hrs)')
ylabel('Steam Generated (g/s)')
```

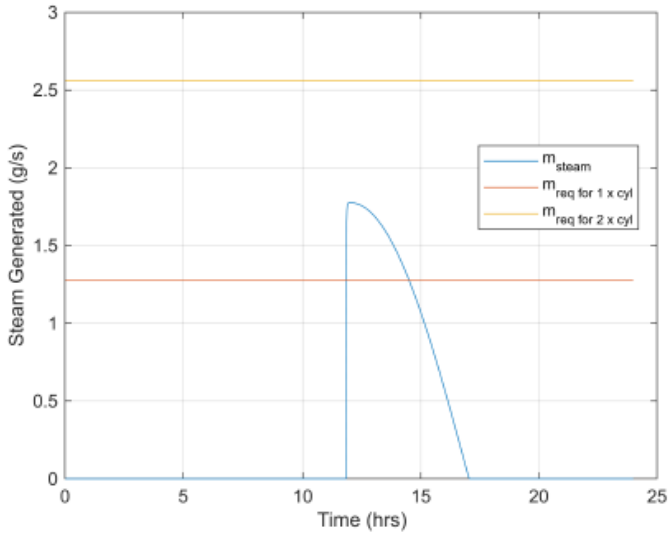


```
m_steamTotal = sum(M_m_steam*(delta_t*60))
```

```
m_steamTotal = 21.6659
```

References

Agency for Toxic Substances and Disease Registry. 2007. Toxicological profile for Benzene. Available: https://www.atsdr.cdc.gov/toxprofiles/tp3.pdf.

Agency for Toxic Substances and Disease Registry. 2017. Toxicological profile for Toluene. Atlanta. Available: https://www.atsdr.cdc.gov/toxprofiles/tp56.pdf.

Ahuja, S. 2021. Overview: Modern water purity and quality, in Handbook of Water Purity and Quality, Elsevier. 1–18. DOI: 10.1016/B978-0-12-821057-4.00014-8.

Artic Solar Inc. 2021. External Concentrating Parabolic Collector (XCPC). Available: www.articsolar.com.

Atkins, P., de Paula, J. & Keeler, J. 2018. Physical Chemistry. 11th ed. New York: Oxford University Press.

Bannister, P. 1991. An experimental and analytical assessment of a steam Rankine solar thermal power system. Thesis for degree of Doctor of Philosophy. Australian National University. DOI: 10.13140/RG.2.2.20340.76167.

Brooks, M., du Clou, S., van Niekerk, J., Gauche, P., Leonard, C., Mouzouris, M., Meyer, A., van der Westhuizen, N., van Dyk, E. & Vorster, F. 2015. SAURAN: A New Source for Solar Radiometric Data in Southern Africa. Journal of Energy in Southern Africa. 26:2–10. Available: https://sauran.ac.za/.

Cengel, Y. & Ghajar, A. 2015. Heat and mass transfer: fundamentals and applications. 5th ed. New York: McGraw-Hill.

Council for Scientific and Industrial Research - CSIR. 2022. Statistics of utility-scale power generation in South Africa in 2021. Available: https://www.csir.co.za/sites/default/files/Documents/20220503-Statistics%20of%20power%20in%20SA%20H2-2021-CSIR-%5BFINAL%5D%20%281%29.pdf.

Department of Energy. 2012. A survey of energy-related behaviour and perceptions in South Africa. Available: https://www.energy.gov.za/files/media/Pub/Survey%20of%20Energy%20related%20behaviour%20and%20perception%20in%20SA%20-%20Residential%20Sector%20-%202012.pdf.

Department of Public Enterprises Republic of South Africa. 2019. Roadmap for Eskom in a reformed electricity supply industry. Available: https://www.gov.za/sites/default/files/gcis_document/201910/roadmap-eskom.pdf.

Dieter, G.E. & Schmidt, L.C. 2013. Engineering design. 5th ed. New York: McGraw-Hill.

Dincer, I. & Kanoglu, M. 2010. Refrigeration systems and applications. 2nd ed. John Wiley & Sons (ed.). DOI: 10.1002/9780470661093.

Duffie, J.A. & Beckman, W.A. 2013. Solar engineering of thermal processes. 4th ed. Hoboken, New Jersey: Wiley. DOI: 10.1002/9781118671603.

Guppy, L. & Anderson, K. 2017. Global water crisis: the facts. Hamilton, Canada. Available: http://inweh.unu.edu.

International Bank for Reconstruction and Development & World Bank. 2012. Renewable energy desalination: an emerging solution to close the water gap in the Middle East and North Africa. Washington DC. DOI: 10.1596/978-0-8213-8838-9.

Josse, H. 1885. Moteur Domestique - Systeme Hathorn, Davey and Co. Revue industrielle: revue mensuelle technique et économique. 93–94. Available: https://gallica.bnf.fr/ark:/12148/bpt6k97674548/f105.item.

Kalogirou, S.A. 2014. Solar energy engineering processes and systems. 2nd ed. San Diego: Academic Press. DOI: 10.1016/B978-0-12-374501-9.X0001-5.

Kamrin, M. 1990. Distillation for home water treatment. Michigan. Available: https://www.baycounty-mi.gov/Docs/CitizenCorps/DistillationForHomeWaterTreatment.pdf

Landelle, A., Tauveron, N., Haberschill, P., Revellin, R. & Colasson, S. 2017. Organic Rankine cycle design and performance comparison based on experimental database. Applied Energy. 204:1172–1187. DOI: 10.1016/j.apenergy.2017.04.012.

Ling-Chin, J., Bao, H., Ma, Z., Taylor, W. & Roskilly, A.P. 2019. State-of-the-art technologies on low-grade heat recovery and utilization in industry. DOI: 10.5772/intechopen.78701.

Liu, B. & Richard, J. 1963. The Long-Term Average Performance of Flat-Plate Solar-Energy Collectors. Available: https://www.sciencedirect.com/science/article/abs/pii/0038092X63900069

Loutzenhiser, P.G., Manz, H., Felsmann, C., Strachan, P.A., Frank, T. & Maxwell, G.M. 2007. Empirical validation of models to compute solar irradiance on inclined surfaces for building energy simulation. Solar Energy. 81(2):254–267. DOI: 10.1016/j.solener.2006.03.009.

Mabuya, B. & Scholes, M. 2020. The three little houses: A comparative study of indoor and ambient temperatures in three low-cost housing types in Gauteng and Mpumalanga, South Africa. International Journal of Environmental Research and Public Health. 17(10). DOI: 10.3390/ijerph17103524.

Matsuda, K. 2013. Low heat power generation system, in Chemical Engineering Transactions, vol. 35, Italian Association of Chemical Engineering - AIDIC. 223–228. DOI: 10.3303/CET1335037.

Müller, G. 2017. The condensing cycle for heat engines with operating temperatures from 50 to 100°C. Proceedings of the 13th Heat Transfer, Fluid Mechanics and Thermodynamics Conference.

Müller, G. & Howell, C. 2021. Comparative analysis of ORC and condensing heat engines for low grade waste heat recovery. Applied Engineering. 5(1):29–35. DOI: 10.11648/j.ae.20210501.15.

Müller, G., Chan, C.H., Gibby, A., Nazir, M.Z., Paterson, J., Seetanah, J., Telfer, M., Tsuzaki, T., Walker, C. & Yusof, F. 2018. The condensing engine: A heat engine for operating temperatures of 100 °C and below. Proceedings of the Institution of Mechanical Engineers, Part A: Journal of Power and Energy. 232(4):437–448. DOI: 10.1177/0957650917736455.

Panagopoulos, A. 2021. Water-energy nexus: desalination technologies and renewable energy sources. Environment Science and Pollution Research. 28. DOI: 10.1007/s11356-021-13332-8/Published.

Pranesh, V., Velraj, R., Christopher, S. & Kumaresan, V. 2019. A 50 year review of basic and applied research in compound parabolic concentrating solar thermal collector for domestic and industrial applications. Elsevier Ltd. DOI: 10.1016/j.solener.2019.04.056.

Presidential Climate Commission. 2022. A presidential climate commission report: A framework for a just transition in South Africa. Available: https://pccommissionflow.imgix.net/uploads/images/A-Just-Transition-Framework-for-South-Africa-2022.pdf.

Rashid, F., Saleem, E.A., Kashif Mehmood, E. & Faizan Rashid, E. 2019. The efficiency of solar PV system. Proceedings of the 2nd International Multi-Disciplinary Conference. Available: https://www.researchgate.net/publication/334277230.

Rasul, M., Masud, M., Khan, K., Ullah, I., Rasul, M.G. & Khan, M.M.K. 2013. An overview of solar thermal desalination technologies. Available: https://www.researchgate.net/publication/258568401.

Senft, J.R. 1987. Mechanical efficiency of kinematic heat engines. Journal of the Franklin Institute. 324(2). DOI: 10.1016/0016-0032(87)90066-4.

SOLARGIS. 2022. Solar Resource Maps and GIS Data for 200+ Countries and Regions. Available: https://solargis.com/maps-and-gis-data/download/world [2022, December 20].

Southern African Development Community. 2015. SADC industrialization strategy and roadmap. Available: https://sadc-eu.sardc.net/resources/RISDP/SADC-Industrialisation-Strategy-and-Roadmap-2015-2063.pdf.

Southern African Development Community & Southern African Research and Documentation Centre. 2018. SADC energy monitor 2018 - enabling industrialization and regional integration in SADC. Gaborone, Harare.

Southern African Power Pool. 2021. SAPP 2021 annual report. Available: https://www.sapp.co.zw/sites/default/files/Full%20Report%20SAPP.pdf.

Spinks, A.T., Dunstan, R.H., Harrison, T., Coombes, P. & Kuczera, G. 2006. Thermal inactivation of water-borne pathogenic and indicator bacteria at sub-boiling temperatures. Water Research. 40(6):1326–1332. DOI: 10.1016/j.watres.2006.01.032.

Stillwell, A.S. & Webber, M.E. 2016. Predicting the specific energy consumption of reverse osmosis desalination. Water (Switzerland). 8(12). DOI: 10.3390/w8120601.

Sturm, R.G. 1941. A study of the collapsing pressure of thin-walled cylinders. Urbana, Illinois. Available: https://core.ac.uk/download/4814572.pdf.

Tchanche, B.F., Lambrinos, G., Frangoudakis, A. & Papadakis, G. 2011. Low-grade heat conversion into power using organic Rankine cycles - A review of various applications. Elsevier Ltd. DOI: 10.1016/j.rser.2011.07.024.

UN Department of Economic and Social Affairs. 2014. World urbanization prospects. New York: United Nations. Available: https://population.un.org/wup/publications/files/wup2014-highlights.pdf.

UN Economic Commission for Africa, African Union Commission & Africa Development Bank. 2003. The Africa water vision for 2025 - equitable and sustainable use of water for socioeconomic development. Addis Ababa, Ethiopia. Available: https://repository.uneca.org/handle/10855/5488.

UN Educational Scientific and Cultural Organisation & UN Water. 2021. The United Nations world water development report 2021 - valuing water. Paris. Available: https://www.unwater.org/publications/un-world-water-development-report-2021.

United Nations. 2022. The sustainable development goals report 2022. Available: 14/12/2022https://unstats.un.org/sdgs/report/2022/The-Sustainable-Development-Goals-Report-2022.pdf.

Widyolar, B., Jiang, L., Bhusal, Y., Brinkley, J. & Winston, R. 2021. Solar thermal process heating with the external compound parabolic concentrator (XCPC) – 45 m2 experimental array performance, annual generation (kWh/m2-year), and economics. Solar Energy. 230:131–150. DOI: 10.1016/j.solener.2021.10.027.

Windenburg, D. & Trilling, C. 1934. Collapse by instability of thin cylindrical shells under external pressure. ASME. 56:819–825.

Winston, R. 2016. *Patent No. US9383120B1*. United States.

World Health Organisation. 2015. Boil water - technical brief. Available: https://apps.who.int/iris/bitstream/handle/10665/155821/WHO_FWC_WSH_15.02_eng.pdf.

Wu, G., Deshmukh, R., Ndhlukula, K., Radojicic, T. & Reilly, J. 2015. Renewable energy zones for Africa clean energy corridor: multi-criteria analysis for planning renewable energy.